

HIGH PERFORMANCE NEAR/SHORT WAVELENGTH INFRARED MEGAPIXEL
InGaAs FOCAL PLANE ARRAY FABRICATION DEVELOPMENT
AND NEW DESIGN PROPOSALS

A THESIS SUBMITTED TO
THE GRADUATE SCHOOL OF NATURAL AND APPLIED SCIENCES
OF
MIDDLE EAST TECHNICAL UNIVERSITY

BY

UTKU KARACA

IN PARTIAL FULFILLMENT OF THE REQUIREMENTS
FOR
THE DEGREE OF MASTER OF SCIENCE
IN
ELECTRICAL AND ELECTRONICS ENGINEERING

JULY 2018

Approval of the thesis:

**HIGH PERFORMANCE NEAR/SHORT WAVELENGTH MEGAPIXEL InGaAs
FOCAL PLANE ARRAY FABRICATION DEVELOPMENT
AND NEW DESIGN PROPOSALS**

submitted by **UTKU KARACA** in partial fulfillment of the requirements for the degree of
**Master of Science in Electrical and Electronics Engineering Department, Middle East
Technical University** by,

Prof. Dr. Halil Kalıpçılar
Dean, **Graduate School of Natural and Applied Sciences**

Prof. Dr. Tolga Çiloğlu
Head of Department, **Electrical and Electronics Eng.**

Assist. Prof. Dr. Serdar Kocaman
Supervisor, **Electrical and Electronics Eng. Dept., METU**

Examining Committee Members:

Prof. Dr. Cengiz Beşikçi
Electrical and Electronics Eng. Dept., METU

Assist. Prof. Dr. Serdar Kocaman
Electrical and Electronics Eng. Dept., METU

Prof. Dr. Gönül Turhan Sayan
Electrical and Electronics Eng. Dept., METU

Prof. Dr. Haluk Külâh
Electrical and Electronics Eng. Dept., METU

Assoc. Prof. Dr. Tuğba Selcen Navruz
Electrical and Electronics Eng. Dept., Gazi University

Date: 04.07.2018

I hereby declare that all information in this document has been obtained and presented in accordance with academic rules and ethical conduct. I also declare that, as required by these rules and conduct, I have fully cited and referenced all material and results that are not original to this work.

Name, Surname : Utku Karaca

Signature :

ABSTRACT

HIGH PERFORMANCE NEAR/SHORT WAVELENGTH INFRARED MEGAPIXEL InGaAs FOCAL PLANE ARRAY FABRICATION DEVELOPMENT AND NEW DESIGN PROPOSALS

Karaca, Utku

M.S., Department of Electrical and Electronics Engineering

Supervisor: Assist. Prof. Dr. Serdar Kocaman

July 2018, 92 pages

$\text{In}_{0.53}\text{Ga}_{0.47}\text{As}$ is the most appropriate material system for Short Wavelength Infrared (SWIR) detection at $\sim 1.7 \mu\text{m}$ cutoff wavelength with its relatively lower cost and high performance. Ultra-low dark current ($\sim \text{nA}/\text{cm}^2$) has been recently demonstrated in InGaAs photodetectors with planar type process by eliminating surface leakage current. Here, a fabrication procedure for planar InGaAs photodetectors with unique pixel isolation methods has been developed and $\sim 10 \text{ nA}/\text{cm}^2$ dark current density levels were obtained from 15 and 25 μm pitch megapixel and large format Focal Plane Arrays (FPA) where almost 100% internal quantum efficiency was measured. Mesa type InGaAs photodetectors were also fabricated to be able to make a comparison between two process types. Developed photodetectors were able to sense both Near Infrared (NIR) and visible region of electromagnetic spectrum by removing InP substrate and $\sim 99.5\%$ pixel operability was achieved in FPAs after flip-chip bonding and substrate removal. Furthermore, a novel all InGaAs nBn photodetector design was also proposed numerically in order to reduce surface leakage current particularly in mesa type photodetectors. Simulations were executed in Sentaurus TCAD numerical tool where InGaAs material properties were optimized with the data provided in literature, and also with the experimental results obtained in InGaAs photodetector fabrication. Shockley-Read-Hall (SRH), Auger, radiative and surface currents were modeled and more than 20

times improvement in dark current has been shown to be achievable by utilizing nBn photodetector compared to conventional p-n InP/InGaAs photodetectors without degrading responsivity.

Keywords: Photodetector, InGaAs, Near Infrared, Short Wavelength Infrared, Focal Plane Array, Megapixel.

ÖZ

YÜKSEK PERFORMANS YAKIN/KISA DALGA BOYU KIZILÖTESİ MEGAPİKSEL InGaAs ODAK DÜZLEM DİZİNLERİNİN FABRİKASYONUNUN GELİŞTİRİLMESİ VE YENİ DİZAYN ÖNERİLERİ

Karaca, Utku

Yüksek Lisans, Elektrik ve Elektronik Mühendisliği Bölümü

Tez Yöneticisi: Dr. Öğr. Üyesi Serdar Kocaman

Temmuz 2018, 92 sayfa

In_{0.53}Ga_{0.47}As sahip olduğu ~1.7 µm kesim dalga boyu ve daha düşük maliyetle Kısa Dalga Boyu Kızılötesi (SWIR) bandı görüntüleme için en uygun malzeme sistemi olarak gözükmektedir. Planar tipi yöntem yakın zamanda InGaAs fotodedektörlerde yüzey kaçak akımını azaltarak çok düşük karanlık akım (~ nA/cm²) seviyelerine ulaşılabilceğini gösterdi. Bu çalışmada, 15 ve 25 µm piksel adımına ve özgün piksel izolasyonuna sahip megapiksel ve geniş format InGaAs fotodedektör Odak Düzlem Dizinleri (ODD) için bir fabrikasyon prosedürü geliştirildi ve üretilen cihazlarda ~10 nA/cm² seviyesinde karanlık akım yoğunluğu ve yaklaşık %100 içsel kuantum verimliliği seviyelerine ulaşıldı. Mesa tipi InGaAs fotodedektörler de iki üretim tipinin karşılaştırılması açısından geliştirildi. Fotodedektörler, InP alttaşın kaldırılmasıyla elektromanyetik spektrumun görünür ve Yakın Kızılötesi (NIR) bölgelerini algılayabilecek şekilde üretildi ve ters yonga paketlemesi ve alttaşın kaldırılmasının ardından, üretilen Odak Düzlem Dizinlerinde ~%99.5 piksel çalışma kapasitesine ulaşıldı. Bu çalışmaya ek olarak, özellikle mesa tipi fotodedektörlerdeki yüzey kaçak akımını engellemek amacıyla tamamen InGaAs malzemesine dayalı eşsiz nBn fotodedektör dizaynı nümerik olarak önerildi. Simülasyonlar Sentaurus TCAD nümerik programında gerçekleştirildi ve programda InGaAs malzemesinin özellikleri literatürde sağlanan bilgi ve ayrıca InGaAs fotodedektör fabrikasyonundan elde edilen deneysel

tecrübeyle optimize edildi. Shockley-Read-Hall (SRH), Auger, ışım ve yüzey akımları modellenip çalışma sonunda nBn tipi fotodedektör kullanılarak geleneksel p-n InP/InGaAs fotodedektör tipine göre tepkisellikte bozulmaya yol açmadan karanlık akımda 20 kattan fazla gelişim elde edilebileceği gösterildi.

Anahtar Kelimeler: Fotodedektör, InGaAs, Yakın Kızılötesi, Kısa Dalga Boyu Kızılötesi, Odak Düzlem Dizini, Megapiksel.

To My Family

ACKNOWLEDGMENTS

First, I would like to express my sincere gratitude to my supervisor Assist. Prof. Dr. Serdar Kocaman for his extraordinary guidance in this work, and in my academic career starting from my undergraduate level. I also want to thank Prof. Kocaman for his invaluable recommendations and providing me chance to work in such an advanced laboratory.

I also want to thank Prof. Dr. Cengiz Beşikçi for sharing his immense knowledge and experience with me, giving me chance to work in such an exceptional facility and being on my thesis committee.

I am thankful to Prof. Dr. Gönül Turhan Sayan, Prof. Dr. Haluk Külâh and Assoc. Prof. Dr. Tuğba Selcen Navruz for accepting to be on my thesis committee.

I would like to thank ASELSAN A.Ş. and Presidency of the Republic of Turkey Undersecretariat for Defence Industries (SSM) for their support.

I also owe a debt of gratitude to Halit Dolaş, Ekin Kızıllkan, Kübra Çırçır and Muammer Kozan for their invaluable friendship in and outside of laboratory, sharing their knowledge with me and the conversations we had which kept me going in this work.

I would like to thank Fatih Uzgur, Eray Yurtseven, Yiğit Özer and Kaan Sel for their friendship, help and enjoyable moments in and outside of laboratory.

I want to thank to my friends Eray Kaçar, Fatih Kalyon, Burak Açıkgöz, Ertuğrul Aksoy, Alperen Gövdeli and Murat Can Sarıhan for their invaluable friendships.

Last but the best, I would like to express my love to my family for being always with me.

TABLE OF CONTENTS

ABSTRACT	v
ÖZ	viii
DEDICATION	ix
ACKNOWLEDGMENTS.....	x
TABLE OF CONTENTS	xi
LIST OF TABLES	xiv
LIST OF FIGURES	xv
LIST OF ABBREVIATIONS	xx
CHAPTERS	
1. INTRODUCTION	1
1.1. Fundamentals of Infrared Radiation.....	2
1.2. Infrared Photodetectors with Figure of Merits	6
1.2.1 Responsivity.....	8
1.2.2 Noise	9
1.2.3 Noise Equivalent Power and Detectivity	10
1.2.4 Noise Equivalent Temperature Difference and Irradiance.....	11
1.3. Infrared Photon Detector Types	12
1.4. Scope and the Motivation of the Work	23
2. NIR/SWIR PHOTODETECTOR TECHNOLOGY AND STATUS	25
2.1. Application Areas and Properties of SWIR Photodetectors.....	25

2.2.	Utilized Materials in SWIR Detection and p-i-n Diode Concept.....	30
2.2.1	Semiconductors of SWIR Band	30
2.2.2	p-i-n Type Photodiodes	32
2.3.	NIR/SWIR HgCdTe Photodetectors.....	34
2.4.	NIR/SWIR InGaAs Photodetectors	40
2.4.1	Mesa and Planar Process in InGaAs Photodetectors.....	41
2.4.2	Planar Type State-of-the-art InGaAs Photodetectors.....	43
2.4.3	Mesa Type State-of-the-art InGaAs Photodetectors	47
3.	PLANAR AND MESA TYPE MEGAPIXEL AND LARGE FORMAT SWIR InGaAs FPA FABRICATION DEVELOPMENT	51
3.1.	MBE Growth of InGaAs Photodetectors and Wafer Characterization.....	51
3.1.1	MBE System Basics	52
3.1.2	Growth Procedure of the Designs	53
3.1.3	Wafer Characterization	55
3.2.	How to Conclude with Final Design Structure.....	57
3.3.	Fabrication Procedure of NIR/SWIR InGaAs Photodetectors	60
3.3.1	Fabrication of Planar Type Photodetectors	60
3.3.2	Fabrication of Mesa Type Photodetectors.....	65
3.4.	Characterization Results of NIR/SWIR InGaAs Photodetectors	66
3.4.1	I-V Measurement Results.....	66
3.4.2	Responsivity and Detectivity Measurement Results.....	69
3.4.3	Imaging	73
4.	A NEW DESIGN APPROACH FOR InGaAs PHOTODETECTORS	77
4.1.	All InGaAs nBn Type Photodetector Design	77

4.2. Device Characterization Results80

5. CONCLUSION AND FUTURE WORK85

REFERENCES87

LIST OF TABLES

TABLES

Table 2.1: Lattice matched InGaAs and InP material properties at 300 K.	40
Table 3.1: “ISC0002” ROIC Parameter Specifications [38].	62

LIST OF FIGURES

FIGURES

Figure 1.1: Spectral radiant exitance of a blackbody versus wavelength for different temperatures [4].	3
Figure 1.2: Atmospheric transmittance at infrared region [3].	5
Figure 1.3: (a) Interband excitation mechanism in intrinsic photon detectors. (b) Excitation from an impurity or a trap energy state to conduction band in extrinsic photon detectors. (c) Intersubband excitation between confined energy states of QWIPs [5].	7
Figure 1.4: Basic representation of photoconductor detector working mechanism under biasing circuit.	14
Figure 1.5: A representative photodiode structure showing the photocurrent generation process.	15
Figure 1.6: I-V characteristic of photovoltaic or photodiode type detectors under dark and illuminated conditions.	17
Figure 1.7: Representation of AlGaAs/GaAs QWIPs under applied voltage and Transmission Electron Microscopy (TEM) image from the fabrication [10].	21
Figure 1.8: InAs/GaSb materials based superlattice detector band diagram showing the formation of minibands and excitation process [10].	22
Figure 2.1: Spectral photon exitance curves for different blackbody temperatures.	26

Figure 2.2: Visible and SWIR cameras looking to the same FOV in a hazy environment [13]. 27

Figure 2.3: A SWIR photodetector detecting 1550 nm laser beam [15]. 28

Figure 2.4: Night sky radiance spectrum under different Moonlight levels [17]. 29

Figure 2.5: Typical QE spectrum of InGaAs and HgCdTe detectors depicted on the same graph with airglow spectrum under no Moonlight [20]. 32

Figure 2.6: p-i-n diode structure and corresponding energy band diagram showing also photo-generation process [5]. 33

Figure 2.7: Epilayer structure of p-i-n photodiodes designed for (a) front and (b) back illumination [5]. 34

Figure 2.8: HgCdTe bandgap energy (straight line), cutoff wavelength (parabolic line) and lattice constant variation with the change of Cd mole fraction [22]. 35

Figure 2.9: (a) Idark densities reported from 15 μm pitch, 640x512 HgCdTe FPAs grown on CdZnTe substrates with LPE and GaAs substrates with MBE in AIM facilities for 1.8, 2.5 and 2.6 μm cutoff wavelengths. (b) SWIR images captured from 1.8 μm cutoff detector under daylight and moonless night conditions. (c) Extended SWIR images captured from 2.5 μm cutoff detector under foggy and cloudy conditions [21], [23]. 37

Figure 2.10: p-on-n HgCdTe architecture developed by Sofradir and CEA [25]. 38

Figure 2.11: (a) Sofradir-CEA planar p-on-n architecture HgCdTe photodetectors' dark condition performance in years. (b) QE of HgCdTe detectors when antireflection coating is present [27]. 39

Figure 2.12: In_{0.53}Ga_{0.47}As material's bandgap change with respect to temperature.41

Figure 2.13: Planar type InGaAs photodetectors' typical structure [29].	42
Figure 2.14: (a) Dark current density of 20 μm pitch 640x512 NIR/SWIR InGaAs camera developed by Goodrich SUI. (b) QE of the fabricated photodetectors. (c) Images taken by 640SDX product under Tungsten lamp illumination and low light level [30].	43
Figure 2.15: (a) Dark current analysis of detector pixels having different diameter and showing perimeter dependency in Sofradir SNAKE camera. (b) QE of SWIR and visible InGaAs cameras. (c) SEM image of flip-chip bonding process. (d) Snapshots of SNAKE camera [31], [32].	45
Figure 2.16: (a) Readout noise of C-RED 2 product with respect to frame rate and 22 e- noise was achieved at 400 FPS which is not shown in the graph. (b) Commercial C-RED 2 product [33].	46
Figure 2.17: (a) Dark current density of 15 μm pitch FLIR camera at different temperatures. (b) Equivalent readout noise in terms of electrons of pixel's dark current density for various pixel pitches. (c) 1920x1080 image captured by FLIR camera [15].	47
Figure 2.18: (a) Proposed InGaAs p-i-n diode structure including InAlAs barrier. (b) Dark current levels obtained from different mesa sizes [34].	49
Figure 2.19: (a) Dark current of $\text{In}_{0.83}\text{Ga}_{0.17}\text{As}$ photodetector having InAlAs grading layer. (b) QE of the proposed detector. (c) Images captured by extended SWIR InGaAs photodetector [35].	50
Figure 3.1: (a) Epilayer structure utilized in planar type InGaAs photodetectors. (b) Epilayer structure utilized in mesa type InGaAs photodetectors.	52
Figure 3.2: METU III-V Riber Epinat MBE Reactor.	54
Figure 3.3: XRD and rocking curve simulation result of a wafer utilized in this work.	57

Figure 3.4: Representative dark current of test detectors under different doping concentration of absorber layer. 59

Figure 3.5: Representative photocurrent of test detectors under different doping concentration of absorber layer. 59

Figure 3.6: (a) Cross section view of epilayer after Zn diffusion. (b) Top view of epilayer after Zn diffusion. 60

Figure 3.7: “DAG810” substrate grinding machine utilized for substrate removal. 64

Figure 3.8: Schematic representing substrate removal process. 64

Figure 3.9: (a) Cross section view of epilayer after all mesa processing steps. (b) Top view of epilayer after all mesa processing steps. 66

Figure 3.10: I-V curve of 25 μm pitch planar detectors at 20 and 25 $^{\circ}\text{C}$ 67

Figure 3.11: I-V curve of 15 μm pitch planar detectors at 20 and 25 $^{\circ}\text{C}$ 68

Figure 3.12: I-V curve of 25 μm pitch mesa detectors at 25 $^{\circ}\text{C}$ 69

Figure 3.13: Monochromator device and overall setup utilized in responsivity measurements. 70

Figure 3.14: Responsivity measurement setup overview. 71

Figure 3.15: Responsivity graphs of 25 μm pitch detectors at 20 $^{\circ}\text{C}$ 72

Figure 3.16: Responsivity graph of 15 μm pitch detectors at 20 $^{\circ}\text{C}$ 73

Figure 3.17: 640x512 25 μm pitch FPA- ISC0002 ROIC couple on LCC after having done substrate removal process. 74

Figure 3.18: Hot and cold object’s voltage difference histogram recorded under 5 ms integration time, and with F/2 lens. 75

Figure 3.19: Not optimized snapshots taken by 25 μm pitch 640x512 NIR/SWIR InGaAs camera. 76

Figure 4.1: Band diagram of conventional nBn photodetectors with existing current mechanisms in configuration [41].78

Figure 4.2: (a) First epilayer design of InGaAs nBn photodetector. (b) Corresponding band diagram of first design. (c) Final epilayer design of InGaAs nBn photodetector. (d) Corresponding band diagram of final design [39]. 79

Figure 4.3: (a) nBn and p-n InGaAs photodetectors' dark current for different surface velocities at $\tau_{\text{SRH}}=10 \mu\text{s}$. (b) nBn and p-n InGaAs photodetectors' dark current for different surface velocities at $\tau_{\text{SRH}}=1 \text{ ns}$. (c) Barrier thickness versus dark current in nBn detector at -0.1 V. (d) $I_{\text{dark}}-V$ curve of nBn detector for various barrier thicknesses [39]. 82

Figure 4.4: (a) Responsivity of nBn and p-n detectors. (b) QE of nBn and p-n detectors [39]. 83

LIST OF ABBREVIATIONS

IR	Infrared
ROIC	Readout Integrated Circuits
NIR	Near Infrared
SWIR	Short Wave Infrared
InGaAs	Indium Gallium Arsenide
FPA	Focal Plane Array
InP	Indium Phosphide
MWIR	Mid Wavelength Infrared
LWIR	Long Wavelength Infrared
VLWIR	Very Long Wavelength Infrared
FIR	Far Infrared
QWIP	Quantum Well Infrared Photodetector
EHP	Electron-Hole Pair
I_{photo}	Photocurrent
I_{dark}	Dark Current
QE	Quantum Efficiency
NEP	Noise Equivalent Power
SNR	Signal-to-Noise Ratio
F/#	F-Number
NETD	Noise Equivalent Temperature Difference
NEI	Noise Equivalent Irradiance
G-R	Generation-Recombination
SRH	Schockley-Read-Hall
BLIP	Background Limited Performance
HgCdTe	Mercury Cadmium Telluride

InSb	Indium Antimonide
CZT	Cadmium Zinc Telluride
Si	Silicon
GaAs	Gallium Arsenide
InAs	Indium Arsenide
Ge	Germanium
AlGaAs	Aluminium Gallium Arsenide
TEM	Transmission Electron Microscopy
FOV	Field of View
TEC	Thermoelectric Cooler
LPE	Liquid Phase Epitaxy
CTIA	Capacitive Transimpedance Amplifier
MBE	Molecular Beam Epitaxy
Zn	Zinc
MOCVD	Metalorganic Chemical Vapor Deposition
MOVPE	Metal Organic Vapor Phase Epitaxy
SEM	Scanning Electron Microscopy
UHV	Ultra High Vacuum
Be	Beryllium
LN₂	Liquid Nitrogen
RHEED	Reflection High Energy Electron Diffraction
XRD	X-ray Diffractometer
FWHM	Full Width Half Maximum
HCl	Hydrochloric Acid
UBM	Under Bump Metallization
LCC	Leadless Ceramic Carrier
ADC	Analog-to-digital converters

CHAPTER 1

INTRODUCTION

Infrared (IR) radiation basically covers 0.7-1000 μm wavelengths of the electromagnetic spectrum. Change in the electric dipole of molecules due to rotations and vibrations of atoms is the origin of infrared radiation and the objects including humans near room temperature emit radiation which falls into infrared region [1]. Therefore, high performance detection of infrared radiation is a vital issue in terms of various technological applications such as tracking, surveillance, night vision, hyperspectral imaging, weather estimation, astronomic observations, and also medical imaging. Infrared detection can be achieved by measuring the electrical signal arising from the variation in the temperature of the materials (thermal detectors) or the variation in the electron energy distribution of the materials which is a consequence of electron-photon interaction phenomena (photon detectors) [2]. However, due to the time required for heating and cooling issues, thermal detectors have slow response time and even if they possess low production cost, they are not fully adequate for high performance infrared detection. In that case, semiconductor technology based photon detectors come to the picture with their high speed operation. Growing semiconductor materials, fabrication of the photodetectors, integration to readout integrated circuits (ROIC) and cryogenic cooling necessity make photon detectors expensive, but still most of the effort in infrared photodetector industry belongs to the improvement of photon detectors since high performance is needed in wide range of the application areas. This thesis work includes fabrication and design development of Near Infrared (NIR)/Short Wave Infrared (SWIR) Indium Gallium Arsenide (InGaAs) photon detectors in focal plane array (FPA) level.

In this chapter, the basic properties of infrared radiation, types and operation methods of photon detectors with figure of merits are discussed in order to make more comprehensible analysis of the conducted work in the next chapters.

In Chapter 2, SWIR photodetector technology is examined with its own distinctive features and current status of especially InGaAs semiconductor material based detectors grown on Indium Phosphide (InP) substrates is mentioned.

Chapter 3 involves the fabrication procedure of 25 μm (in 640x512 format) and 15 μm pitch (in 1280x1024 format) InGaAs FPAs with planar and mesa process techniques, some challenges faced during the process development, and I-V, responsivity and imaging characterization results. Furthermore, a unique method proposed for nBn type InGaAs photodetectors in order to decrease the dark current particularly in mesa type photodetectors is explained.

Finally, in Chapter 4, all the discussions gone through are summarized with concluding remarks.

1.1. Fundamentals of Infrared Radiation

In infrared wavelengths (0.7-1000 μm), there are different kinds of radiation sources for the detection. Basically, the thermal emission from the objects having temperature greater than absolute zero (0 K) is the primary source for IR region. According to Kirchhoff's law of thermal radiation:

$$\alpha + \rho + T = 1 \quad (1.1)$$

where α is the absorbance, ρ is the reflectance and T stands for the transmittance of a material meaning that an incident radiation to an object can be absorbed, reflected or transmitted [3]. A blackbody is an object that absorbs all the incident electromagnetic radiation ($\alpha=1$, $\rho=0$, $T=0$) regardless of the wavelength. A blackbody is also an ideal emitter, and the re-emission of the absorbed energy at thermal equilibrium is called as blackbody radiation which can be stated as the main

source at IR region. Therefore, at any temperature, blackbody is the object that emits maximum possible spectral exitance (M_λ) which is the power radiated per unit area and per unit wavelength ($\text{Watt}/\text{cm}^2\text{-}\mu\text{m}$). The spectral exitance of a blackbody is defined by the Planck's law as follows

$$M_\lambda(\lambda, T) = \frac{2\pi hc^2}{\lambda^5 \left(e^{\frac{hc}{\lambda kT}} \right)} \quad (1.2)$$

where λ corresponds to the radiation wavelength, h is the Planck constant, c is the speed of the light, k is the Boltzmann constant and T corresponds to temperature of the object. If one draws a graph of spectral exitance with respect to wavelength and for various temperatures, the graph in Figure 1.1 is obtained [4].

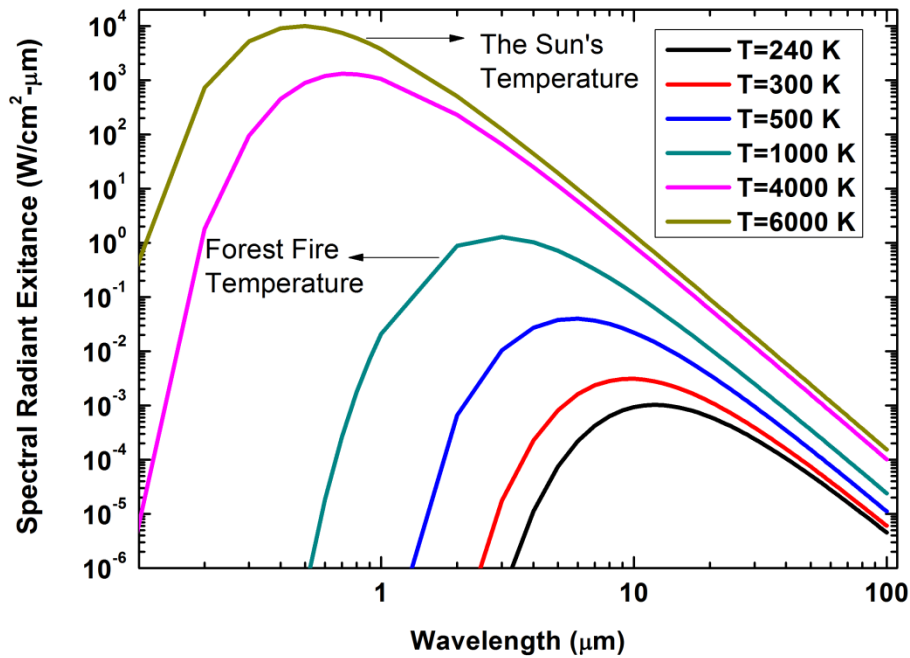


Figure 1.1: Spectral radiant exitance of a blackbody versus wavelength for different temperatures [4].

From Figure 1.1, some important conclusions can be deduced. First, blackbody objects at room temperature emit radiation totally in infrared region with around 10 μm peak

wavelength, so they can be identified by utilizing a thermal camera and making use of the temperature difference between the objects and background. Also, by increasing temperature, peak wavelength shifts towards shorter wavelengths and the area under the curve increases meaning that total exitance grows. As the temperature reaches the Sun's temperature, peak wavelength falls into visible light range (around 0.5 μm) which explains the humans' clear vision of the environment. Peak wavelength actually can be calculated by taking the derivative of Equation 1.2 with respect to wavelength and according to Wien's displacement law:

$$\lambda_{max} = \frac{2898 \mu\text{m} \cdot \text{K}}{T (\text{K})}. \quad (1.3)$$

Blackbody objects are the ideal absorbers and emitters as mentioned. However, most of the objects do not behave like blackbodies and they do not fully emit their absorbed energy, so we need to define a parameter to relate emission rates of the objects which is called the emissivity $\varepsilon (\lambda)$. Emissivity shows the ratio between the emitted energy from the object at temperature T and maximum emitted energy which can be obtained from a blackbody. Similar to spectral exitance, we also expect wavelength dependency in emissivity parameter, and if this dependency is known over the electromagnetic spectrum, emissivity is reduced to a single value as in Equation 1.4.

$$\varepsilon = \frac{\int_0^{\infty} \varepsilon(\lambda) M_{\lambda}(\lambda, T) d\lambda}{\int_0^{\infty} M_{\lambda}(\lambda, T) d\lambda} \quad (1.4)$$

In theoretical calculations, the objects are treated like gray bodies which do not show any variation in emissivity with respect to wavelength at least for some portion of the spectrum. For instance, human skin or glass is a gray body having emissivities of 0.98 and 0.94 respectively in infrared region.

Infrared radiation is also attenuated by atmosphere which is the usual transmission media during imaging with two mechanisms which are absorption of mainly O₂, H₂O and CO₂ gas molecules, and scattering from the particles such as dust or fog. If the size

of the particle is smaller than the wavelength Rayleigh scattering occurs, and it is inversely proportional to fourth power of the wavelength ($1/\lambda^4$), but if the size of the particle is larger than the wavelength Mie scattering takes place which is wavelength nonselective. Absorption of the gases has more crucial effect in infrared region, and the infrared spectrum is divided into subwavelengths or windows according to transparency of the atmosphere. The transmittance of the atmosphere at infrared wavelengths is shown in Figure 1.2 [3].

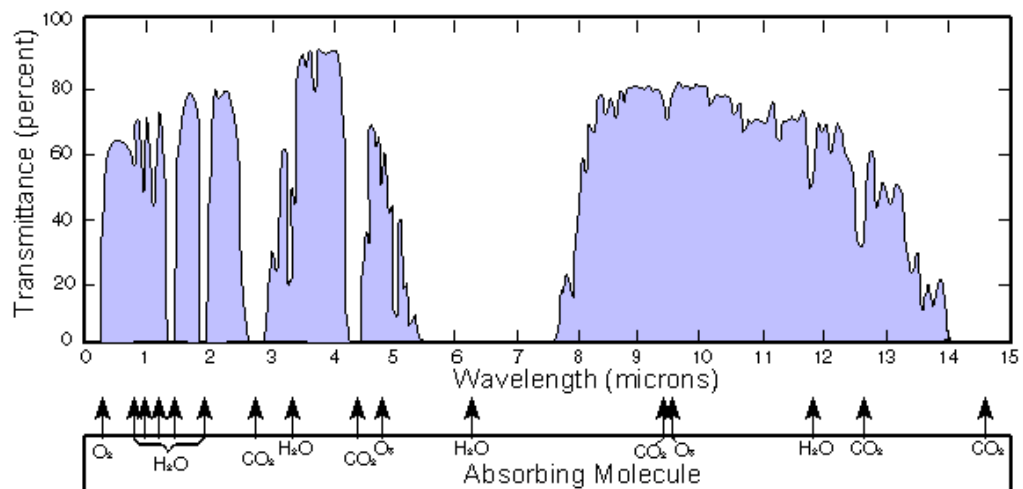


Figure 1.2: Atmospheric transmittance at infrared region [3].

Mainly because of the H₂O absorbance, atmosphere is not transparent at all to infrared radiation between 5-8 μm wavelengths. According to Figure 1.2, the subdivision of infrared region is as follows:

- 0.7 - 1 μm : Near Infrared (NIR)
- 1 - 3 μm : Short Wave Infrared (SWIR)
- 3 - 5 μm : Mid-wavelength Infrared (MWIR)
- 8 - 12 μm : Long Wavelength Infrared (LWIR)
- 12 - 20 μm : Very Long Wavelength Infrared (VLWIR)

- 20 - 1000 μm : Far Infrared (FIR).

By combining the transmission spectrum with the blackbody radiation curve, the deductions can be expanded. To illustrate, the change in the blackbody radiation of near room temperature objects (300 K) is higher in MWIR band compared to LWIR band which results in larger thermal contrast in MWIR imaging. This large thermal contrast is a good property in most of the time, but if we are trying to monitor hot and cold objects simultaneously, hot objects may saturate the ROIC capacitors at the average gain which does not allow for clear analysis during imaging. Also, high thermal contrast in MWIR band is achieved at the expense of reduced photon flux near room temperature objects. Similar investigations can be made for different temperatures and infrared bands.

Another significant result is that the radiation coming from the room temperature objects is very low at the SWIR band, but still the Sun is a power source in those wavelengths and the cameras produced to operate in this region benefits especially from the Sunlight. This is actually the reason why the images taken by these cameras resemble to the ones taken with visible cameras or usual photograph machines. There are also other radiation sources utilized in SWIR band, and the further information will be given in Chapter 2.

1.2. Infrared Photodetectors with Figure of Merits

Infrared photodetectors are the devices that can sense the infrared radiation by creating electrical current or voltage as an output signal which can be measured by the characterization systems. In thermal detectors, the infrared radiation varies a physical property of the materials by heating the detector and creates an electrical signal. The most common types of thermal detectors are microbolometers, thermocouples and pyroelectric detectors [2]. In microbolometers, the resistance of the material is changed. Thermocouples or thermopiles (multiple connections of thermocouples pairs) detect a thermoelectric voltage change generated between the junctions of the material with thermoelectric effect. Finally, in pyroelectric detectors a pyroelectric voltage is obtained as a result of internal electrical polarization change yielding charge accumulation. These

detectors are able to work at room temperature and do not need any cooling except for temperature stabilization concerns, but they have very slow response time and high speed operation is not realizable.

Opposite to thermal detectors, photon detectors operate with electron-photon interaction principle which is an abrupt process and fast response times in the devices are easy to achieve. Semiconductor materials having energy bandgap (E_g) are utilized in photon detectors where the incoming photons with sufficient energy excite the electrons to the conduction band states and left a hole in their initial states. In fact, different excitation mechanisms are present in semiconductors which give names to photodetector types. These main mechanisms are illustrated in Figure 1.3 which will be further investigated [5]. In intrinsic detectors, the electron in the valence band is directly excited to conduction band which can be stated as interband transition. Extrinsic detector operation is based on excitation of electrons residing in impurity states. Intersubband transition between the confined energy states in quantum well infrared photodetectors (QWIPs) is another important free carrier generation mechanism.

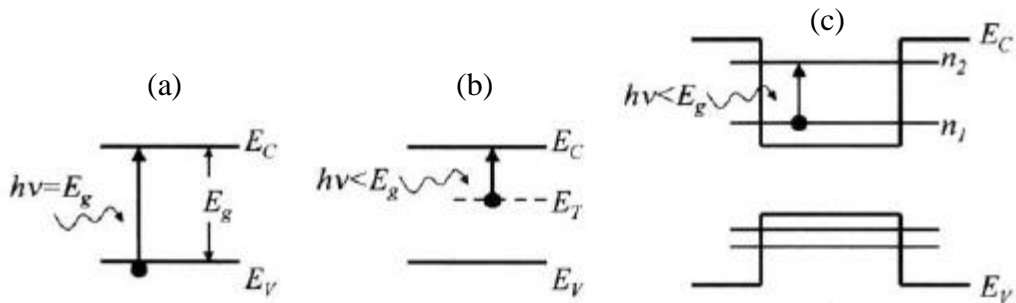


Figure 1.3: (a) Interband excitation mechanism in intrinsic photon detectors. (b) Excitation from an impurity or a trap energy state to conduction band in extrinsic photon detectors. (c) Intersubband excitation between confined energy states of QWIPs [5].

Under an external or already existing internal electric field, photo-generated electron-hole pairs (EHPs) are collected by the contact regions generating an electrical current called photocurrent (I_{photo}). There is also some current flowing through the photodetector

device under no illumination due to thermal excitation of the carriers when the temperature is above absolute zero (0 K) and it is called the dark current (I_{dark}). The $I_{\text{photo}}/I_{\text{dark}}$ ratio of the photodetector basically reflects the sensitivity of the device since the useful signal from the photo-generated carriers can be extracted when their number is significantly larger than thermally generated carriers. Therefore, decreasing dark current of the photon detectors is a vital issue. In order to reduce the thermal generation rate, most of the photodetector types require cryogenic cooling which increases the overall system cost and decreases the compactness. Now, figure of merits of photodetector devices will be presented.

1.2.1 Responsivity

Responsivity (R) is the parameter that indicates how much of the incident radiation can be transferred into output signal, so it is defined as the ratio of output signal to incoming radiation where the output signal is electrical current (A) or voltage (V) and input signal can be expressed in terms of radiation power (W) as given in Equation 1.5:

$$R = \frac{\text{Output Signal}}{\text{Incident Radiation}} = \frac{I_{\text{photo}}}{\varphi} \quad (1.5)$$

Since the output signal in photon detectors is the photocurrent, the most encountered unit of the responsivity becomes A/W. Responsivity actually depends on the wavelength in which case it is called spectral responsivity. The energy of a photon decreases with wavelength, and for a certain incident radiation power, the number of photons in the coming energy packet increases with increasing wavelength. That is why the responsivity curves show linear relationship with wavelength. In photon detectors, the responsivity and the wavelength relationship can be obtained by manipulating the Equation 1.5 to obtain:

$$R = \frac{\eta g \lambda}{1.24} \quad (1.6)$$

where η represents the quantum efficiency (QE) of the detector which can be defined as the ratio of the number of excited electrons to the number of striking photons to the material, g corresponds to the gain of detector which is actually the number of roundtrips that an electron can make before the recombination process occurs and λ is the wavelength having μm unit.

1.2.2 Noise

As a general description, noise can be stated as the random oscillations in the observed signals. Due to the randomness, it is defined as a random variable and measured in terms of root mean square. Noise shows frequency dependent behavior and it is provided with the frequency bandwidth (Δf) in which the measurement is taken. It can be measured in terms of voltage (v_n) or current (i_n). The well-known noise mechanisms are Johnson (thermal) noise, shot noise, capacitor (kTC) noise and pink (1/f) noise.

Johnson noise or thermal noise comes from the randomness in the thermal velocity of the charge carriers for temperatures above absolute zero. It can be calculated as:

$$v_n^2 = 4kTR\Delta f \text{ or } i_n^2 = \frac{4kT\Delta f}{R} \quad (1.7)$$

where R corresponds to the resistance of the detector at the operating conditions.

Shot noise occurs in the devices with potential energy barrier. The photo-generated carriers show random behavior to overcome this barrier as the photon arrival process is also random. The shot noise formulation is performed with

$$i_n^2 = 2qI\Delta f \quad (1.8)$$

in which q is the electric charge and I can be taken as the sum of dark and photocurrent of the device.

Capacitor noise is another noise mechanism. Practical capacitors exhibit shunt resistance displaying complex impedance which varies with the frequency. Integrating

the real part of this impedance in all frequency bandwidth an inserting it into the thermal noise formula gives us the noise of the capacitor which is shown in Equation 1.9:

$$v_n^2 = \frac{kT}{C} \quad (1.9)$$

where C is the capacitance value. This capacitor noise may be important when the noise of the photodetector is low compared to the noise exhibited by the integration capacitor of the ROIC connected to each detector pixel. Therefore, producing low noise ROICs is another important area in infrared devices.

Pink or 1/f or flicker noise is a significant noise mechanism at low frequencies. It may be associated with the impurities or trap states introduced from the material itself or during the fabrication, but still its stems are not fully identified. This noise mechanism can be modeled as:

$$i_n^2 = \frac{CI^\alpha \Delta f}{f^\beta} \quad (1.10)$$

in which C is proportionality constant and α and β are material/device dependent empirical constants.

In case the dominant noise mechanisms are Johnson, shot and 1/f noise, the total noise current is expressed as

$$i_{ntotal}^2 = i_{nthermal}^2 + i_{nshot}^2 + i_{n1/f}^2. \quad (1.11)$$

1.2.3 Noise Equivalent Power and Detectivity

Noise equivalent power (NEP) is the radiation power constituting the output signal at the same level with the noise signal meaning that it is the power which makes the signal-to-noise ratio (SNR) of the photodetector 1. NEP is accepted to be the minimum sensible photon flux in the photon detectors. Mathematically, it is expressed as:

$$NEP = \frac{i_{noise}}{R_i} = \frac{v_{noise}}{R_v}. \quad (1.12)$$

It can be easily observed that NEP needs to be small in photodetectors. In order to make the concept more understandable, detectivity (D) parameter is defined as the 1/NEP term where it would be better for the detector if it is large. However, detectivity depends on the photon flux coming to the detector (ϕ), total detector area (A_d) and also Δf of the noise measurement, so instead of providing these information with the detectivity parameter, a normalization in the formulation is made in order to compare different types of detectors. The normalized detectivity is named as specific detectivity (D^*) and given as:

$$D^* = \frac{\sqrt{A_d \Delta f}}{i_{noise}} R_i. \quad (1.13)$$

D^* is therefore independent of A_d and Δf . An FPA is located at the focal point of the lens used in the imaging system. The received photon flux depends on the optical aperture specified by the F-number (F/#) which is given as f/D_{as} term where f is the focal length of the lens, and D_{as} is the diameter of the lens aperture. Consequently, with larger D_{as} or lower F/#, the collected photon number is increased and I_{photo} of the detector varies inversely with the square of the F/# ($I_{photo} \propto 1/(F/\#)^2$). Returning back to specific detectivity case, R_i depends on I_{photo} , and i_{noise} changes with $\sqrt{I_{photo}}$ if dominated by the shot noise. Then, the whole D^* shows $\sqrt{I_{photo}}$ and $1/(F/\#)$ dependency accordingly. Hence, when D^* of a photodetector FPA is presented, F/# used in the optics system should also be provided.

1.2.4 Noise Equivalent Temperature Difference and Irradiance

Noise equivalent temperature difference (NETD) is the temperature difference between the object and background which generates SNR=1. In other words, it is the minimum sensible temperature difference in the detector, and smaller NETD is better to identify each object in the field of view. NETD is formulized as:

$$NETD = \frac{(4(F/\#)^2 + 1) \sqrt{\Delta f}}{\sqrt{A_D} \int_0^\infty T(\lambda) D^*(\lambda) \frac{dM_{\lambda Target}(\lambda)}{dT} d\lambda} \quad (1.14)$$

where $T(\lambda)$ is the transmission spectrum of the atmosphere together with the optics. The unit of NETD is Kelvin. Also, note that D^* displays the same linear relation with wavelength as in responsivity since R term is included in D^* expression. From NETD equation, some important conclusions can be achieved. First, by reducing the pixel pitch and detector area, we increase NETD in photodetectors which is not a good result even if the resolution of the system increases. Furthermore, Δf in NETD equation does not correspond to noise measurement bandwidth, but it is related to integration time (τ) of the ROIC capacitors ($\Delta f=1/2\tau$). By decreasing the integration time, the frame rate of the imaging is increased, but NETD increases at the same time, so this tradeoff should be taken into consideration.

NETD is valid for the detectors which benefits from the blackbody radiation difference of different object temperatures. As mentioned before, in SWIR band, the blackbody radiation of the objects is not a source due to low photon flux, so NETD parameter cannot be defined for SWIR photodetectors. Instead of NETD, noise equivalent irradiance (NEI) is provided with SWIR detector which is the minimum amount of photon flux that should reach the system to have SNR=1. Similar to NETD, NEI can be described in terms of photons and watts as:

$$NEI_{photons} = \frac{Noise}{A_{optics} \tau} \text{ or } NEI_{watts} = \frac{Noise}{A_{optics} \tau} \frac{hc}{\lambda} \quad (1.15)$$

where τ is again the integration time of the system [6].

1.3. Infrared Photon Detector Types

Infrared photon detectors' working mechanism is related to the excitation of the electrons to the conducting energy states of the semiconductor material with the energy provided by the absorbed photons of the incoming radiation. Then, the generated EHPs

are collected from the metal contacts by the help of an externally applied or internally formed electric field. Photon detectors are first categorized according to the way of creating this electric field in the device which are named as photoconductor and photovoltaic detectors which will be discussed in detail.

Photoconductor Detectors: In this type of detectors, the photogenerated EHPs under the photon flux ϕ reach the contact regions with the applied bias voltage V as seen in Figure 1.4. The bias voltage should be adjusted such that the generated electron and holes are able to drift to the contacts for collection without exposing to recombination process. The generated carriers simply increase the conductivity of the semiconductor material which in return increases the total current flowing through the device ($I_{\text{dark}}+I_{\text{photo}}$). This current is reflected as an output voltage across the connected load resistance R . By starting from change in the conductivity, I_{photo} can be calculated as:

$$I_{\text{photo}} = qg_{\text{op}}wtL \left(1 + \frac{\mu_p \tau_n}{\mu_n t_{\text{tr}}} \right). \quad (1.16)$$

In this equation, g_{op} corresponds to the EHPs generated in every second per unit volume (EHP/cm³-s), w,t,L are the dimensions of the material, μ_n and μ_p are the mobilities of the electrons and holes respectively, τ_n is the electron lifetime and t_{tr} stands for the transit time of the electrons across the sample which can be expressed as L divided by velocity of the electrons ($t_{\text{tr}} = L/(v_e=\mu_n E)$). As can be noticed easily, $qg_{\text{op}}wtL$ term already gives a current value, so $(1 + \frac{\mu_p}{\mu_n} \frac{\tau_n}{t_{\text{tr}}})$ expression basically multiplies this current value and that is why it is called the gain (g) of the photodetector. The gain in the photoconductor detectors comes from the fact that the mobility of the hole is low compared to the electron. The electron reaches the contact before the hole, however, in order to preserve the charge neutrality, an electron must be reinjected to the sample. The roundtrips that the electron makes until the hole is collected from the the contact basically constitutes this gain expression. Gain may seem to be an advantage of these detectors, but still I_{photo} is strictly dependent to the applied bias voltage and electric field which is a major disadvantage. In order to collect the generated carriers, a large bias may be required

which increases the power consumption in the device and may not allow the producer to make large format FPAs.

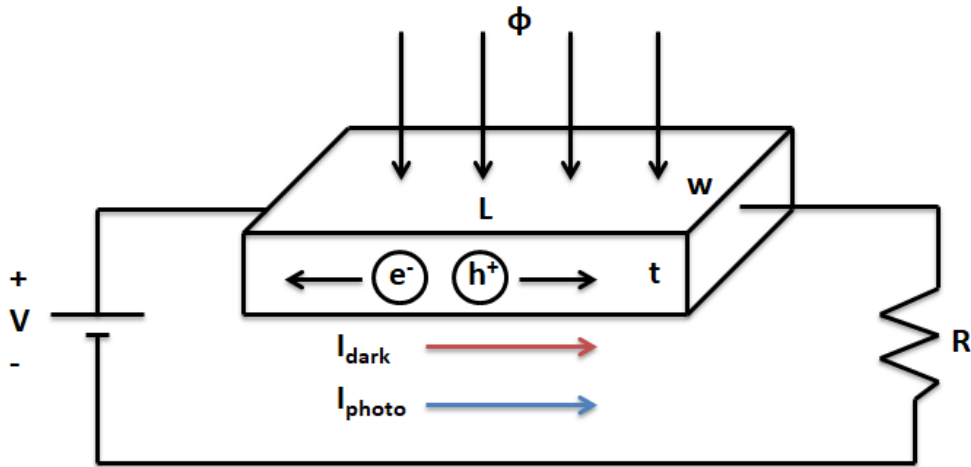


Figure 1.4: Basic representation of photoconductor detector working mechanism under biasing circuit.

Photovoltaic Detectors: This type of detectors made use of basic diode structures called photodiodes. The operation principle of these detectors basically relies on physics behind p-n or p-i-n junctions. A schematic of a p-n junction is presented in Figure 1.5 to explain the photo-generation process.

In a p-n junction, large hole concentration in p doped material and large electron concentration in n doped material constitute a diffusion gradient in the device leading to a depleted region just around the junction. In the depletion region, a built-in electric field exists. Photodiodes are used at reverse bias voltages to minimize the dark current. Under no illumination, I_{dark} is the current we measure from the device due to the thermal excitation. There are different components of this dark current. First one is the diffusion current associated with the radiative and Auger recombination processes. If the thermally generated carriers are able to diffuse to the depletion region, they contribute to the dark current in the device with the presence of high electric field. Therefore, these carriers should be generated within the electron or hole diffusion lengths which are labeled as L_n and L_p , respectively in Figure 1.5.

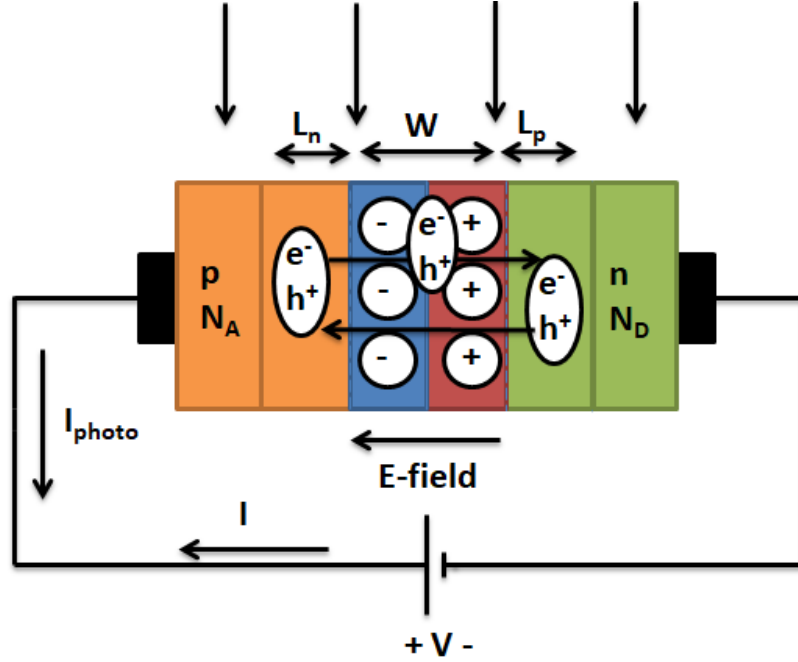


Figure 1.5: A representative photodiode structure showing the photocurrent generation process.

By obtaining the carrier concentration distribution along a long device and applying the boundary conditions, the diffusion current is expressed as:

$$I_{diff} = qA \left(\frac{L_p n_i^2}{\tau_p N_D} + \frac{L_n n_i^2}{\tau_n N_A} \right) \left(e^{\frac{qV}{kT}} - 1 \right). \quad (1.17)$$

In Equation 1.17, τ_n and τ_p are the lifetimes of the electron and holes, N_A and N_D stand for the p and n doping concentration and n_i corresponds to the intrinsic carrier concentration of the material used. It can be seen that due to n_i^2 term ($\propto e^{-E_g/kT}$), diffusion current shows a strong dependence to the temperature. MWIR and LWIR photodetectors possessing low bandgap values have high intrinsic carrier concentration, and they require cryogenic cooling to reduce diffusion current. However, SWIR photodetectors have higher bandgap due to shorter cutoff wavelengths, and they can be operated at room temperature. Another observation is that one of $n_i^2/\text{doping concentration}$ term in Equation 1.17 can be ignored by increasing one of the doping concentration much or by

selecting a high bandgap material at one side of p-n junction meaning that by utilizing a heterojunction structure consisting of different materials.

Second dark current mechanism is the generation-recombination current in the depletion region or named as G-R current. Impurities or defects introduce trap energy states in the bandgap of the materials. Electrons generated in the depletion region can easily couple to those states since lower energy is required compared to coupling directly to valence band states and contribute to the dark current. The whole process is known as Shockley-Read-Hall (SRH) recombination process, and G-R current can be also called SRH current. For a single trap state located near to midpoint of the bandgap, this current can be calculated as:

$$I_{G-R} = \frac{qAWn_i}{2\tau_{G-R}} \quad (1.18)$$

when the p/n doping concentrations are similar. In equation 1.18, W is the depletion width in the diode and τ_{G-R} corresponds to the G-R lifetime. G-R current shows less dependency to the temperature due to n_i term instead of n_i^2 term, so while reducing the temperature of the device, it can be dominant after a certain point as diffusion current decreases more rapidly. Also, in photodetectors which do not satisfy lattice matched condition of the utilized materials in the epi-structure, G-R may be the dominant mechanism due to reduced G-R lifetime.

Band to band and trap assisting tunneling currents are other parts of the dark current in photodiodes. Under excess doping concentration, valence band in the p side can be aligned with the conduction band in the n side which allows carrier tunneling between these bands directly or by the help of trap states in the bandgap. Therefore, this current may be dominant at low bandgap materials with high enough bias voltages.

Similar to the dark current, photo-generated EHPs under illumination and within the thickness composed of electron and hole diffusion lengths and depletion width are swept to contact regions via high electric field. Hence, photocurrent can be easily expressed as:

$$I_{photo} = qAgop(Lp + Ln + W). \quad (1.19)$$

The important thing is to select this total thickness properly so that we can generate as much as I_{photo} possible. However, the thickness parameters show the same effects on dark current components and the tradeoff between I_{photo} and I_{dark} should be investigated carefully to maximize SNR of the photodetector. Under reverse bias voltages, I_{photo} and I_{dark} flow in the same direction and the sum of the currents is measured. I-V curve of a photodiode is presented in Figure 1.6 for dark and illuminated cases.

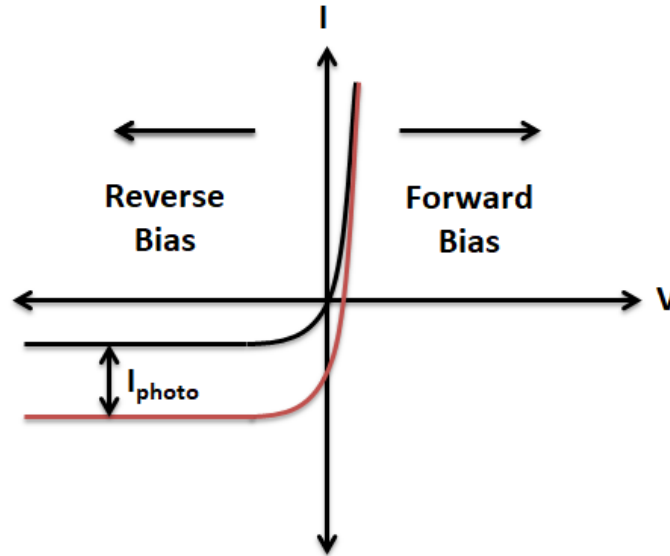


Figure 1.6: I-V characteristic of photovoltaic or photodiode type detectors under dark and illuminated conditions.

Some discussions may be added which are valid for both photoconductor and photovoltaic type detectors. To begin with, an additional noise mechanism is defined in photodetectors considering the trapping states in bandgap. The oscillations in the rate of carrier trapping of these states cause randomness in the creation of EHPs leading to G-R noise in photodetectors. It can be modeled as:

$$i_{n-gr}^2 = 2qIg\Delta f \quad (1.20)$$

where I is the total current flowing through the device and it includes both dark and photocurrent which is logical since these oscillations can be associated with thermal and optical excitations. It can be noticed that G-R noise expression resembles to shot noise expression except that the current is the total current and gain term appears. Also, taking into account both generation and recombination process, the expression is multiplied with 2 just in photoconductor detectors since the recombination process is not correlated to generation process and takes part in noise of the detector [2]. In photovoltaic detectors, this multiplication does not occur and they have less G-R noise.

Background limited performance (BLIP) is another concept that should be mentioned. Apart from the useful photon flux, the detector receives radiation from the background which contributes to optical generation rate and background photon flux is usually higher than targeted photon radiation. If the sufficient cooling is applied to the detector and thermal generation is suppressed, background radiation becomes the primary noise source. The temperature that the thermal generation is equal to the background photo-generation rate is defined as BLIP temperature. At this temperature and below, G-R noise can be counted as the dominant noise mechanism and the current term in G-R noise is related to the background photon flux. Hence, by inserting this noise to D^* expression (Equation 1.13) and doing the proper transformation in variables, we conclude with BLIP detectivity as:

$$D_{BLIP}^* = \frac{\lambda}{2hc} \sqrt{\frac{\eta}{\varphi_b}}. \quad (1.21)$$

In BLIP detectivity expression, φ_b represents the background photon flux per unit area (photons/cm²-sec). An important observation is that at BLIP conditions, detectivity can be increased by only quantum efficiency improvement as the other parameters are just constants. This situation reflects the ultimate detector performance and we always want to obtain high quantum efficiency in the detectors to improve it. In addition, Equation 1.21 gives BLIP performance in photoconductors. Due to the correlation in

recombination and generation processes in photovoltaic detectors, D^*_{BLIP} becomes $\sqrt{2}$ times greater in photovoltaic ones [2].

Photon detectors can also be categorized in terms of excitation mechanisms as mentioned in Chapter 1.2. Now, more detailed information will be provided for each type.

Intrinsic Photon Detectors: These detectors rely on direct transition of electron from valence band to conduction band known as interband transition. Therefore, the bandgap of the absorber material in the design determines the cutoff wavelength of the absorption which can be easily calculated as:

$$\lambda_{cutoff} (\mu m) = \frac{1.24}{E_g (eV)}. \quad (1.22)$$

As indicated before, in order to extend the cutoff wavelength, lower bandgap materials need to be selected which results in also higher thermal generation rates and intrinsic carrier concentration which is the reason for the requirement of cooling especially in MWIR and LWIR photodetectors. The most outstanding detector technologies utilizing interband transition can be listed as Mercury Cadmium Telluride (HgCdTe), InGaAs and Indium Antimonide (InSb) photodiodes.

HgCdTe is currently the leading material in photodetector technology with its unique advantages over the remaining semiconductor materials. First of all, it is the combination of HgTe metal (no bandgap) and CdTe II-VI semiconductor materials ($E_g=1.5$ eV). This allows us to tune the cutoff wavelength between 1-20 μm by changing the mole fraction of the material so that HgCdTe photodetectors can cover all SWIR, MWIR and LWIR bands. The most important advantage while changing the mole fraction is that there occurs a very small change in the lattice constant of the material (around 0.2% change in lattice constant between CdTe and $Hg_{0.8}Cd_{0.2}Te$) [7]. Therefore, lattice matched condition with Cadmium Zinc Telluride (CZT) substrates is not broken which also enables to produce dual or multiband (multicolor) HgCdTe photodetectors

sensing different IR bands on the same detector structure because of the high absorption coefficient in all of them. There is significant work dedicated to improve HgCdTe photodetector technology and there are efforts towards overcoming instability and nonuniformity problems as well as growing the detector on alternative substrates such as Silicon (Si) or Gallium Arsenide (GaAs) in order to avoid the high cost of CZT substrates.

InSb photodiodes have long history than HgCdTe ones. InSb material has 0.23 eV bandgap at 80 K corresponding to around 5.4 μm cutoff wavelength and they offer similar performance with HgCdTe photodetector in MWIR band and in FPA level. The only disadvantage that the cutoff wavelength cannot be adjusted since it is a binary semiconductor. In the literature, 1 nA/cm^2 dark current densities at 77 K are presented [8] and 10 μm pitch FPAs in 1920x1536 format with less than 0.8 pA dark current at 77 K have been fabricated [9].

InGaAs photodiodes provide high performance at SWIR band like HgCdTe counterparts. It is a ternary semiconductor material composed of Indium Arsenide (InAs) and GaAs. The major advantage of these detectors is that they become lattice matched to commercially available InP substrates at 0.53 In mole fraction. The cutoff wavelength of $\text{In}_{0.53}\text{Ga}_{0.47}\text{As}$ material is 1.68 μm at 300 K. High responsivity and QE values are achievable via InGaAs photodiodes. Lower substrate and fabrication costs make them proper choice for SWIR band IR detecting. The current status of InGaAs photodetectors will be presented in Chapter 2 considering all aspects.

Extrinsic Photon detectors: Extrinsic detectors are not as popular as the other type of photon detectors. Their operation relies on the excitation of the carriers residing in the impurity states, so they require less energy for the excitation and the cutoff wavelengths can extend to a few hundred μm . However, extreme cooling requirements beyond 20 μm cutoff wavelengths is the most critical issue. The most suitable materials utilized in extrinsic detectors are Si and Germanium (Ge) which can be doped to proper levels [10].

Quantum Well Infrared Detectors: QWIPs benefit from the quantum confinement property of the carriers where low bandgap materials are sandwiched between high bandgap materials in a periodic array and subbands are formed by the localization of the energy states. The electrons confined at these subbands can be excited directly to continuum states and collected with the applied bias voltage which can be seen from Figure 1.7 or they can be excited to higher energy subband states and then tunnel through the continuum [10]. This is a simple explanation of QWIPs' operating principle indicating that QWIPs belong to photoconductor type detector family. They are known with their high uniformity, stability and pixel operability advantages and they can be designed to operate in the entire IR band. However, QWIPs have very low QEs mostly less than 10% since horizontally polarized photons are needed for absorption, so they cannot offer higher performances than HgCdTe photodiodes. The widely used material systems in QWIPs is Aluminium Gallium Arsenide (AlGaAs)/GaAs. 1280x1024 format 19.5 μm pitch MWIR and LWIR AlGaAs/GaAs QWIPs have been presented with 3.8% QE [11]. Furthermore, very high QE (31%) with an alternative material system (InP/InGaAs) has been achieved [12].

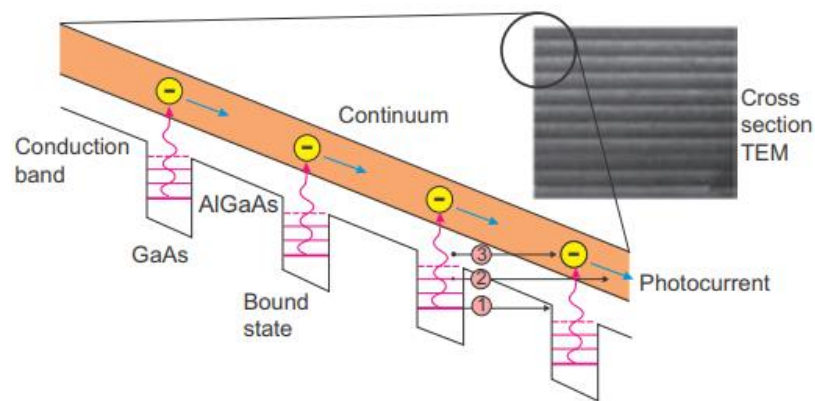


Figure 1.7: Representation of AlGaAs/GaAs QWIPs under applied voltage and Transmission Electron Microscopy (TEM) image from the fabrication [10].

Type II Superlattice Detectors: Superlattice detectors are actually one of the newest detector technologies which might have potential to achieve closer performance to HgCdTe photodiodes in MWIR and LWIR bands. Basically, when two lattice matched materials with misaligned band structures (the conduction band minimum of one material stays below the valence band maximum of the other) are brought together, minibands in the energy band diagram can be obtained due to overlapping wavefunctions of the electron and holes. This is pictured in Figure 1.8 [10]. In superlattice detectors, the excitation between the minibands is sensed. Theoretically, these detectors offer high QE, high responsivity and reduction in dark current mechanisms (compared to HgCdTe) such as tunneling current due to higher effective mass (m^*) or Auger recombination due to induced strain. However, superlattice detector technology has not yet been able to deliver the theoretical promise, and currently, researchers are working on developing fabrication procedures to achieve high performance. GaSb/InAs and InGaSb/InAs can be counted as the most widely used material systems in this detector technology. Also, by playing with the thickness of the materials, the energy difference between the minibands can be adjusted.

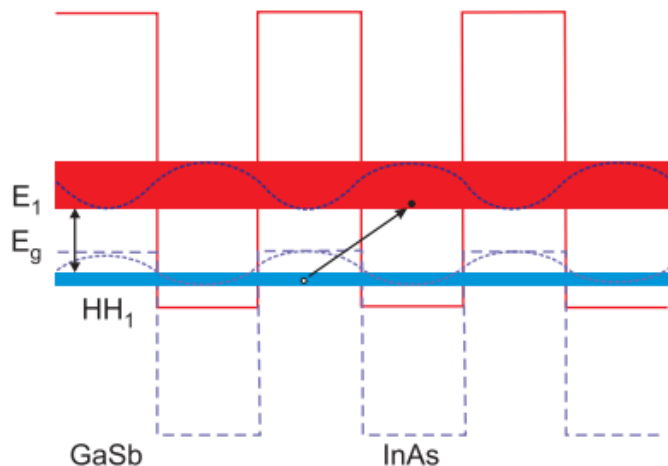


Figure 1.8: InAs/GaSb materials based superlattice detector band diagram showing the formation of minibands and excitation process [10].

1.4. Scope and the Motivation of the Work

Even though InGaAs photodiodes are well studied and developed, this detector technology still needs improvement especially to be used in night imaging. By utilizing planar process method, dark current densities have recently been reduced to a few nA/cm² orders, but mesa type processes, which offer lower crosstalk between the pixels and are compatible with dual color applications, have higher dark current densities compared to the planar type structures. Addressing some of these issues, planar and mesa fabrication procedures were developed for large format/megapixel NIR/SWIR InGaAs photodetectors. Also, a unique method was proposed numerically which shows the possibility of enhancing characteristics of InGaAs photodetectors.

CHAPTER 2

NIR/SWIR PHOTODETECTOR TECHNOLOGY AND STATUS

This chapter is dedicated to application areas, properties and advantages of NIR/SWIR photodetector technology. It also includes the material systems utilized for SWIR detection and state-of-the-art photodetectors fabricated from them, so an overall outlook to the recent technology is presented.

2.1. Application Areas and Properties of SWIR Photodetectors

SWIR radiation cover 1-3 μm wavelengths of the infrared spectrum as defined in Chapter 1. It is also stated that blackbody radiation emitted by the room temperature objects is negligible in SWIR band, and thermal radiation is not a source for detection. The spectral photon exitance or number of photons striking to unit area material per second for each wavelength and different temperatures is depicted in Figure 2.1. It clearly indicated very low photon flux level of room temperature objects at SWIR band, and even there is more than 5 order of magnitude difference in photon flux between 1000 K and 6000 K (the Sun) temperatures. However, it also shows that the Sun is a very powerful source in short wavelengths. SWIR photodetectors make use of the reflected Sunlight from the objects around us in daylight applications like visible cameras we use in our daily life. This is also the explanation of why SWIR photodetector images look like images taken by a usual photograph machine.

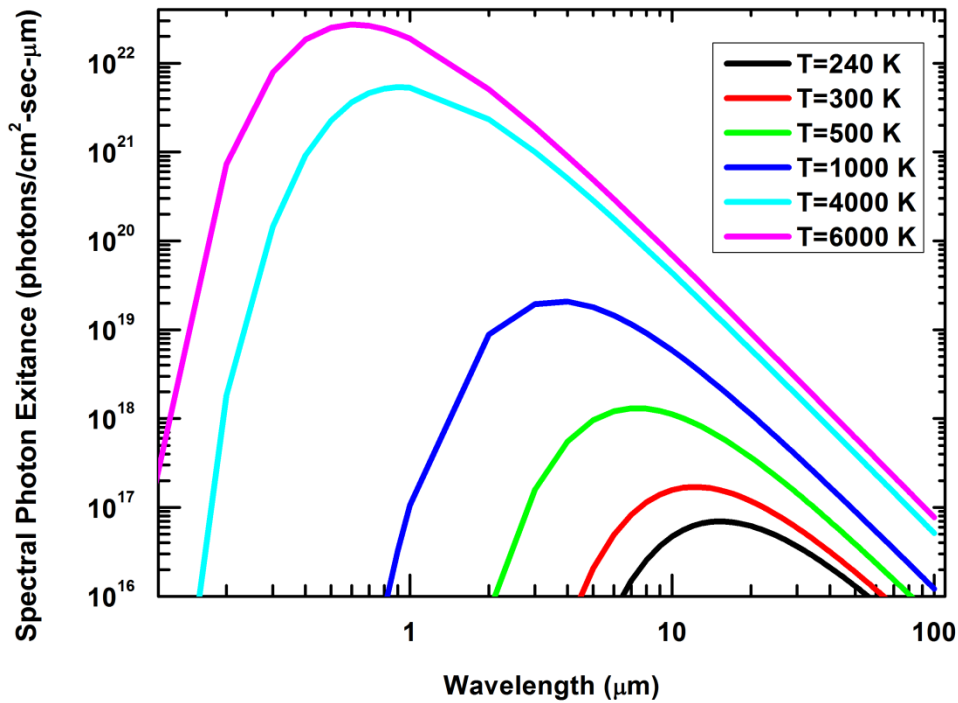


Figure 2.1: Spectral photon exitance curves for different blackbody temperatures.

Although visible and SWIR images are quite similar, one of the biggest advantage of SWIR photodetectors that they yield better images compared to the visible ones due to their longer wavelengths that reduce Rayleigh scattering which is inversely proportional to 4th power of the wavelength ($\propto 1/\lambda^4$). Therefore, SWIR cameras are able to acquire high quality images through haze and dusty environment with the reduction in attenuation and high performance surveillance becomes their major application area. As an illustration, visible and SWIR cameras monitoring the same hazy atmosphere over sea were presented in Figure 2.2 [13]. It is obvious that visible camera cannot provide good quality image in this misty environment and most of the located targets in the field of view (FOV) cannot be identified. However, due to less scattering, a clear image of shore was obtained and a ship at the farthest point of FOV was detected by a SWIR camera.

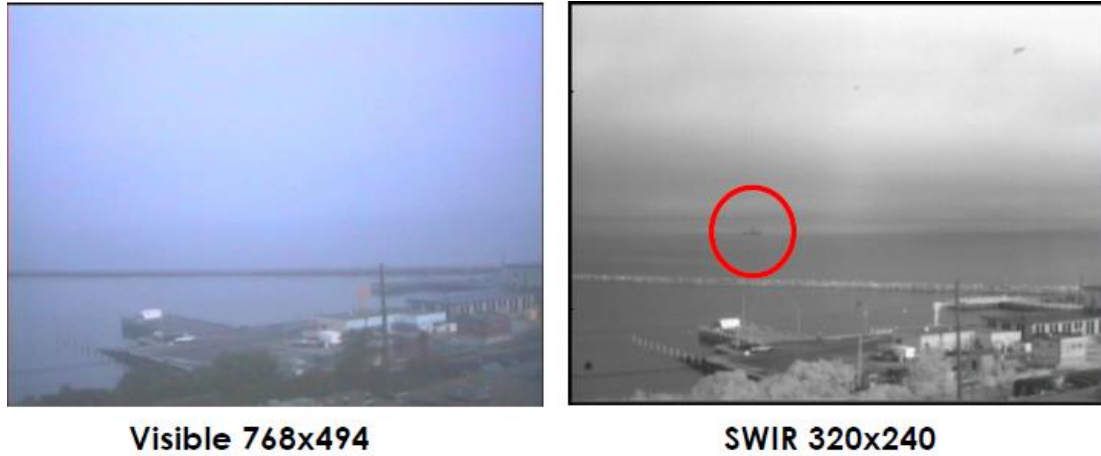


Figure 2.2: Visible and SWIR cameras looking to the same FOV in a hazy environment [13].

Furthermore, overtones of molecular vibrations absorb in SWIR band, and it provides signature identification for molecules including O-H, C-H and N-H chemical bonds [14]. Therefore, hyperspectral imaging is another important application area of SWIR detectors where they can be made to identify recycled plastics, moisture level or contamination of agricultural products by dirt etc. (NIR spectroscopy). In the military applications, same effect can be used to bring to light camouflaged living things. Moreover, active illumination from LEDs and eye-safe lasers is another source for NIR/SWIR band detection [13]. Lasers operating within eye-safe region (beyond 1.4 μm) where laser beam does not focus on retina such as Yag lasers and lasers utilized for specifically fiber optic communication wavelengths (1.31 and 1.55 μm) are the origins of this active illumination which needs to be detected by SWIR photodetectors. In fact, fiber optic light sensing can be counted as the driving force in the development of SWIR photodetector technology in the first place and it is currently a major application area. A SWIR photodetector identifying 1550 nm wavelength laser beam with high quality is presented in Figure 2.3 [15].

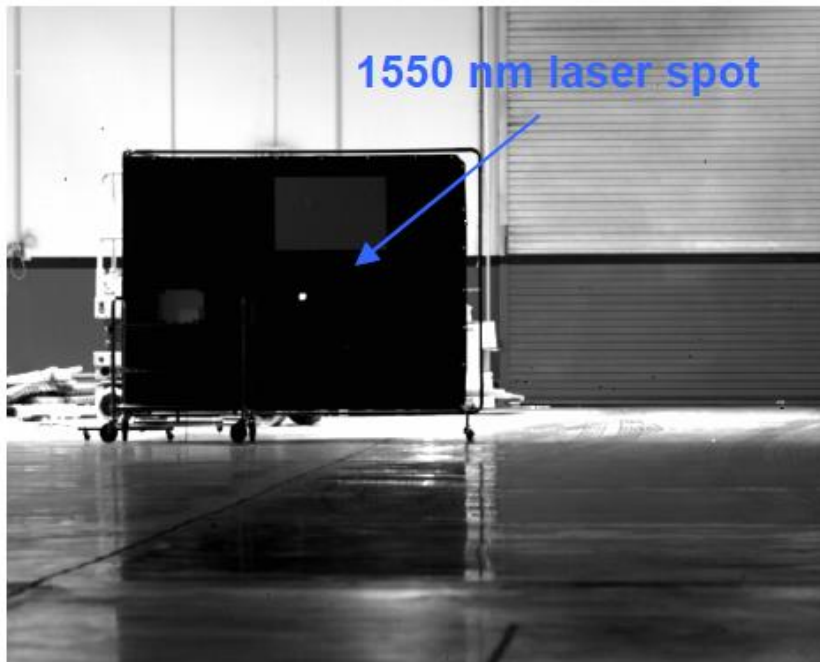


Figure 2.3: A SWIR photodetector detecting 1550 nm laser beam [15].

Night vision may be the hottest application of SWIR photodetectors. Similar to the Sunlight, the Moon and starlight radiation reflected from the objects can be detected at night. However, more importantly, night vision is realizable thanks to the radiance of the night sky which is a passive illumination source for NIR/SWIR band. Night sky radiance is called as nightglow or airglow which was discovered by Swedish physicist Anders Ångström in 1868 and it is the reason why the sky will be not absolutely dark even if Moonlight and starlight are removed [16]. Recombination of photo ionized particles by the sun, luminescence from cosmic rays striking the upper atmosphere, and chemiluminescence of oxygen and nitrogen reaction with hydroxyl ions are the three main effects constituting nightglow [16].

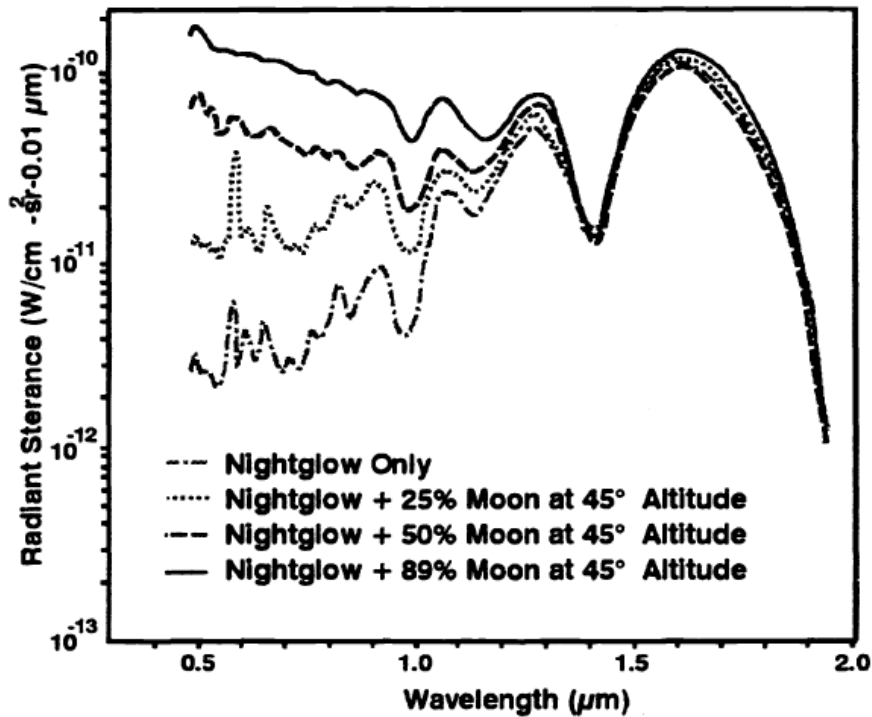


Figure 2.4: Night sky radiance spectrum under different Moonlight levels [17].

Its spectrum which can be seen from Figure 2.4 was first reported in 1972 where we can observe nightglow in terms of $W/cm^2\text{-sr}\cdot 0.1\mu m$ for visible and NIR/SWIR band of spectrum and comparison of it under different Moonlight levels [17]. Figure 2.4 reveals that nightglow is a significant illumination source between 1.2 and 1.8 μm wavelengths of SWIR band in which it achieves maximum intensity. At almost full moonlight levels, nightglow is not considerably affected beyond 1.2 μm which shows us that nightglow intensity can be sufficient for night vision (in surveillance and other military applications) particularly in SWIR band if low dark current and highly sensitive photodetectors can be produced.

In addition, SWIR photodetectors have some distinctive advantages. First, they do not need cryogenic cooling to decrease the dark current because high bandgap materials are utilized for SWIR detection, and thermally generated carriers or n_i are already reduced. Only a simple thermoelectric cooler (TEC) is sufficient to stabilize the detector temperature at near room temperatures while taking images or obtaining any kind of data

from the detector. Second, imaging quality of the photodetectors is limited by diffraction phenomenon which is a result of wave nature of the light. According to Rayleigh resolution criteria, minimum distance between pixels for clear recognition which limits the pixel pitch and resolution is defined as:

$$Pitch \geq 1.22\lambda F/\#. \quad (2.1)$$

Equation 2.1 tells us that pixel pitch is limited by wavelength and F-number of the optics used in the system. In SWIR band, shorter wavelengths basically allow to utilize optics lenses having larger F-number in the imaging which can be achieved by smaller lens diameters. Combining smaller dimension optics with eliminating cryogenic cooling, we can say that SWIR photodetectors provide advantage in terms of compactness (reduced overall system dimensions and weight) and cost compared to MWIR or LWIR counterparts.

2.2. Utilized Materials in SWIR Detection and p-i-n Diode Concept

2.2.1. Semiconductors of SWIR Band

Various materials can be used for detection in SWIR band, but Ge, InGaAs and HgCdTe are the most popular ones among those materials. Germanium's fixed and indirect bandgap restricts the flexibility of the designer, and it cannot compete with InGaAs or HgCdTe. However, developments in growth of Ge on Si substrates offer good performances ($\sim\mu\text{A}/\text{cm}^2$ dark current densities) in Ge photodetectors recently even though there is a lattice mismatch and provide the fabrication of CMOS technology based Si ROICs together on the same wafer (monolithic integration) which reduces the integration cost a lot [18], [19]. Hence, Ge photodetectors mostly utilized in photonics applications in order to fabricate waveguides, modulator or attenuator together with Ge photodetectors on the same Si substrate.

HgCdTe and InGaAs are both variable bandgap materials, and they have the advantage of tuning cutoff wavelength to desired value by changing Cd and In mole fractions

respectively. Changing Cd mole fraction does not considerably change lattice constant of HgCdTe and cutoff wavelength can be arranged to benefit from nightglow as much as possible by also considering dark current of the detectors. Although $\text{In}_x\text{Ga}_{1-x}\text{As}$ bandgap can be adjusted to cover all SWIR spectrum, it is lattice matched to InP substrate only for $x=0.53$ mole fraction and the corresponding bandgap and cutoff wavelength are known to be 0.74 eV and 1.68 μm respectively at 300 K. According to Figure 2.5, this cutoff wavelength matches with the highest nightglow radiation, but to detect nightglow for longer wavelengths (lower bandgap energy is required), In mole fraction should be increased (InAs bandgap= 0.354 eV and GaAs bandgap= 1.424 eV) which changes the lattice constant and breaks lattice matched condition with InP [20]. Therefore, InGaAs can benefit from nightglow radiation more at the expense of dislocations in grown material which generates additional trap states in bandgap and increases G-R current. The region having cutoff wavelength beyond 1.7 μm may be called as extended SWIR where both reflective and emissive radiation can be detected, and InGaAs photodetectors lose performance due to increased n_i and defect levels. On the other hand, covering radiation in wider range is the advantage of HgCdTe over InGaAs. However, CdZnTe substrates lattice matched to HgCdTe material possess high cost and wafer dimensions are small compared to InP substrates. For applications where 1.68 μm cutoff wavelength is sufficient, $\text{In}_{0.53}\text{Ga}_{0.47}\text{As}$ provides optimum detector performance in terms of very low dark current, high responsivity and QE in large format FPAs, and with much lower cost. Researchers are trying to grow HgCdTe on Si or GaAs substrates to overcome high cost and even if lattice mismatch exists in the epilayer, SWIR HgCdTe photodetectors have been recently demonstrated [21].

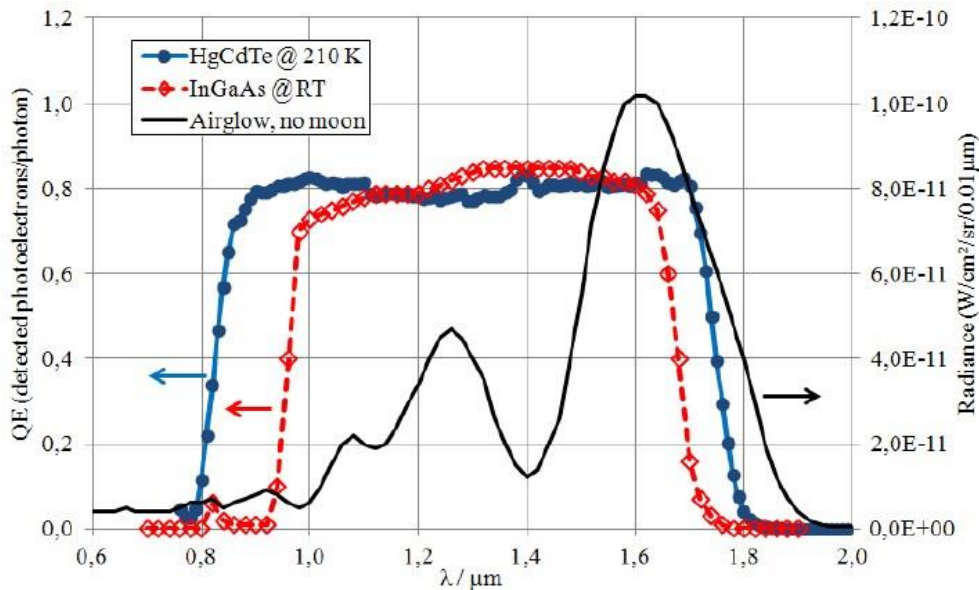


Figure 2.5: Typical QE spectrum of InGaAs and HgCdTe detectors depicted on the same graph with airglow spectrum under no Moonlight [20].

2.2.2. p-i-n Type Photodiodes

p-i-n photodiodes are special types of p-n junctions or photovoltaic detectors where an intrinsic absorber layer is placed between p and n doped regions. The low carrier concentration in intrinsic layer results in low conductivity and high resistivity across the region. Then, high voltage drop occurs along the layer under small reverse bias voltages which means that the absorber becomes depleted and very high electric field exists. This situation provides easy collection of photo-generated carriers under very small reverse bias voltages and it is the advantage of p-i-n type diodes. Figure 2.6 represents both p-i-n diode structure with corresponding band diagram and the photo-generation and collection process of the carriers [5].

The design parameters of p-i-n diodes are now discussed. First, the thickness of the absorber should be carefully selected so that it can effectively absorb the radiation which displays exponentially decreasing behavior with the distance according to Beer-Lambert law. Otherwise, photo-response of the detector is degraded.

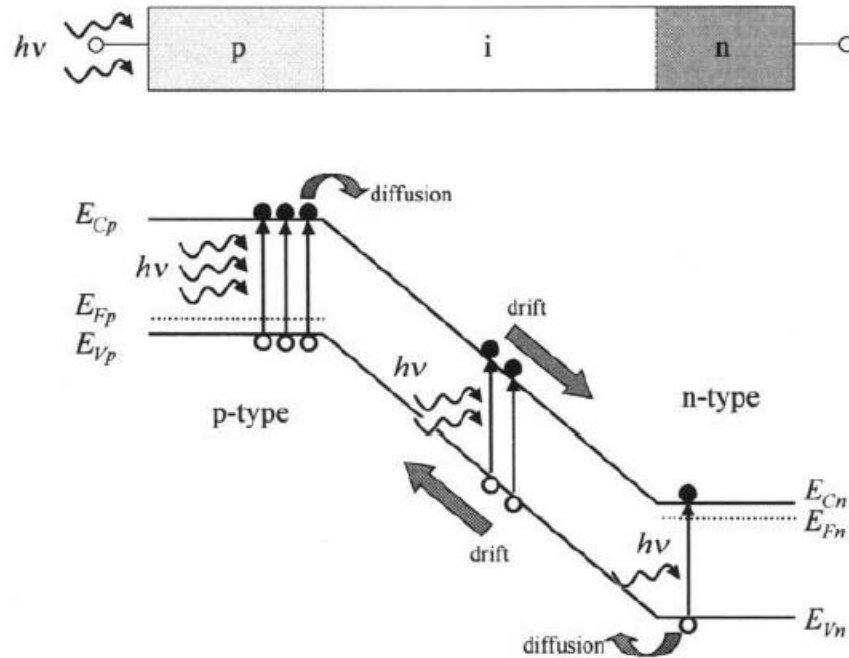


Figure 2.6: p-i-n diode structure and corresponding energy band diagram showing also photo-generation process [5].

Furthermore, the absorber may be intentionally doped to engineer the bandgap for different materials systems utilized in p-i-n diodes. In this case, it should be kept in mind that, the absorber should not be heavily doped. Otherwise, the carrier lifetimes and diffusion lengths deteriorate. In addition, as usual in all photodetectors, the contact p and n regions must have high doping concentrations in order to reduce contact resistance during metallization.

The epitaxial structure of conventional p-i-n diodes are presented in Figure 2.7 [5]. p^+ and n^+ stand for heavily doped p and n contact regions. These diodes can be fabricated to be used under front or back illumination. In the front illumination, radiation reaches directly to grown layers on substrate. Ge detectors belong to this category due to monolithic integration with ROICs. Radiation falls onto the detector from the substrate side in the back illumination case. This type involves InGaAs and HgCdTe photodetectors which are coupled to ROICs via flip-bonding technique where pixels of

FPA and ROIC come to face to face position for connection, and we observe the photodetector from its backside.

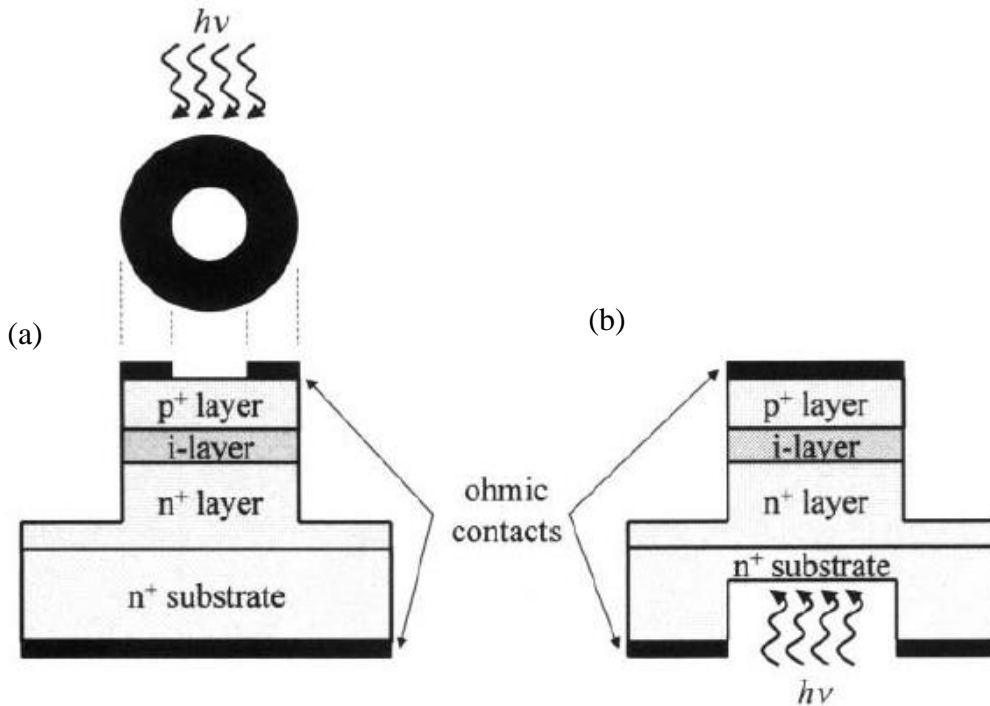


Figure 2.7: Epilayer structure of p-i-n photodiodes designed for (a) front and (b) back illumination [5].

2.3. NIR/SWIR HgCdTe Photodetectors

HgCdTe is the leading material in photodetector market since it can cover 1-20 μm wavelengths of infrared spectrum with its variable bandgap and very small change in lattice constant occurs while changing Cd mole fraction. The variation in bandgap, cutoff wavelength and lattice constant with respect to Cd mole fraction is provided in Figure 2.8 [22]. Combining wide range spectrum coverage and ability for multicolor detection with excellent electrical and optical bulk properties renders HgCdTe as the most promising candidate to develop infrared photodetector technology.

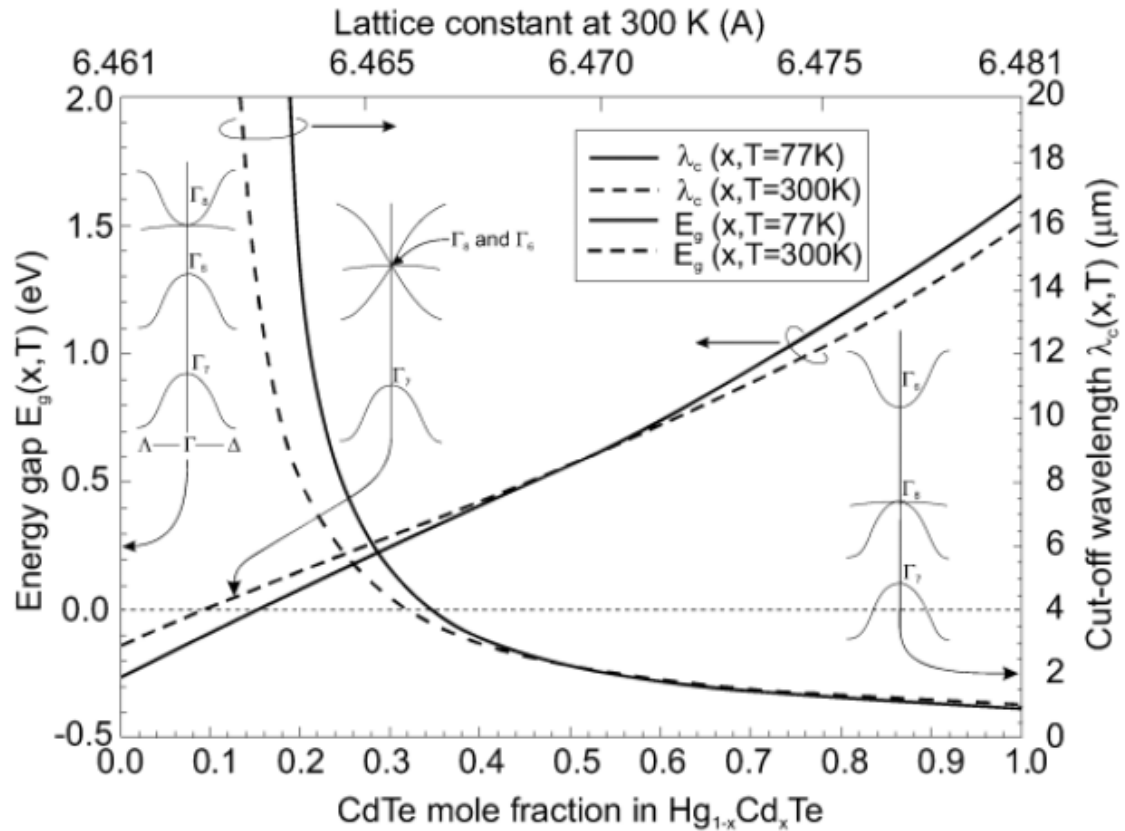


Figure 2.8: HgCdTe bandgap energy (straight line), cutoff wavelength (parabolic line) and lattice constant variation with the change of Cd mole fraction [22].

Apart from these advantages, including toxic materials such as Hg and weak Hg-Te bonds which leads to surface instability can be counted as some disadvantages of HgCdTe material that actually can be handled. Major disadvantage is that CdZnTe substrates lattice matched to HgCdTe material costs a lot and wafer dimensions are small. In order to reduce substrate cost, HgCdTe is tried to be grown on alternative substrates such as Si or GaAs, but in that case, lattice matched condition is distorted. Now, status of state-of-the-art SWIR HgCdTe photodetector technology will be analyzed.

AIM Infrarot-Module GmbH of Germany is one of the primary companies developing SWIR HgCdTe photodetectors and important results have been published starting from 2014 [20]. They are growing the designs on in-house produced CdZnTe substrates by Liquid Phase Epitaxy (LPE). Pixels are being processed in planar type with n-on-p polarity meaning that after growing p type HgCdTe layer pixels are formed with n type diffusion process. CdTe was utilized as passivation layer in their designs. By improving fabrication techniques, in the first results, diffusion limited performance and 2 nA/cm^2 dark current densities at 240 K were obtained from $15 \text{ }\mu\text{m}$ pitch detectors having response in $0.85\text{-}1.75 \text{ }\mu\text{m}$ range [20]. As can be seen from Figure 2.5, around 80% QE was achieved after depositing 3 layers of antireflection coating. 640×512 FPAs were coupled to in-house designed $15 \text{ }\mu\text{m}$ pitch ROICs based on $0.18 \text{ }\mu\text{m}$ CMOS technology and capacitive transimpedance amplifier (CTIA) utilization at the input stage. At the second stage of the design, cutoff wavelength was extended to $2.5 \text{ }\mu\text{m}$ by changing Cd mole fraction and $15 \text{ }\mu\text{m}$ pitch, 640×512 FPAs were produced [21]. At 200 K, 50 nA/cm^2 dark current densities were obtained from this photodetector. In the latest demonstrated detectors, $10 \text{ }\mu\text{m}$ pitch detectors and an optimized ROIC for extended SWIR detection have been realized [23]. Furthermore, the first results of HgCdTe detector having $2.6 \text{ }\mu\text{m}$ cutoff and grown on GaAs substrate with MBE have been provided. Compared to $2.5 \text{ }\mu\text{m}$ cutoff HgCdTe grown on CdZnTe, one order of magnitude higher dark current densities have been reported at 175 K. Dark current densities measured for each developed photodetector technology, SWIR ($1.8 \text{ }\mu\text{m}$) and extended SWIR ($2.5 \text{ }\mu\text{m}$) images taken by $15 \text{ }\mu\text{m}$ pitch, 640×512 FPAs in daylight, moonless night and cloudy conditions are given in Figure 2.9 (a), (b) and (c) respectively.

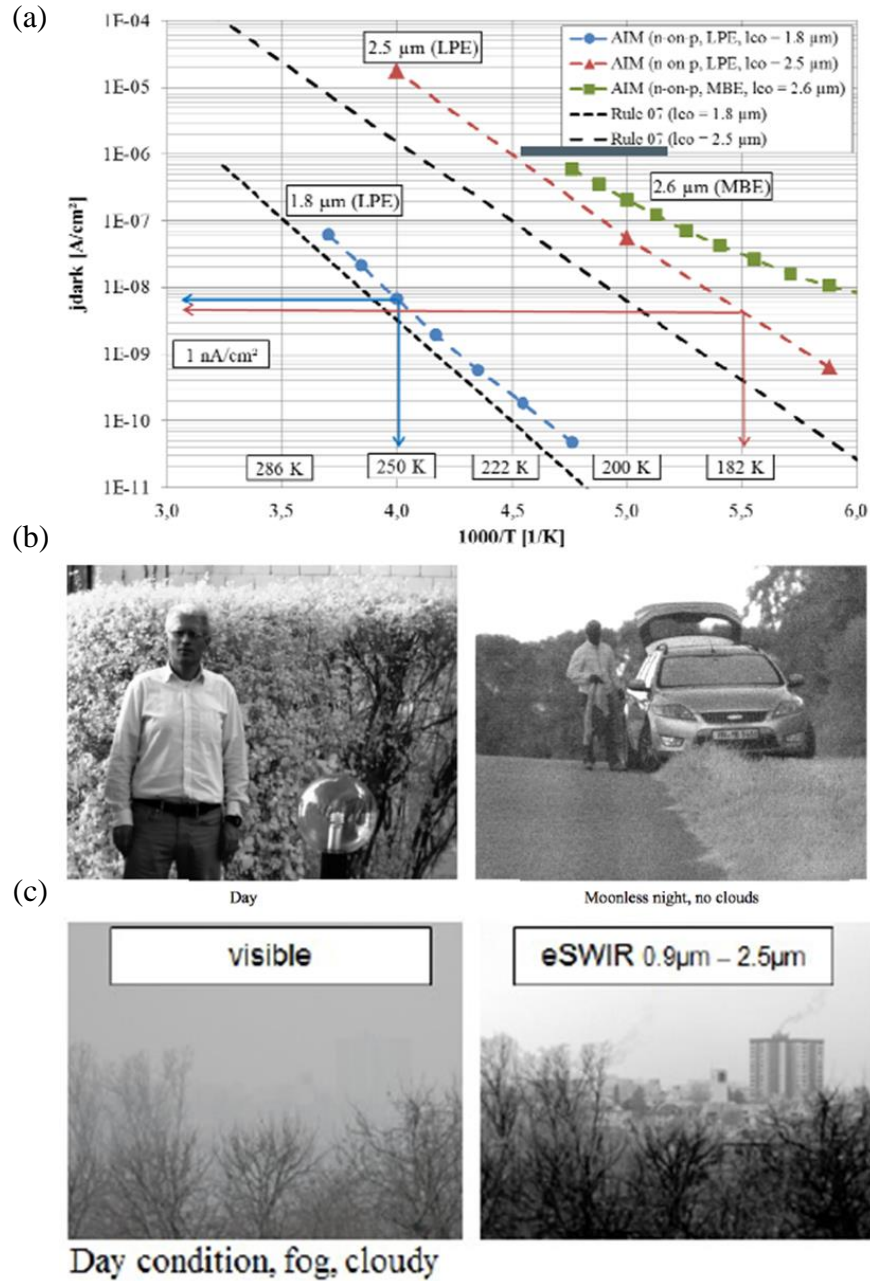


Figure 2.9: (a) I_{dark} densities reported from $15 \mu\text{m}$ pitch, 640×512 HgCdTe FPAs grown on CdZnTe substrates with LPE and GaAs substrates with MBE in AIM facilities for 1.8 , 2.5 and $2.6 \mu\text{m}$ cutoff wavelengths. (b) SWIR images captured from $1.8 \mu\text{m}$ cutoff detector under daylight and moonless night conditions. (c) Extended SWIR images captured from $2.5 \mu\text{m}$ cutoff detector under foggy and cloudy conditions [21], [23].

Sofradir of France is one of the leading companies in the world which has very wide photodetector technology and ROIC fabrication ability background. In order to develop high performance technology in NIR/SWIR space applications which requires very low dark current densities, they are working together with CEA-LETI (French Atomic Energy Commission, Electronic division), and CEA-IRFU (French Atomic Energy Commission, Astrophysics Service) in the production of HgCdTe NIR/SWIR photodetectors. To realize ultra low dark current, they started progressing planar type p-on-n HgCdTe architecture [24]. The schematic of p-on-n architecture is depicted in Figure 2.10 [25]. The architecture was grown on CdZnTe substrate with both LPE and Molecular Beam Epitaxy (MBE) techniques. Normally, HgCdTe is doped with Hg vacancies which are not convenient for p type doping aimed in this process. Therefore, first extrinsic In doped HgCdTe was grown. They reported that In doping concentration varies minority carrier lifetime, diffusion length, and accordingly, dark current by even changing dominant recombination Auger to SRH and photo-response of the detector [26]. After that, p-n junctions were created by As ion implantation and planarity was preserved. It was followed by passivation, metallization and antireflection coating deposition.

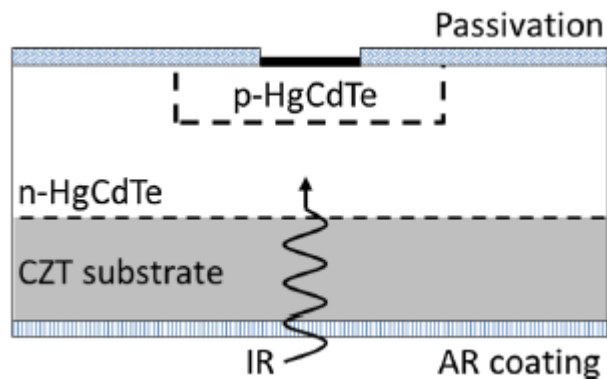


Figure 2.10: p-on-n HgCdTe architecture developed by Sofradir and CEA [25].

Utilizing p-on-n structure, 15 μm pitch FPAs from 1.96 to 2.5 μm cutoff wavelengths have been fabricated, and very low dark current values were achieved compared to n-on-p planar architecture at the final stage. Dark current evolution of these photodetectors

through the years is provided in Figure 2.11 (a) [27]. It shows that $0.1e^-/s$ dark current per pixel was obtained from FPA pixels at 100 K in the final designs with LPE. Also, around 80% QE was measured from the devices including antireflection coatings as seen from Figure 2.11 (b). As mentioned in the latest article, they are going to produce 2Kx2K format FPAs to be used in space applications.

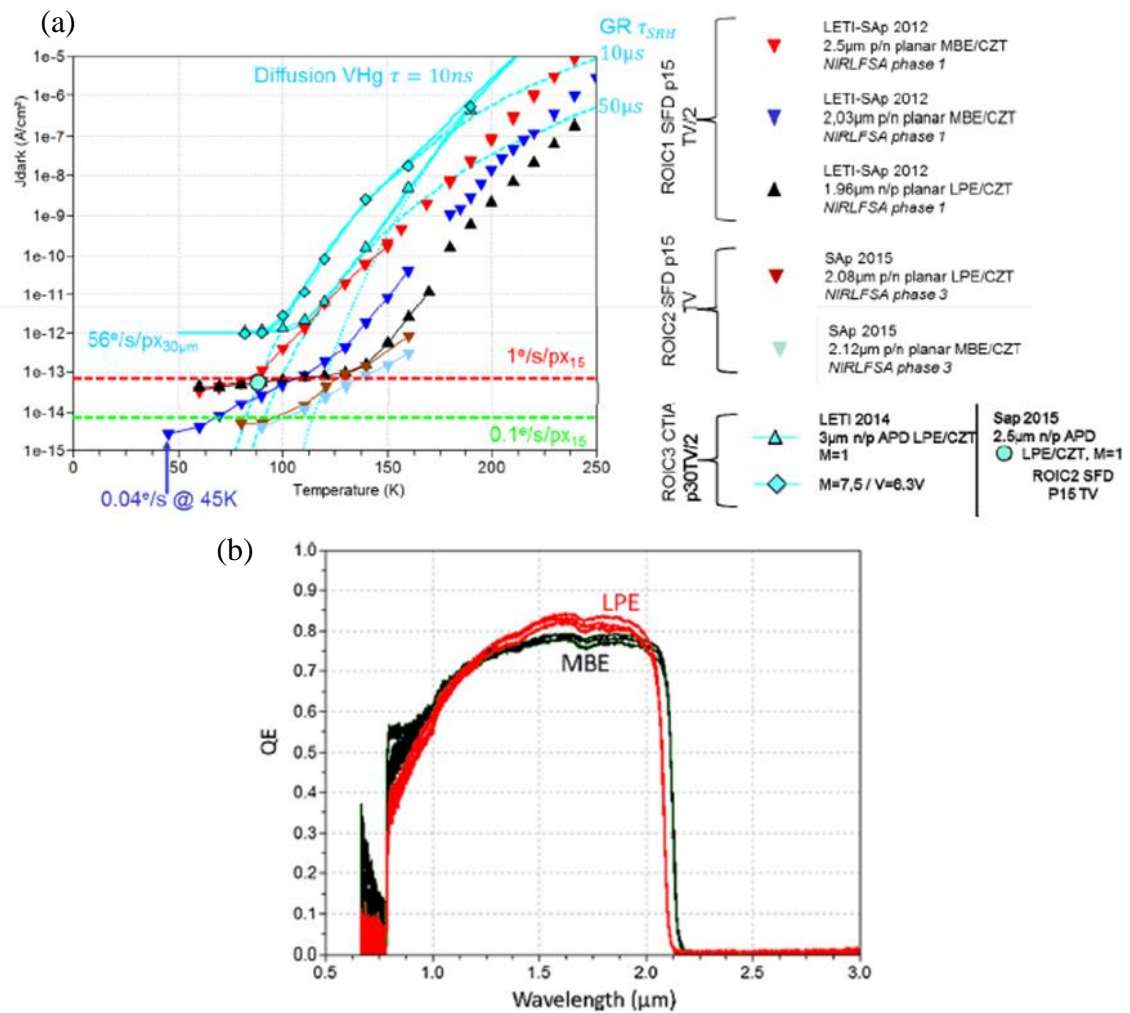


Figure 2.11: (a) Sofradir-CEA planar p-on-n architecture HgCdTe photodetectors' dark condition performance in years. (b) QE of HgCdTe detectors when antireflection coating is present [27].

2.4. NIR/SWIR InGaAs Photodetectors

InGaAs photodetectors are the most appropriate candidates for SWIR detection at a 1.7 μm cut-off wavelength with their high material quality thanks to advanced III-V material growth techniques and bulk properties. They provide very high performance in terms of sensitivity and noise. In InGaAs detectors mostly p-i-n type photodiode structures are utilized. In order to reduce the dark current, p and n sides are selected as InP material which is a higher bandgap material (1.34 eV at 300 K) and consequently has lower thermal generation rate. Therefore, InP/InGaAs heterojunction photodetectors are the most encountered and preferred ones in SWIR technology. However, when FPA and ROIC is coupled to each other by hybrid integration and photodetector can only be illuminated from backside, InP substrate absorbs radiation below 920 nm wavelength, so in order to sense the radiation at NIR and visible range in InGaAs photodetectors, InP substrate should be removed. The substrate thinning is generally achieved by mechanical grinding, then for the complete removal, wet etching can be applied.

The properties of $\text{In}_{0.53}\text{Ga}_{0.47}\text{As}$ and InP materials at 300 K is presented in Table 2.1.

Table 2.1: Lattice matched InGaAs and InP material properties at 300 K.

T=300 °K	$\text{In}_{0.53}\text{Ga}_{0.47}\text{As}$	InP
Crystal Structure	Zinc Blende	Zinc Blende
Lattice Constant	5.869 Å	5.869 Å
Energy Bandgap	0.74 eV	1.34 eV
Electron Affinity	4.5 eV	4.38 eV

In case of deviations in mole fraction and temperature, bandgap of InGaAs material is calculated as:

$$E_{g(x,T)} = 0.42 + 0.625x - \left[\frac{5.8}{T+300} - \frac{4.19}{T+271} \right] * 10^{-4}T^2x - \frac{4.19*10^{-4}T^2}{T+271} - 0.475x^2 \quad (2.2)$$

where x corresponds to Ga mole fraction, unit of E_g is in eV and unit of T is in K [28]. For $\text{In}_{0.53}\text{Ga}_{0.47}\text{As}$ material, bandgap variation with respect to temperature is given in Figure 2.12.

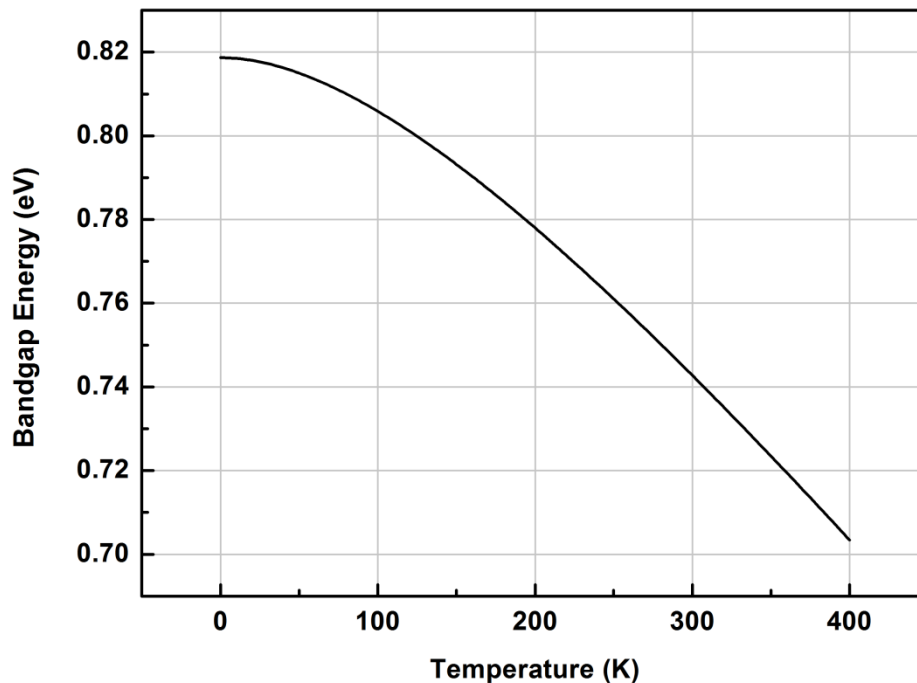


Figure 2.12: $\text{In}_{0.53}\text{Ga}_{0.47}\text{As}$ material's bandgap change with respect to temperature.

2.4.1. Mesa and Planar Process in InGaAs Photodetectors

Mesa and planar processing techniques are available for the fabrication of InGaAs photodetector. In mesa technique, pixels are formed by dry or wet etching methods and pixels become fully isolated from each other. However, sharp sidewalls of the pixels are also created during the etching. These sidewalls constitute additional path for current flow at the surroundings of the pixels by introducing new trap states. Existence of new trap states can be related to the charge accumulation coming from residual byproducts during chemical etch or dangling bonds as the missing atoms can be occurred at the surface. This current is called as surface leakage current and it depends on the perimeter of the pixels. It can be reduced to below certain values with the proper passivation of the

surface by the dielectric materials, but obtaining perfect passivation of the surface is a very hard work since it requires perfect suitable dielectric material. Therefore, mesa type InGaAs photodetectors show surface leakage limited performance with decreasing pixels sizes to 25 and 15 μm and reduction in bulk related currents. In planar process, on the other hand, pixels are formed after epitaxial growth by p type diffusion process. This means that during the growth, p type doping is not done and pixels become buried in the epilayer as p-i-n diode will only be constructed where p diffusion is applied. By this way, formation of sidewalls is eliminated and surface leakage current is decreased significantly. A typical structure of planar InGaAs photodetector is presented in Figure 2.13 [29]. State-of-the-art InGaAs photodetectors are mostly fabricated with planar process and low dark current is achieved. As a p type doping material Zinc (Zn) metal is preferred in the fabrication. However, planar InGaAs detectors may suffer from crosstalk since the pixels are not isolated from each other. Due to complete isolation in mesa process, crosstalk is not a problem which makes them suitable for easy detection of different wavelengths as in hyperspectral imaging or for multiple band applications.

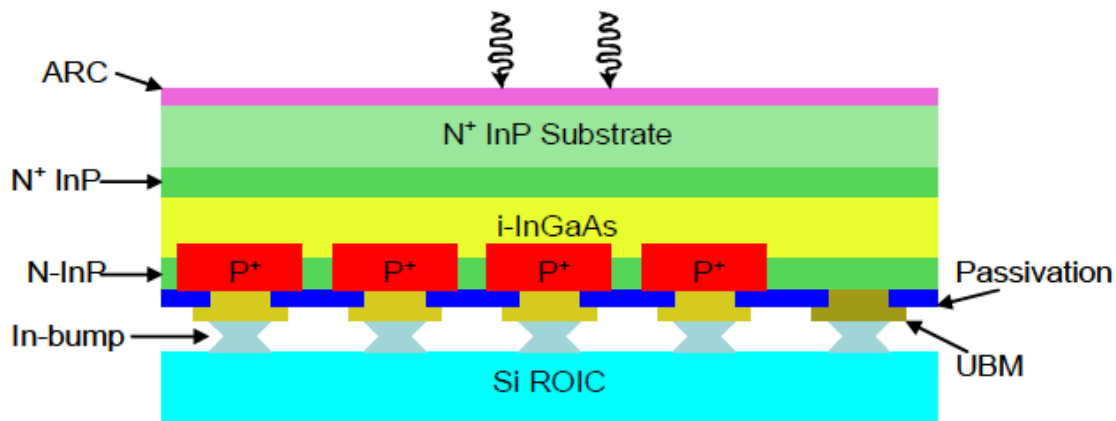


Figure 2.13: Planar type InGaAs photodetectors' typical structure [29].

2.4.2. Planar Type State-of-the-art InGaAs Photodetectors

One of the low dark current levels achieved in planar InGaAs photodetectors was demonstrated in 2007 by Goodrich Corporation [30]. They made use of the epitaxial structure given in Figure 2.13. The design was grown with Metalorganic Chemical Vapor Deposition (MOCVD) technique. They fabricated 20 μm pitch 640x512 NIR/SWIR FPAs with 1.7 μm cutoff wavelength, and 30.8 fA mean dark current was measured at 25 $^{\circ}\text{C}$. At 12.3 $^{\circ}\text{C}$, 2 nA/cm² dark current density was achieved at -0.1 V bias voltage which displayed diffusion limited behavior. InP substrate was removed successfully and approximately 90% QE was achieved. FPAs were also coupled to in-house fabricated ROICs having less than 10 e⁻ noise. The mentioned results are provided in Figure 2.14.

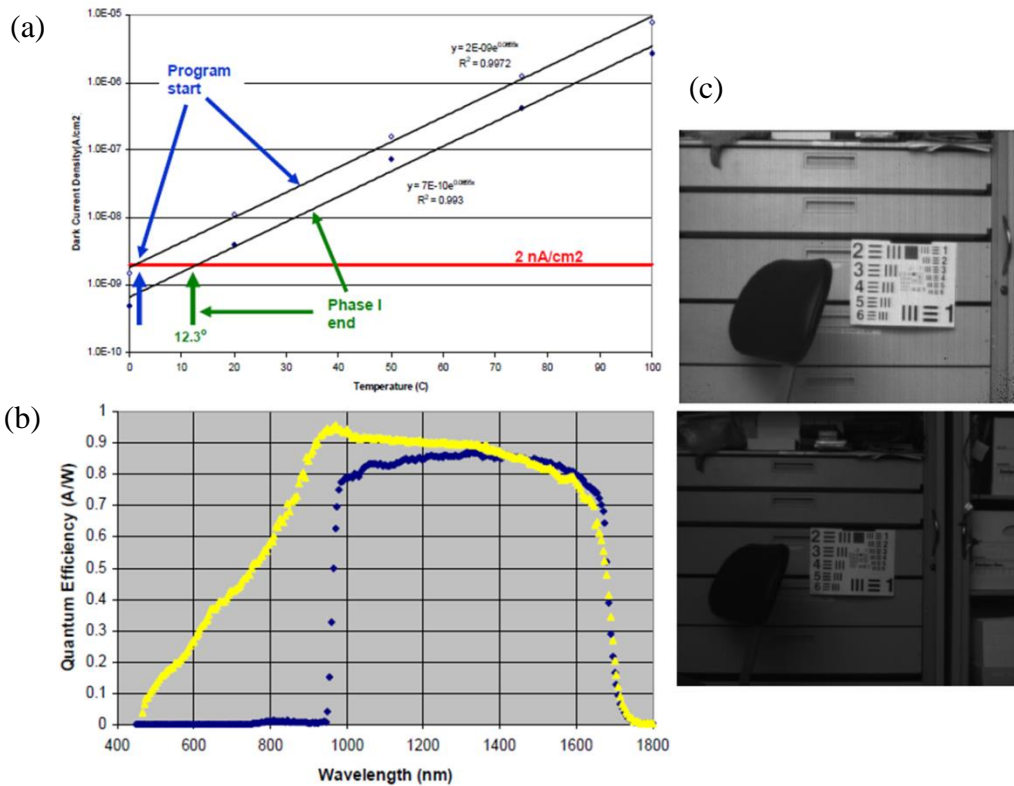


Figure 2.14: (a) Dark current density of 20 μm pitch 640x512 NIR/SWIR InGaAs camera developed by Goodrich SUI. (b) QE of the fabricated photodetectors. (c) Images taken by 640SDX product under Tungsten lamp illumination and low light level [30].

Sofradir is also producing commercial products of InGaAs photodetectors particularly after the transfer of existing technology in Thales III-VLab to the organization. Almost every year, they are presenting their current status with developed cameras and ROICs which are especially produced for low photon flux detection in SWIR. Sofradir's InGaAs photodetectors are based on planar type p-i-n diodes. In 2015, Sofradir introduced 640x512 format 15 μm pitch so called SNAKE product grown with Metal Organic Vapor Phase Epitaxy (MOVPE) [31]. This product is basically the extension and optimization of the work conducted at 2013 [32]. In the fabrication, p type doping was executed by Zn diffusion process where SiN was used as a masking layer which was followed by surface passivation with SiN. Then, FPA was coupled to a ROIC via flip-bonding including reflow process of In bumps. They reported surface leakage limited and perimeter dependent dark current which was measured as 11 fA and 7 fA for 6 μm and 4 μm diameters respectively at -0.2 V as seen in Figure 2.15 (a). Detectors were also coated with SiO₂/TiO₂ materials to minimize reflection and increase QE. For the detection in visible range, InP substrate was removed to around hundred nanometers by only wet etching. QE of SNAKE product can be observed from Figure 2.15 (b) where more than 70% and 80% QE was reported under substrate not removed and removed conditions respectively. Scanning Electron Microscopy (SEM) image of the coupled sample is also provided in Figure 2.15 (c) and more than 99.99% yield was achieved during hybridization. Images taken by SNAKE are given in Figure 2.15 (d) where 99.97% operability and 2.78% nonuniformity in response was recorded.

Based on SNAKE product, Sofradir improved the characteristics of ROIC especially from noise point of view and introduced their 640x512 format 15 μm pitch C-RED 2 camera in 2017 [33]. Since SNAKE has very low dark current, during the imaging readout noise was dominating the detector performance, so low noise ROIC based on CTIA utilization at the input stage was produced. In C-RED 2, the readout noise was reported as only 10 e⁻ at 25 FPS and 22 e⁻ at 400 FPS full frame. They measured the mean dark current of the camera as 290 e⁻/s or 0.05 fA at -40 °C by thermoelectric

cooling. C-RED 2 is currently operating only at SWIR band with more than 70% QE. Readout noise and the final product can be observed from Figure 2.16.

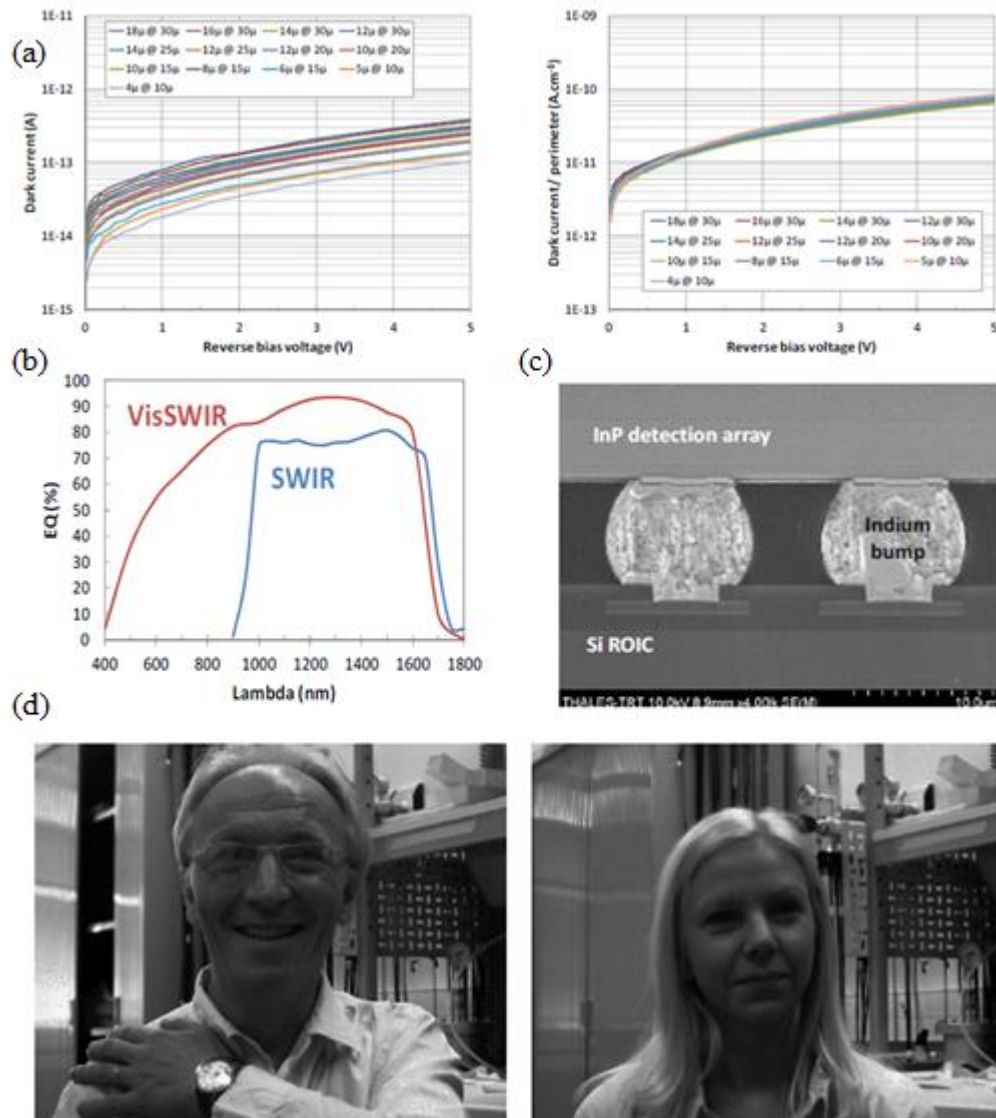


Figure 2.15: (a) Dark current analysis of detector pixels having different diameter and showing perimeter dependency in Sofradir SNAKE camera. (b) QE of SWIR and visible InGaAs cameras. (c) SEM image of flip-chip bonding process. (d) Snapshots of SNAKE camera [31], [32].

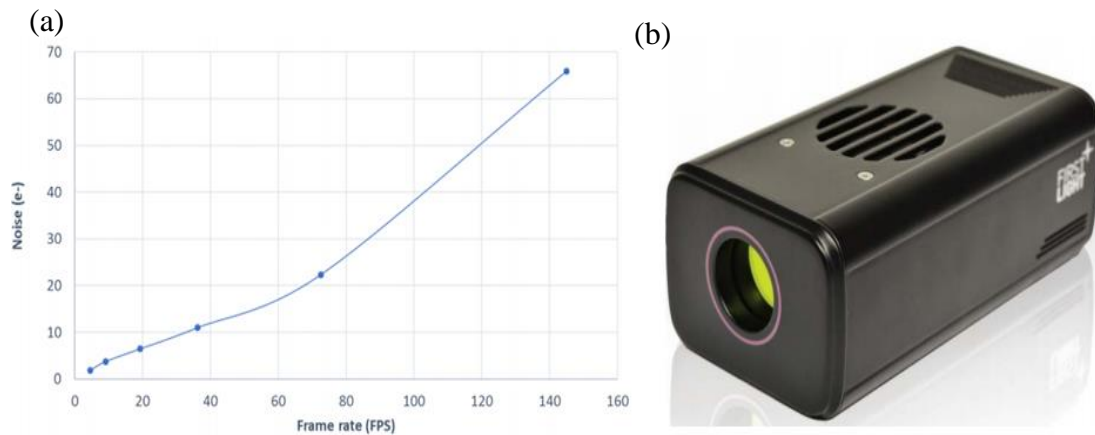


Figure 2.16: (a) Readout noise of C-RED 2 product with respect to frame rate and 22 e⁻ noise was achieved at 400 FPS which is not shown in the graph. (b) Commercial C-RED 2 product [33].

FLIR Systems is another leading company producing infrared devices. In 2012, they presented high performance 15 μm pitch SWIR InGaAs FPAs in 640x215 and 1920x1080 format [15]. They also developed their own ROICs for each format. The mean dark current density measured from the FPAs was indicated as 1.5 nA/cm² at 7 °C and 0.26 nA/cm² at 0 °C which means ultra-low level of noise. Dark current taken at different temperatures are illustrated in Figure 2.17 (a). They calculated the corresponding readout noise for various pixel pitches and dark current densities as shown in Figure 2.17 (b). 120 e⁻ and 50 e⁻ noise was reported for 640x512 and 1920x1080 format ROICs at 30 Hz frame rate. Therefore, FPA performances are limited by readout noise at this stage. A wide field image observed with 1920x1080 FPA is provided in Figure 2.17 (c) which has high quality and contrast.

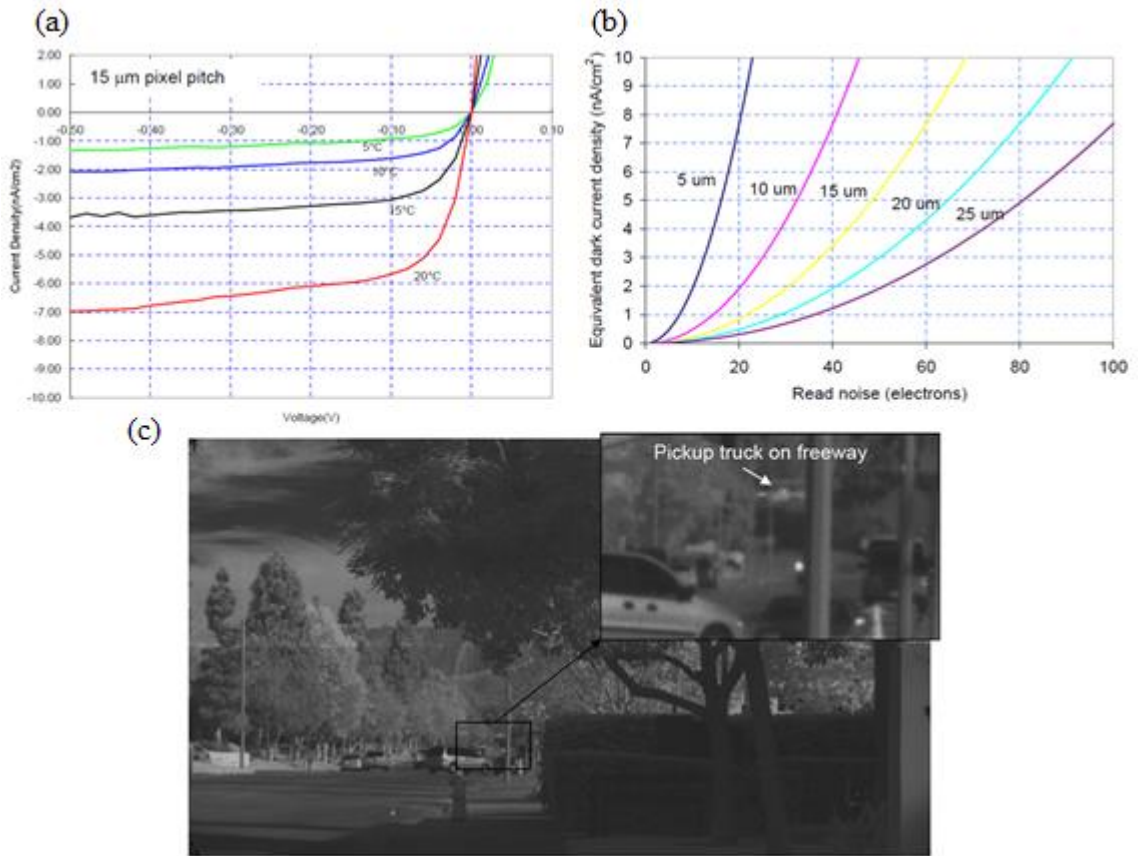


Figure 2.17: (a) Dark current density of 15 μm pitch FLIR camera at different temperatures. (b) Equivalent readout noise in terms of electrons of pixel's dark current density for various pixel pitches. (c) 1920x1080 image captured by FLIR camera [15].

2.4.3. Mesa Type State-of-the-art InGaAs Photodetectors

1.7 μm cutoff state-of-the-art InGaAs photodetectors are usually fabricated by planar type process to lower surface leakage current. Mesa type photodetectors mostly includes utilization of new design structures or extended SWIR detection.

A unique design to improve mesa processed 1.7 μm cutoff InGaAs p-i-n photodetectors was proposed by making use of conduction band barrier concept which prevents the flow of majority carriers (electrons in this configuration) and eliminates surface leakage current [34]. The design's epitaxial structure is given in Figure 2.18 (a). Conduction

band barrier was obtained by inserting undoped InAlAs material between InGaAs absorber and p contact layers where lattice matched condition also does not get distorted. However, in addition to conduction band barrier, InAlAs forms a valence band offset in energy band diagram, and in that case, photo-generated hole cannot be collected which decreases responsivity of the detector. In order to solve this problem, InAlGaAs grade layer was placed between absorber and barrier layers where material composition was changed to sweep bandgap from InGaAs to InAlAs materials' bandgap. Then, 5 nm thick delta doped sheets were inserted which creates a static electric field in the opposite direction of electric field generated by valence band offset variation in the first place. With this way of bandgap engineering, valence band offset was eliminated and conduction band barrier placement was accomplished. Fabricated 10 μm pitch detectors without applying any passivation procedure provided 44 fA at -0.1 V and room temperature which can be seen from Figure 2.18 (b). Also, the results were compared to conventional mesa detectors, and there observed more than 100 factor difference between them which is an outstanding result for mesa type detectors. Barrier detector was found to be still surface leakage limited when perimeter-to-area ratio increased which shows the requirement of further optimization of the proposed design. At last, 10 nA/cm² dark current density was measured from 25x25 μm^2 detectors and 0.62 A/W responsivity was recorded at 1550 nm.

A high performance MBE grown extended SWIR (2.65 μm cutoff) InGaAs photodetector including a novel approach in epitaxial structure has also been recently proposed and characterized in FPA level by Quantum Devices and Nanophotonics Laboratory in Middle East Technical University [35]. Photodetector utilized p-i-n diode structure where unintentionally doped absorber layer was made from In_{0.83}Ga_{0.17}As material. In order to reduce lattice mismatch effect between InP substrate and absorber layer InAlAs graded layer was inserted into design. 25 μm pitch 640x512 FPA having 20x20 μm^2 mesa sizes has been fabricated by wet etching. At 180 K and 25 mV reverse bias voltage, 0.48 $\mu\text{A}/\text{cm}^2$ dark current density levels were measured.

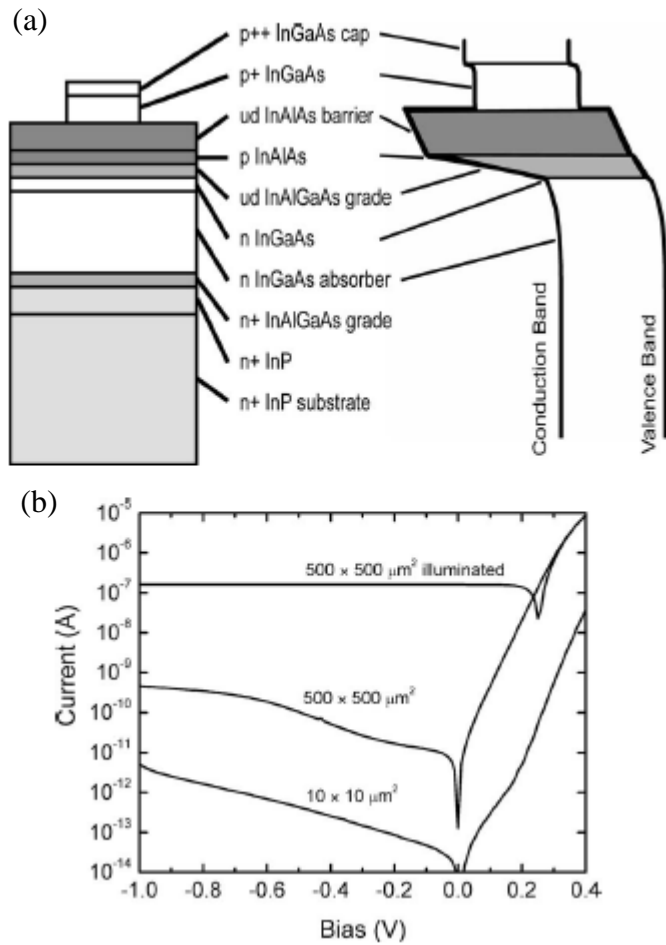


Figure 2.18: (a) Proposed InGaAs p-i-n diode structure including InAlAs barrier. (b) Dark current levels obtained from different mesa sizes [34].

At 300 K, main dark current mechanism was determined as G-R current as expected due to high lattice mismatch. As the temperature decreases to 200 K, shunt leakage current become the major dark current component up to -3 V since G-R current reduces and dynamic resistance is low because of lattice mismatch which is provided in Figure 2.19 (a). In terms of photo-response, as depicted in Figure 2.19 (b), ~90% peak QE was obtained around $1.7 \mu\text{m}$ wavelength, then it followed a decreasing trend due to free carrier absorption in n doped substrate and graded buffer layers. In FPA pixels, with a record level of 99.8% pixel operability was achieved with hybrid integration and high quality images were captured with only one point nonuniformity correction as observed from Figure 2.19 (c).

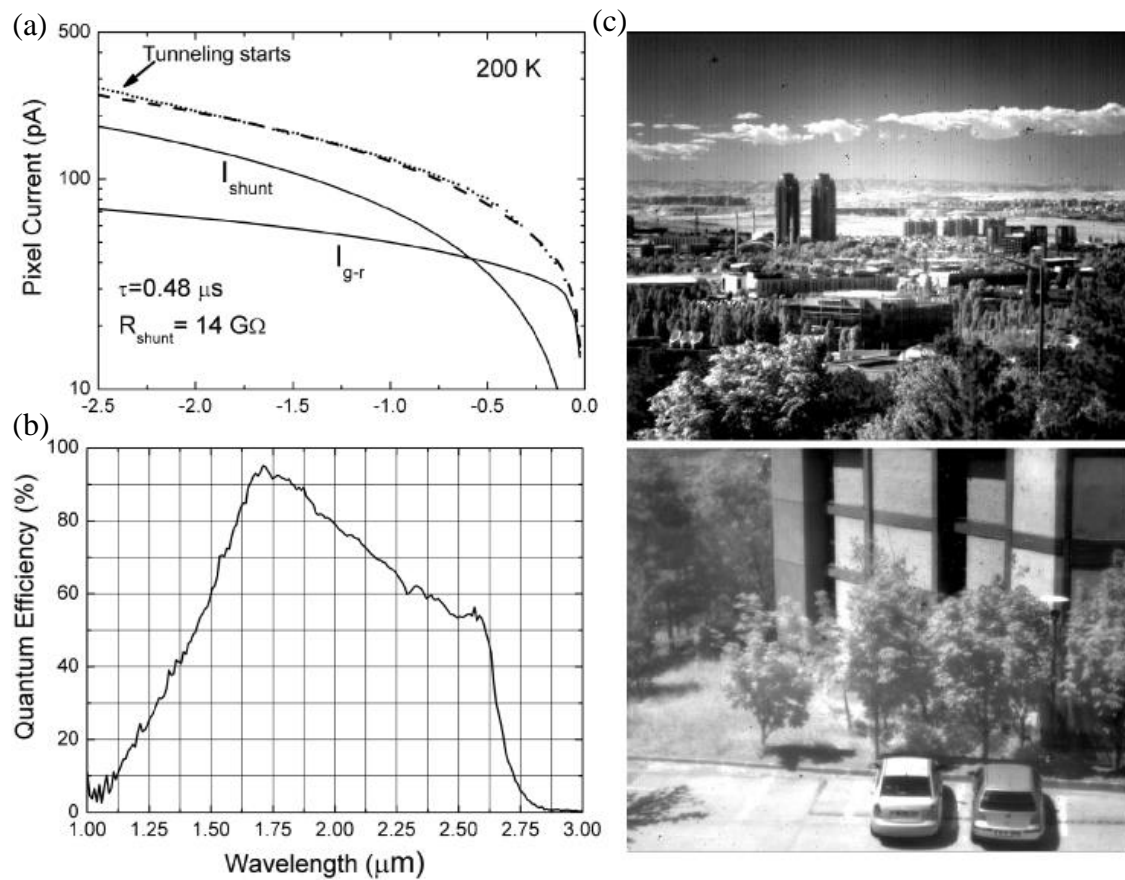


Figure 2.19: (a) Dark current of $\text{In}_{0.83}\text{Ga}_{0.17}\text{As}$ photodetector having InAlAs grading layer. (b) QE of the proposed detector. (c) Images captured by extended SWIR InGaAs photodetector [35].

CHAPTER 3

PLANAR AND MESA TYPE MEGAPIXEL AND LARGE FORMAT SWIR InGaAs FPA FABRICATION DEVELOPMENT

In this chapter, fabrication development procedure of 25 and 15 μm pitch SWIR InGaAs photodetectors will be discussed from material growth with Molecular Beam Epitaxy (MBE) to hybrid integration. Dark current, responsivity, and FPA level characterization results will be presented.

3.1. MBE Growth of InGaAs Photodetectors and Wafer Characterization

The growth progress and the growth of the final epilayer design were carried out with III-V Riber Epinat MBE reactor located at METU Quantum Devices and Nanophotonics Laboratory. Some of the development in InGaAs and InP material growths were also a part of a previous M.Sc. thesis work [36]. In order to optimize the growth procedure, various fine tunings were applied to flux calibration and substrate temperature adjustment steps. Also, the thickness and the doping concentration of the layers in the design were selected after iterative growths to suppress dark current and enhance responsivity of the photodetectors. The final epilayer structures utilized in this work are given in Figure 3.1 for planar and mesa type processing techniques.

(a)

$i\text{-In}_{0.53}\text{Ga}_{0.47}\text{As}$
$i\text{-InP}$
$i\text{-In}_{0.53}\text{Ga}_{0.47}\text{As}$ (Absorber)
$n\text{-InP}$
$\text{In}_{0.53}\text{Ga}_{0.47}\text{As}$ Etch Stop
InP Substrate

(b)

$p\text{-In}_{0.53}\text{Ga}_{0.47}\text{As}$
$p\text{-InP}$
$i\text{-In}_{0.53}\text{Ga}_{0.47}\text{As}$ (Absorber)
$n\text{-InP}$
$\text{In}_{0.53}\text{Ga}_{0.47}\text{As}$ Etch Stop
InP Substrate

Figure 3.1: (a) Epilayer structure utilized in planar type InGaAs photodetectors. (b) Epilayer structure utilized in mesa type InGaAs photodetectors.

3.1.1. MBE System Basics

MBE is one of the most important growth techniques to achieve high crystal quality while providing excessive control over the growth parameters. In these systems, growth chamber is kept at ultra high vacuum (UHV) in order to reduce collision rates of material atoms with the atoms in the air. Due to UHV environment, mean free path of the particles are increased which basically slows down the growth procedure, but gives the opportunity to control the particle motions precisely. Hence, MBE systems enable to grow high quality crystal at the expense of lower growth rates and cost.

METU Riber Epinat MBE system utilized in this work contains III-V materials in the effusion cells. In and Ga are Group III and P and As are Group V elements loaded to the cells. Also, Si (Group IV) and Beryllium (Be) (Group II) elements are available for n and p type doping of Group III materials respectively. Speaking of the effusion cells, there are two types of cells present in the system. Group V materials are located in valved cracker cells to control their allotropes. These materials are evaporated in

tetramer forms such as P_4 or As_4 , and they may be required to be used in P_2 and As_2 dimer forms. There is an additional condenser compartment in P cell in order restrict the production of white P which can cause harm to people since it gets burned with the interaction of atmosphere. Therefore, only needed amount of P is generated and stored in condenser which has lower temperature than other parts of the cell. The flux rate in valved cracker cells is managed by the valve openings. The materials except of P and As are located in double filament effusion cells where the material flux is controlled by the base and tip temperature of the crucible with the help of thermocouples and powering cables.

The growth chamber pressure is kept at UHV by a cryo pump, an ion pump and a titanium sublimation pump. The pressure is further decreased during growth by supplying liquid nitrogen (LN_2) to the cryo panels of the chamber. Substrate or wafer holder is attached to growth chamber which can rotate and heat up the sample for uniform and defect free growth. There are also some measurement and inspection tools in the chamber. Beam equivalent pressure of the materials is measured with Bayard-Alpert flux gauge which can be inserted just beneath the substrate holder. Pyrometer is utilized to monitor surface temperature of the wafer during growth. Reflection High Energy Electron Diffraction (RHEED) is also a useful tool for real time surface inspection and checking material quality where a gun fires an electron beam which gets reflected from the wafer surface according to atom arrangement and a diffraction pattern is observed on a screen. These tools were utilized in this work. The overall picture of the MBE system is presented in Figure 3.2.

3.1.2. Growth Procedure of the Designs

Before starting to growth, LN_2 is introduced to the system through the flex lines and it is waited until growth chamber pressure is reduced to $\sim 10^{-11}$ Torr levels. Then, wafer is loaded to the loading chamber and transferred to PREP oven by elevator system in the reactor for general cleaning of atmospheric residue at high temperatures.

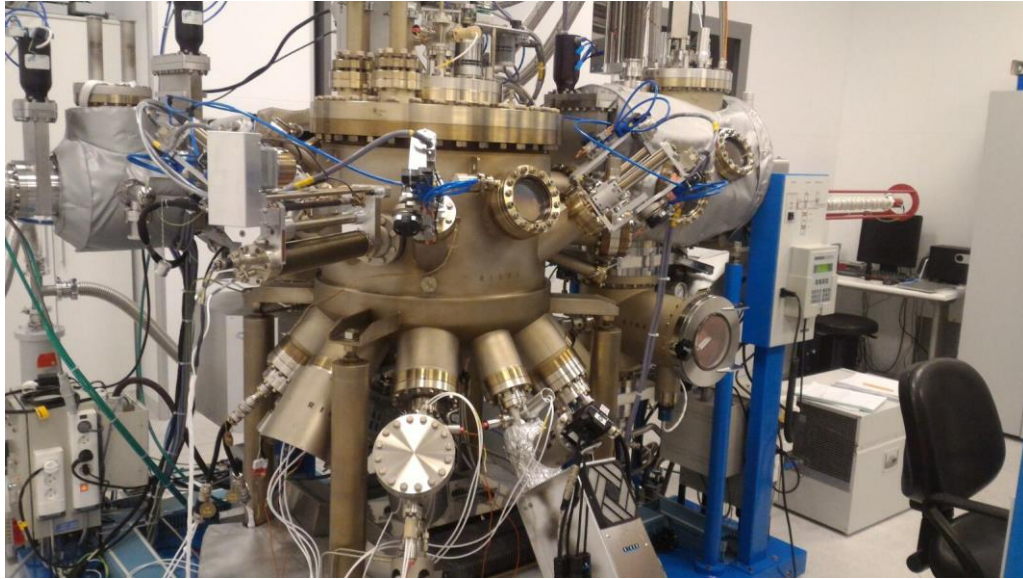


Figure 3.2: METU III-V Riber Epinat MBE Reactor.

At the same time, degassing process of the effusion cells is started. For this purpose, the cells are heated up just beyond their growth temperature. After degassing process is over, flux calibration of the materials is begun. First, flux gauge is inserted to the growth chamber. Then, each material cell shutter or valve is opened one by one and desired flux value is adjusted by playing with base and tip temperatures or valve opening. In and Ga elements need the careful attention in flux calibration as they are going to determine the mole fraction of InGaAs material. After iterative growths and X-ray Diffractometer (XRD) measurements, the In:Ga flux ratio was determined. Group V elements usually have higher beam equivalent pressure than Group III elements and the growth rate is identified from the sticking rate of Group III elements to the substrate, so it will be okay to have enough amount of Group V elements in the chamber. Si and Be cell temperatures are also determined in order to achieve the required doping concentrations which were decided after consecutive fabrication of different detectors.

Following the wafer degassing in PREP oven and flux calibration, InP substrate is transferred to growth chamber and attached to substrate holder. In order to remove the oxide layer on the surface by thermal cleaning, holder temperature is increased gradually

and diffraction pattern in RHEED screen is monitored in real time until diffraction shape of InP crystal atoms is observed as the oxide layer is lifted up. During this oxide desorption process, P loss occurs from the substrate due to high temperature, so the process is executed under P pressure meaning that P valves are opened. After observing high quality crystal, growth recipe is then started by opening In shutter and growing a short InP buffer layer. The growth temperatures and fluxes are adjusted in the recipe such that epistructures in Figure 3.1 are obtained.

During the growth, the most important parameter is the substrate temperature. Excessive shifts in substrate temperature easily cause generation defects and dislocations on the substrate which can be even seen with bare eyes and these defects introduce trap states to bandgap of the material and increases G-R component of the dark current. Since InGaAs is a low bandgap material compared to InP, the blackbody radiation coming from the effusion cells at growth temperature can be absorbed by InGaAs which results in increase in substrate temperature. Therefore, during InGaAs layer growths especially in high thickness absorber, substrate temperature is frequently monitored by pyrometer and according to the increasing trend in surface temperature of InGaAs, holder temperature is decreased.

An important concluding remark is that in planar type InGaAs wafer growths, p type doping is not done but it is achieved with Zn diffusion process. The reason is explained in Chapter 2.5.1 while mentioning the difference between planar and mesa process. Hence, Be cell does not get heated up in planar InGaAs growths, but it is used as a p doping source for only InGaAs photodetectors which will be fabricated by mesa process.

3.1.3. Wafer Characterization

After epitaxial growth, quality of the wafer is checked via XRD measurement. “Rigaku Smartlab” XRD device was utilized for XRD measurement of the wafers. Basically, an X-ray gun present in the system fires X-ray beams to the wafer surface for specific angles defined from a computer program. Scattered rays from surface are detected with a detector. Working principle of the device is based on Bragg’s law which is expressed as:

$$n\lambda = 2d \sin \theta \quad (3.1)$$

where d is the distance between atomic planes and θ is the incident angle. It says that constructive interference of the scattered rays from adjacent planes occurs when phase difference of the rays becomes equal to multiple of radiation wavelength. Therefore, for only a specific angle for each material, we observe the constructive interference which appears as peaks at XRD measurement result. We expect to see narrow and sharp peaks in high quality wafers since it means that no considerable shift in material flux occurred during material growth. To check the narrowness of those peaks, full width half maximum (FWHM) is calculated, and lower FWHM signifies better crystal quality.

XRD measurement also allows us to examine mole fraction of grown InGaAs material. If exactly 0.53 In mole fraction was not achieved in growth process, we expect to observe multiple peaks at measurement result. In that case, a rocking curve simulation is utilized in which epilayer structure is inserted to program, and by varying mole fraction of InGaAs material, simulation and XRD measurement results are fitted. Hence, rocking curve simulation provides information about exact mole fraction of ternary materials and gives feedback for next growth procedures.

Figure 3.3 shows a representative XRD and rocking curve simulation result from this work. A narrow peak was obtained for InGaAs material showing good quality.

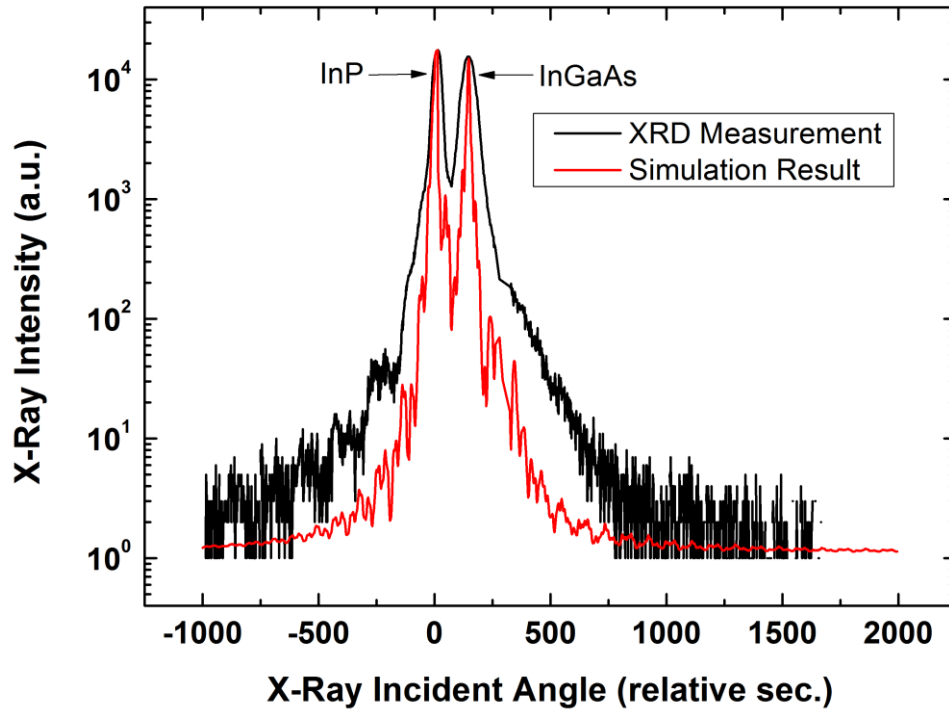


Figure 3.3: XRD and rocking curve simulation result of a wafer utilized in this work.

3.2. How to Conclude with Final Design Structure

SWIR InGaAs photodetectors fabricated in this work are based on InP/InGaAs heterojunction p-i-n photodiode operation. Considering photo-response in NIR and visible ranges, InP substrate removal was planned and InGaAs etch stop layer was also grown in order to benefit from selective wet etching of InP and InGaAs during complete removal of substrate by an acid solution. InP/InGaAs/InP p-i-n diode layers together with InGaAs etch stop layer was the initially designed epistructure. After fabrication of test detectors, it was noticed that in the forward biased region there was not expected exponential increase in the current which stems from the relatively high contact resistance. We know that making p ohmic contact is harder than constituting ground contact due to lower mobility of holes. Therefore, instead of taking contact from p InP cap layer, additional p InGaAs second cap layer was inserted since InGaAs has lower

bandgap than InP and 4 orders of magnitude higher n_i or conductivity at room temperature, so forming ohmic contact from p InGaAs layer will be easier.

The thickness and the doping concentration of each layer, particularly InGaAs absorber layer, are other important design parameters. Doping concentration of contact regions was arranged at $3 \times 10^{18} \text{ cm}^{-3}$ in order to increase conductivity and lower the contact resistance. The thickness of each layer except absorber was determined to obtain easier fabrication, for example, in contact etch or in mesa etch. However, thickness and doping of absorber layer are going to define the characteristics of the photodetector. The thickness was selected according to absorption coefficient of InGaAs material (e.g. 1800 cm^{-1} at $1.68 \mu\text{m}$ [37]) and Beer-Lambert law which is:

$$I = I_0 e^{-\alpha x}. \quad (3.2)$$

Equation 3.2 states that the intensity of the radiation decreases exponentially with increasing position. In order to collect the whole incoming radiation, the thickness of the absorber should be selected carefully. According to our calculation and also representative thickness values from the literature, $2.7\text{-}3 \mu\text{m}$ thick InGaAs satisfies high photocurrent and responsivity conditions. In addition, different doping concentrations were tried to find the optimized value apart from the unintentional background doping. Figure 3.4 shows I_{dark} of fabricated representative test detectors under 4 different doping concentrations. It basically indicates that I_{dark} can be reduced by increasing doping concentration up to some point. This is related to decrease in depletion width which is formed between InGaAs absorber-p InP layers. Similarly, Figure 3.5 illustrates representative photocurrent for each doping concentration. As expected, by increasing doping value, photocurrent we measure decreases since carrier recombination rate increases and carrier lifetimes degrade due to higher impurity levels.

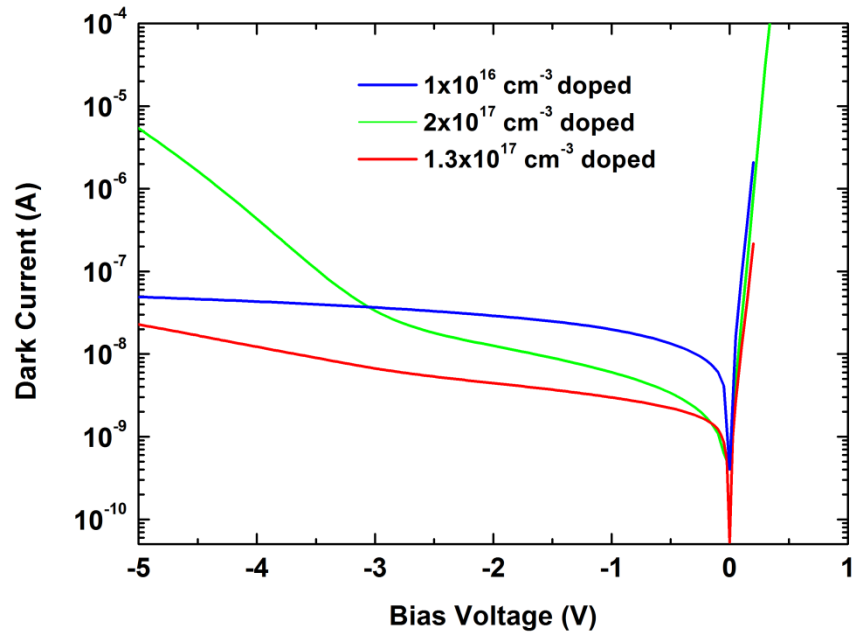


Figure 3.4: Representative dark current of test detectors under different doping concentration of absorber layer.

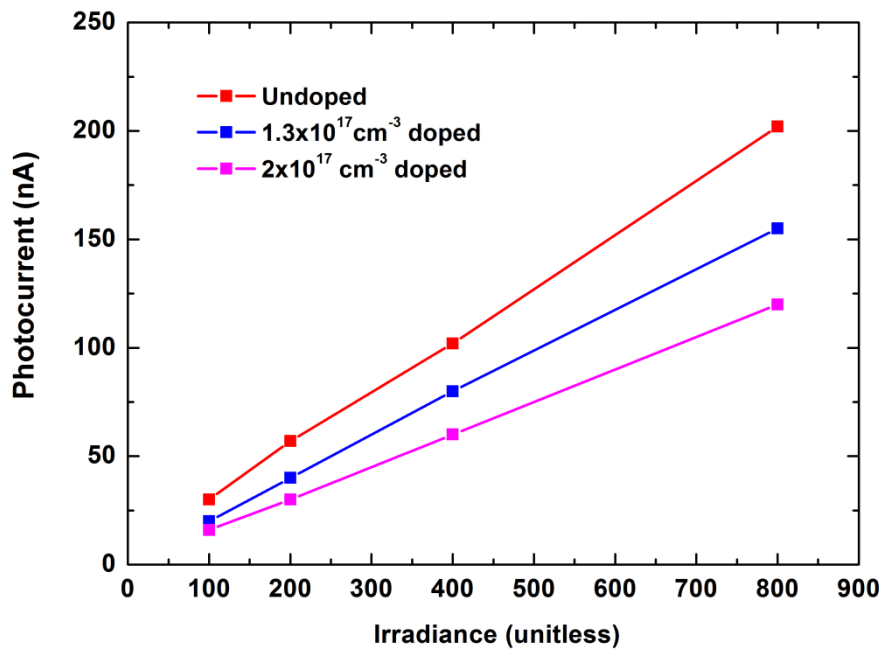


Figure 3.5: Representative photocurrent of test detectors under different doping concentration of absorber layer.

3.3. Fabrication Procedure of NIR/SWIR InGaAs Photodetectors

This work includes fabrication development of planar type 25 μm pitch, 640x512 format and 15 μm pitch, 1280x1024 format FPAs together with mesa type 25 μm pitch, 640x512 FPAs. Photolithography steps in fabrication were accomplished by “ μPG501 of Heidelberg Instruments” Direct Writer device.

3.3.1. Fabrication of Planar Type Photodetectors

Before moving on to fabrication step, first, necessary portion of wafer is diced and alignment marks are formed.

Zn Diffusion: Fabrication starts with p type doping of the epilayer with Zn atoms. The doped regions also directly define pixel regions since p-i-n diode structures will be formed where p type doping exists. Therefore, the distance between Zn diffused areas basically corresponds to the pixel pitch. The resulting epilayer structure can be seen from the representative Figure 3.6 after Zn diffusion process.

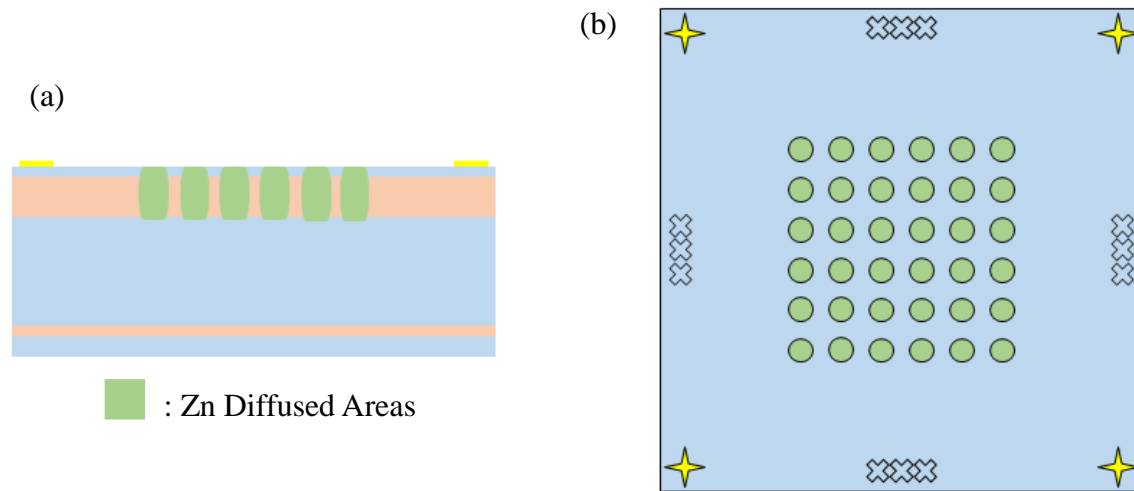


Figure 3.6: (a) Cross section view of epilayer after Zn diffusion. (b) Top view of epilayer after Zn diffusion.

Contact Formation: First, p type contacts are created at the top of the pixels. For this purpose, proper metals are deposited by thermal evaporation technique. Contact formation is finalized by lift-off process. In order to form chemical bond of these metals with InGaAs layer and to reduce the contact resistance, annealing process is applied as well.

Ground or n type contacts are taken from n-InP layer and outside the pixel regions, and metals are deposited again by thermal evaporation. Lift-off process finalizes ground contact formation. Likewise in p contact, annealing helps to create ohmic contact characteristic.

Pixel Isolation: In planar process, a depletion region is created around Zn diffused areas as there are formed p^+ -n junctions. Depletion region extends from absorber layer to wafer surface. In the absorber layer, it is the origin of bulk component of G-R current mechanism, and at the surface, it generates surface G-R current. Surface G-R current shows correlation with the bandgap of the material it is generated on. Etching of top InGaAs layer also somehow means isolation of the pixels from each other and it reduces crosstalk in imaging up to some degree.

Surface Passivation: In planar processes, planarity of the surface is preserved, and no sidewalls around the pixels are formed. This situation reduces the surface leakage current in the pixels which is related to perimeter of a pixel. However, still, dangling bonds or accumulated charges coming from residual byproducts during chemical etch make wafer surface electrically active and create surface leakage current. This current should be reduced as it becomes the dominant dark current in the devices and it is the reason why mesa type is not preferred in state-of-the-art 1.68 μm cutoff InGaAs photodetectors. Therefore, surface passivation is required and a suitable dielectric material should be found.

Under Bump Metallization (UBM) and Indium Deposition: In bump formation is a vital process for hybrid integration of FPA and ROIC. In bumps should be placed on both FPA and ROIC pixels, and flip-chip bonder device connects those In bumps by

applying a mechanical force. In is a soft and sticky material which makes it easier to shape and provides easy connection of bumps during bonding. In is also able to diffuse into epilayer after deposition like Zn atoms, and this issue can distort proper photodiode operation. In order to prevent In diffusion, first an UBM process is required for both FPA and ROIC sides. UBM metals were also deposited by thermal evaporation followed by a lift-off process.

Flip-Chip Bonding: In order to integrate FPAs with ROICs, “SET FC150” flip-chip bonder device was utilized. In this work, only 640x512 format FPAs were hybrid integrated to “FLIR Indigo ISC0002” ROIC. “ISC0002” ROIC specifications are provided in Table 3.1 [38].

Table 3.1: “ISC0002” ROIC Parameter Specifications [38].

ROIC Parameter	Parameter Specification
Array Size	640x512
Pixel Pitch	25 μm
Input Circuit	CTIA
Integration Type	Snapshot Mode
Integration Time	Adjustable > 5.4 μs
Detector Application	p-on-n InGaAs or HgCdTe
Operating Temperatures	80 K to 310 K
Bias Range	0 to 2.5 V
Outputs	Selectable 1, 2, or 4 Outputs
Power Consumption	< 225 mW for Single Output < 325 mW for 4 Outputs at max frame rate

Gain or Capacitance Control	Gain Bit	Maximum e^-	Capacitance Value	Capacitance Noise
	0	39 K	2.5 fF @ 2.5 V	70 e^- @ 250 K and -0.5 V
	1	1.9 M	122 fF @ 2.5 V	656 e^- @ 250 K and -0.5 V

Under-fill Injection and InP Substrate Removal: As mentioned before, InP blocks incident radiation below 920 nm wavelength, and if we want to operate InGaAs photodetector at NIR or visible region, InP substrate removal is a necessity. In this work, substrate removal was achieved in two steps where mechanical grinding was followed by wet etching. For mechanical grinding, “DAG810” substrate grinding machine was utilized whose picture is given in Figure 3.7. After that, substrate removal was completed by wet etching. Due to selective etching, hydrochloric acid (HCl) reaction with the sample stops when it encounters with InGaAs etch stop layer which was the planned utilization of this layer in the first place. As a final remark, InGaAs etch stop layer was also removed after substrate removal because it absorbs radiation before reaching to absorber. Whole InP substrate removal process is summarized in Figure 3.8 for visualization.



Figure 3.7: “DAG810” substrate grinding machine utilized for substrate removal.

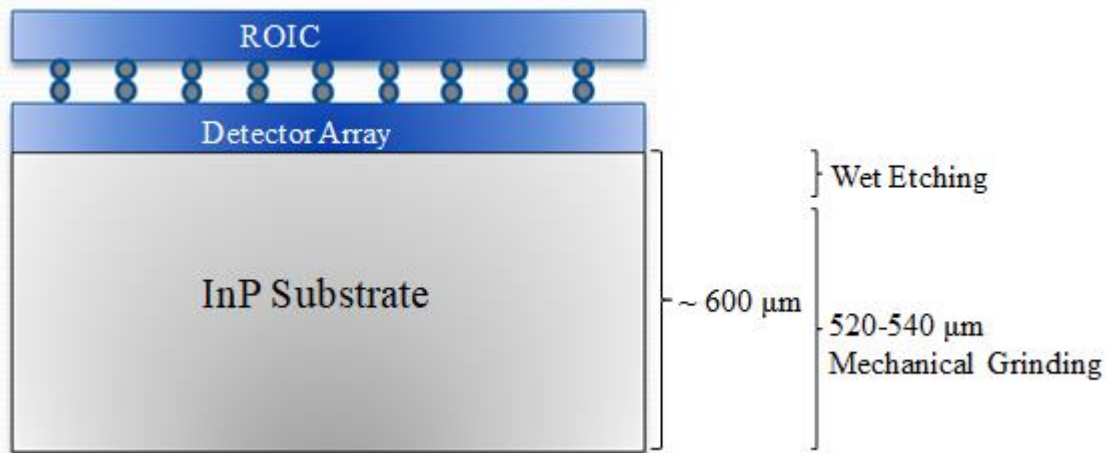


Figure 3.8: Schematic representing substrate removal process.

Challenges in Fabrication: In planar type process, fabrication of 25 μm pitch FPAs is relatively easier compared to 15 μm pitch FPAs. Higher pixel pitch gives freedom in selecting diffusion area size or metal sizes. Alignment is an important subject and it needs substantial attention since direct writer device itself has 1-2 μm resolution and exposed areas may shift from originally planned locations. In addition, In bump widening is another effect to not to short the pixels.

Under-fill injection and substrate removal are other challenging processes for both 15 and 25 μm pitch detectors. If any void is left between pixels, it was experienced that FPA-ROIC connection may be lost in these voids. Moreover, wet etching step in substrate removal is a process which can decrease the yield ratio.

3.3.2. Fabrication of Mesa Type Photodetectors

Mesa process differs from planar process only in pixel formation step. Wafers are already p doped during the growth, so there is no diffusion step in mesa process. Pixels are formed by etching in mesa shape and it is also called as mesa etching. After forming p and n type contacts as exactly described in planar process, mesa pixels are created by wet etching. Mesa etching allows perfect isolation of pixels from each other which diminishes crosstalk and additional pixel isolation process is not needed. Surface passivation, UBM and In processes follow mesa etching which are done in exactly the same way expressed in planar process. Figure 3.9 demonstrates whole mesa type detector structure after having done the explained steps.

Challenges in Fabrication: In addition to the same difficulties faced in planar process, absorber etching time when creating mesas was optimized, in order to create around $20 \times 20 \mu\text{m}^2$ of mesa tops. Furthermore, surface passivation becomes complicated since we have sharp sidewalls at surroundings of the pixels.

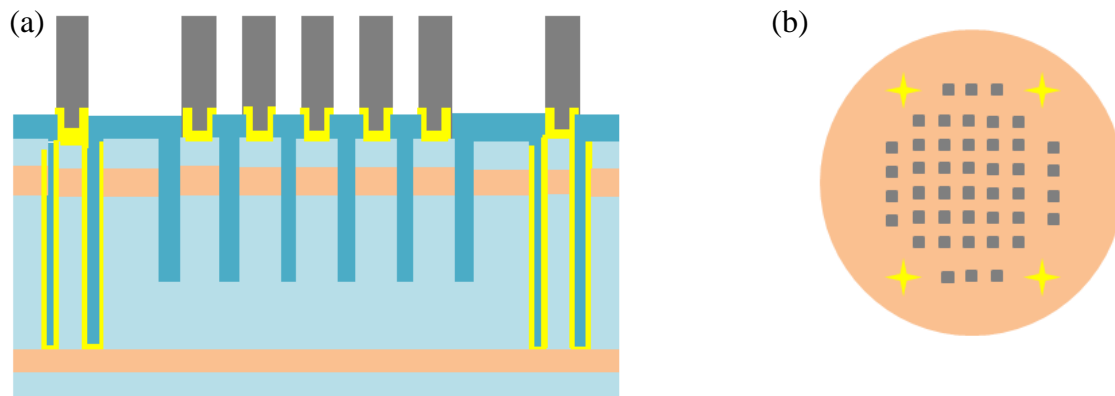


Figure 3.9: (a) Cross section view of epilayer after all mesa processing steps. (b) Top view of epilayer after all mesa processing steps.

3.4. Characterization Results of NIR/SWIR InGaAs Photodetectors

Dark current characterization, photo-response, noise characteristic and imaging results of 25 and 15 μm pitch, planar and mesa NIR/SWIR InGaAs FPAs will be presented in this section. Results except for imaging were taken from test detectors fabricated together with FPAs in the same cleanroom processing.

3.4.1. I-V Measurement Results

Planar 25 μm Pitch Photodetectors: I-V curve of the detectors under no illumination is presented in Figure 3.10 where 155 fA was obtained under applied -0.1 V at 20 $^{\circ}\text{C}$. The measurement was taken from hybrid integrated 100 test detector pixels and results were normalized to 1 pixel. Dark current values are in the same range with the ones reported in state-of-the-art 25 μm pitch InGaAs detectors discussed in Chapter 2.

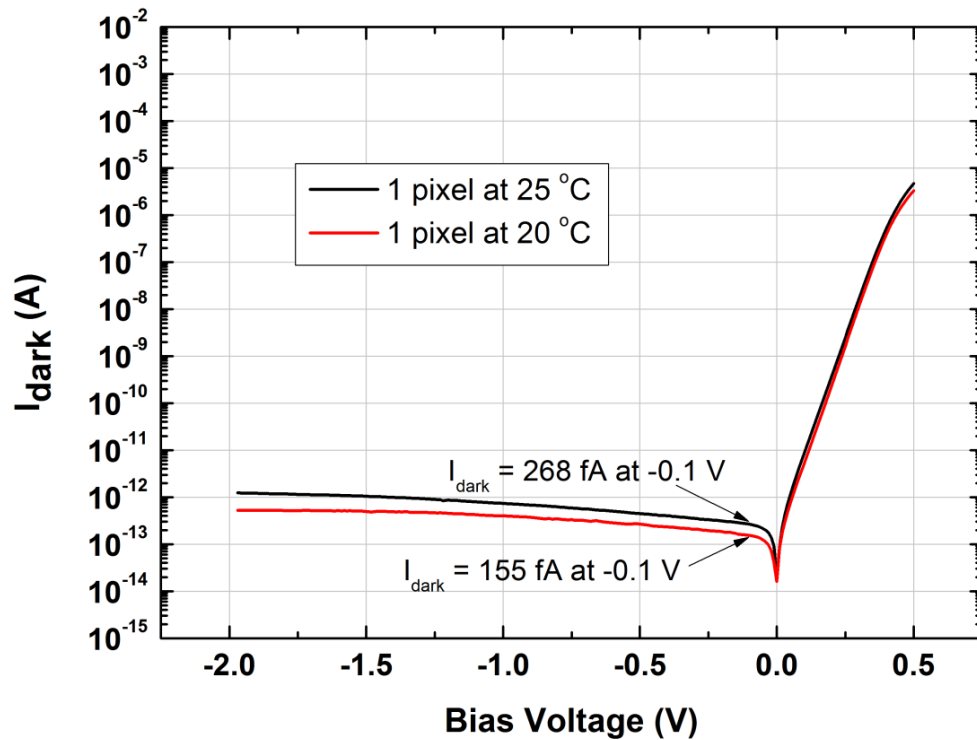


Figure 3.10: I-V curve of 25 μm pitch planar detectors at 20 and 25 $^{\circ}\text{C}$.

Planar 15 μm Pitch Photodetectors: 15 μm pitch detector fabrication was more challenging process as mentioned in previous section and I-V curves acquired are given in Figure 3.11 where 281 fA was obtained at 20 $^{\circ}\text{C}$ under applied -0.1 V. The measurement was again taken from hybrid integrated 100 test detector pixels and results were normalized to 1 pixel.

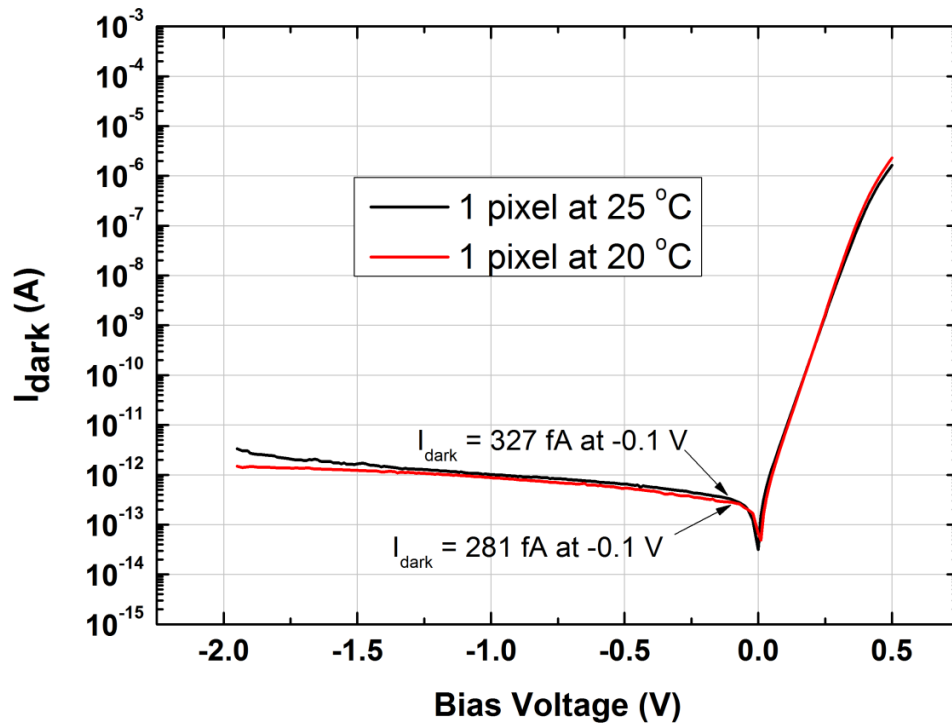


Figure 3.11: I-V curve of 15 μm pitch planar detectors at 20 and 25 °C.

Mesa 25 μm Pitch Photodetectors: As mentioned above, even with proper passivation techniques, surface leakage current in mesa type detectors is still the dominant dark current mechanism. I_{dark} from a fabricated mesa test detector at 25 °C is provided in Figure 3.12 where 10.49 pA dark current was obtained at -0.1 V.

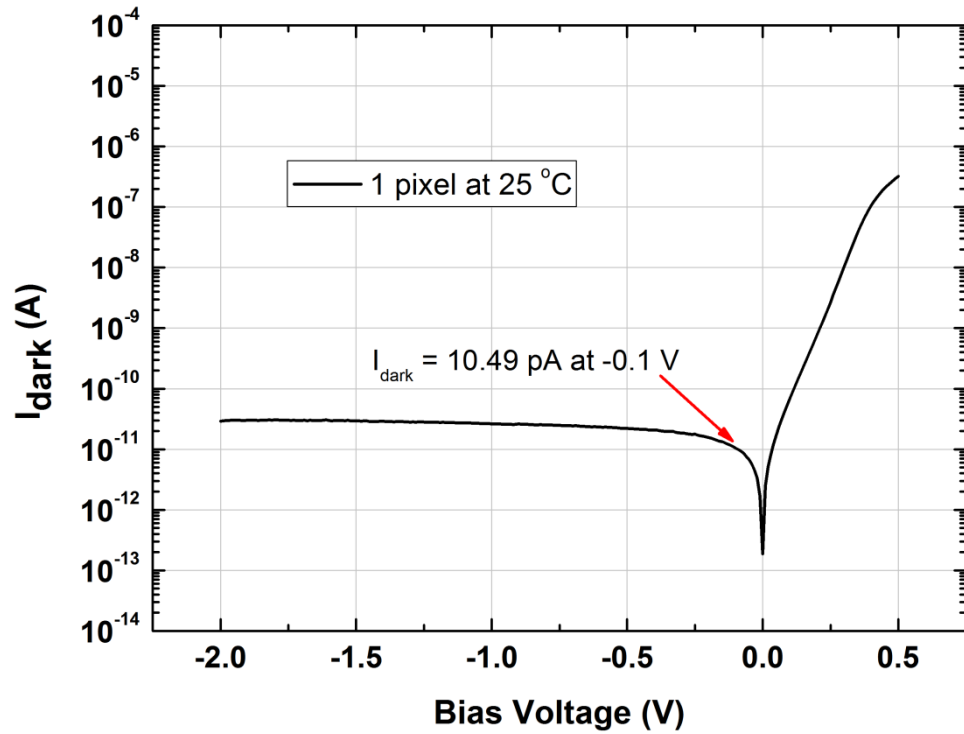


Figure 3.12: I-V curve of 25 μm pitch mesa detectors at 25 $^{\circ}\text{C}$.

3.4.2. Responsivity and Detectivity Measurement Results

Responsivity of FPAs was also determined from the test detectors fabricated together with FPAs. A “Newport” monochromator device was utilized to measure responsivity whose picture is given in Figure 3.13. The overall setup consists of 4 different parts mainly which can be listed as light source, monochromator, transimpedance pre-amplifier and lock-in amplifier. Basically, a halogen light bulb provides necessary radiation inside the system. The radiation is first filtered for desired wavelengths and modulated by a chopper rotating at 30 Hz frequency, and delivered to monochromator part. Diffraction gratings located in monochromator device disperse light, in other words, they spatially split the light into different wavelengths. Then, the light waves are guided with the help of mirrors to an output port. A computer program is able to control which wavelength of the light is going to be outputted from the system or it can sweep wavelength for a defined interval with minimum 10 nm resolution. Exiting light from output port fall into our detector and detector generates photocurrent. Since photocurrent

levels are low to be analyzed by the device, a pre-amplifier is needed. Addressing this issue, a transimpedance amplifier is connected to detector output which converts photocurrent to voltage and multiplies it by a transimpedance gain (V/A). The gain value and bias voltage of the detector can be adjusted from the pre-amplifier. Afterwards, pre-amplifier output signal is connected to lock-in amplifier which is locked to only signals modulated or chopped at 30 Hz, and eliminates especially the effect of background radiation. Lock-in amplifier has unity gain, and does not affect the signal level. The output of lock-in amplifier is finally connected to computer by RS-232 cable which is serial communication protocol. From a computer program, we have a definite control over all parameters and we interpret results. Working mechanism of the complete system is illustrated in Figure 3.14.



Figure 3.13: Monochromator device and overall setup utilized in responsivity measurements.

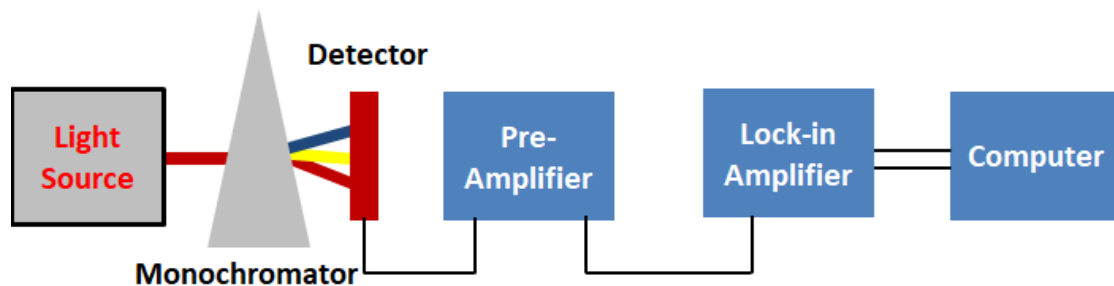


Figure 3.14: Responsivity measurement setup overview.

Only unknown in responsivity measurement setup is the radiation power of halogen light bulb over wavelength spectrum. Therefore, we utilized a calibrated InAs photodetector produced by Teledyne Judson Technologies as a reference whose responsivity spectrum is known. Before moving on to measure test detectors, first, reference detector is placed to monochromator output, and then, photocurrent of the detector is recorded in desired wavelength spectrum. As we know responsivity and photocurrent of the detector, we can easily calculate radiation power coming to reference detector by applying Equation 1.5 in watts. After extracting radiation power striking per unit area of detector, test detectors are connected to the setup. 25, 49 and 100 groups of pixels were utilized during the measurements. In reality, due to the diffusion lengths of the carriers, active covered area of these pixel groups is larger than fabricated area meaning that a pixel may collect photocurrent generated in neighboring pixels because of diffusion. In order to find diffusion length and active area of the pixel groups, photocurrents of different pixel groups were measured. By making use of the fact that each pixel group should have the same photocurrent in per unit area, diffusion length was calculated and active pixel areas were determined. At last, responsivity of the photodetectors was calculated which is nothing but the ratio of photocurrent per unit area to the radiation power per unit area. In order to find QE of the detectors, Equation 1.6 was utilized in which QE remained as only unknown after measuring responsivity.

25 μm Pitch Photodetectors: Responsivity of 25 μm pitch detectors is presented in Figure 3.15. As can be noticed, responsivity increases after removing InGaAs etch stop layer since it absorbs incoming radiation with its 0.5 μm thickness. Cutoff wavelength was determined to be 1.7 μm at 20 $^{\circ}\text{C}$ for this detector. Peak responsivity was measured as 0.89 A/W in substrate removed case at around 1.6 μm wavelength. Responsivity value is close to the theoretical predictions when antireflection coating is not deposited due to Fresnel's reflection. Therefore, it indicates that fabricated FPAs almost have 100% internal QE.

15 μm Pitch Photodetectors: Responsivity values for these detectors are provided in Figure 3.16 where the cutoff wavelength was found to be 1.68 μm . 0.94 A/W value in peak responsivity was achieved at 1560 nm wavelength which again shows almost 100% internal QE.

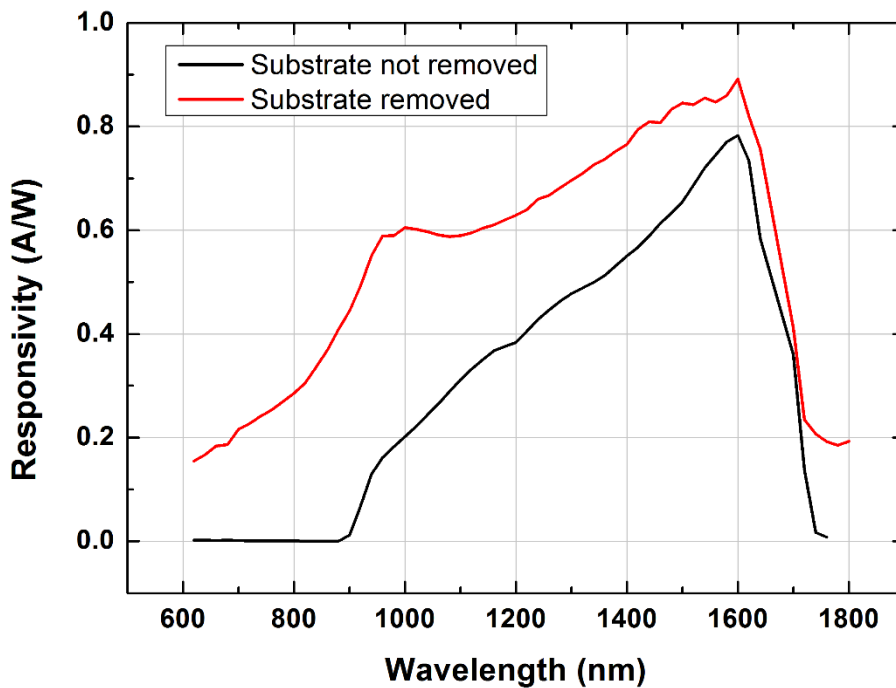


Figure 3.15: Responsivity graphs of 25 μm pitch detectors at 20 $^{\circ}\text{C}$.

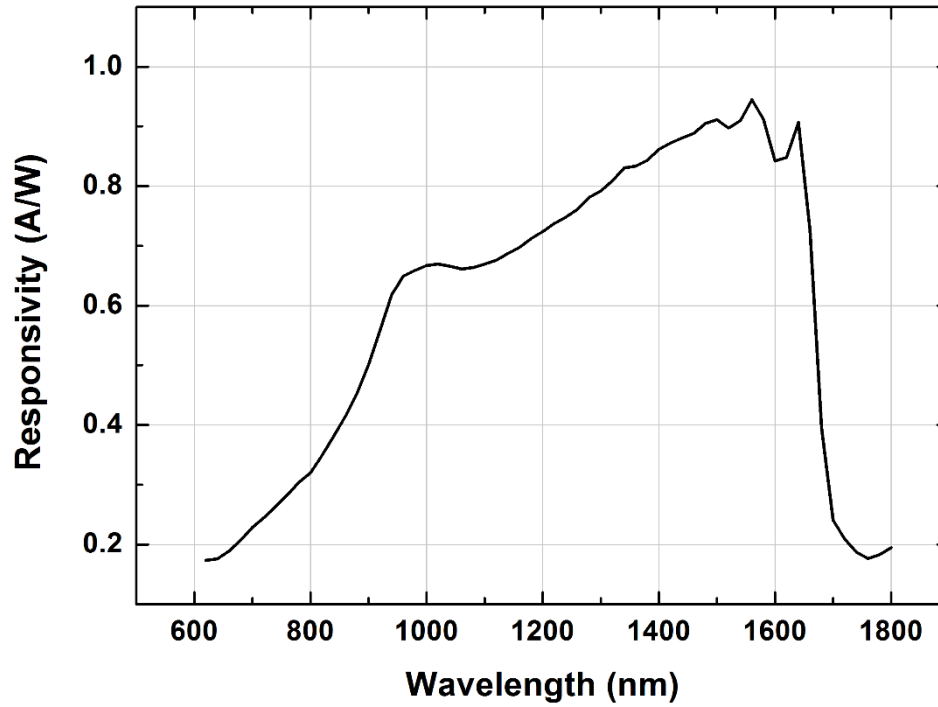


Figure 3.16: Responsivity graph of 15 μm pitch detectors at 20 $^{\circ}\text{C}$.

In this work, Johnson noise limited detectivity of the photodetectors will be presented. First, dynamic resistances of 25 μm and 15 μm pitch detectors are calculated as $5 \times 10^{10} \Omega$ and $1.75 \times 10^{10} \Omega$ respectively at 20 $^{\circ}\text{C}$ and -0.1 V bias. Then, Johnson noise current is found by putting calculated dynamic resistances to Equation 1.7. Noise currents are determined as 0.568 fA and 0.96 fA for 25 μm and 15 μm pitch detectors. Afterwards, responsivity, noise and active detector area values are inserted to Equation 1.13 to calculate detectivity parameter. According to these calculations, Johnson noise limited peak detectivities were found as 1.76×10^{13} and $1.78 \times 10^{13} \text{ cm}\sqrt{\text{Hz}}/\text{W}$ for 25 μm and 15 μm pitch detectors respectively.

3.4.3. Imaging

Imaging is an important step to characterize the pixels in FPA level and to check operability of the pixels. For this purpose, hybrid integrated FPA-ROIC sample, first, is placed on Leadless Ceramic Carrier (LCC) and necessary wirebonding is done between ROIC signal pins and LCC pins according to ROIC datasheet. Figure 3.17 shows

fabricated and integrated 640x512 25 μm pitch FPA- ISC0002 ROIC couple on LCC after substrate grinding process. Afterwards, sample is loaded into dewar which is going to be connected to an imaging system. Dewar utilized in this work has an external TEC for temperature stabilization issues. As an imaging system, “Pulse Instruments” imaging device was used. This device possesses CTIAs at the input stage which converts current signal into voltage signal. Analog-to-digital converters (ADC) transform analog signals into digital signals, and with the help of available cards and computer software, digital signals sensed for each pixel in FPA are processed for imaging.

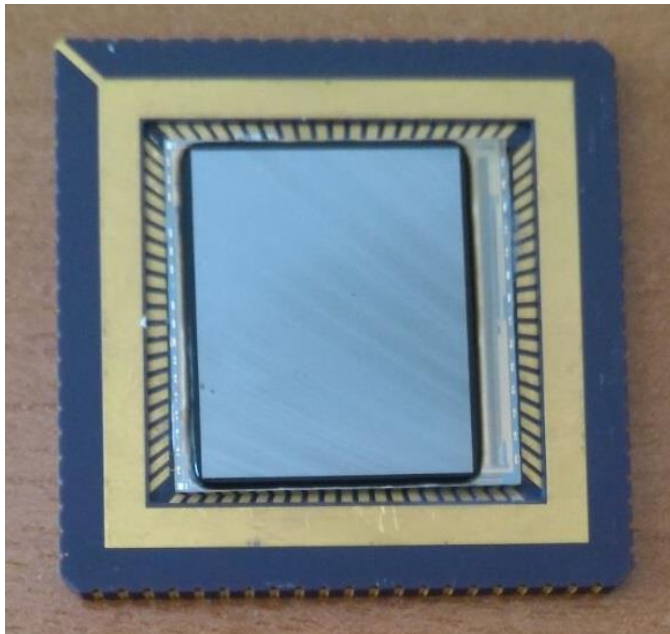


Figure 3.17: 640x512 25 μm pitch FPA- ISC0002 ROIC couple on LCC after having done substrate removal process.

In the imaging process, LCC is mounted on the dewar and temperature is stabilized at 300 K. Then, a proper connection is supplied between dewar and Pulse Instruments imaging system. Also, a SWIR lens having transparency between 0.4-1.7 μm wavelength and adjustable focal length and F/# is mounted on dewar window. From the computer software, biasing voltage of FPA pixels is set to -0.1 V from “Vref” and “Vdetcom” signals of ISC0002 ROIC. In order to examine pixel operability, two histograms are recorded for hot (high light intensity) and cold (low light intensity)

objects. “SBIR integrating sphere” was used to provide uniform hot and cold radiation to the camera. The difference of hot and cold histograms basically gives us photo-response of FPA pixels, and we can make bad pixel and operability analysis. An obtained histogram from hot and cold object difference under 5 ms integration time and with F/2 lens is depicted in Figure 3.18. In the histogram, pixels with proper photo-response constitute a Gaussian distribution curve, and pixels that do not give any response to illumination basically give 0 voltage difference under different illumination intensities. In this work, it is accepted that pixels residing between 50% and 200% of peak capacitance voltage are operating properly. As a result this assumption, it was obtained that fabricated 640x512 FPA includes only 0.57% bad pixel meaning that 99.43% operability is achieved.

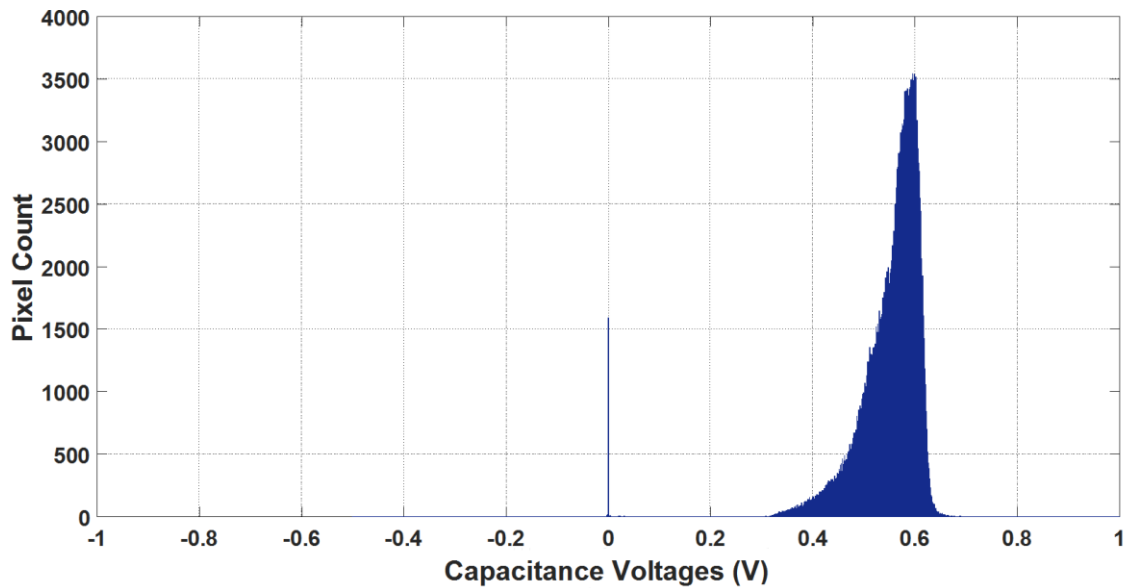


Figure 3.18: Hot and cold object’s voltage difference histogram recorded under 5 ms integration time, and with F/2 lens.

Figure 3.19 shows not optimized images recorded by the developed FPA.



Figure 3.19: Not optimized snapshots taken by 25 μm pitch 640x512 NIR/SWIR InGaAs camera.

CHAPTER 4

A NEW DESIGN APPROACH FOR InGaAs PHOTODETECTORS

In this chapter, a novel method which demonstrates the possibility of improving the characteristics of mesa type InGaAs photodetectors will be presented.

4.1. All InGaAs nBn Type Photodetector Design

Further decrease in dark current of InGaAs photodetectors is crucial particularly to sense airglow for night vision applications. Especially mesa type photodetectors need improvement in dark current. State-of-the-art planar and mesa InGaAs photodetectors seem surface leakage current limited if low noise ROICs are utilized as reported in literature and in this work. In order to address these issues, we presented a unique InGaAs nBn photodetector design [39]. Detector epitaxial structure only consists of InGaAs material and it was designed numerically by commercially available Sentaurus TCAD simulation tool.

nBn concept utilization in photodetectors have been accelerated beginning from 2006 and it is shown that they are able to reduce dark current of photodetectors significantly [40]. nBn type photodetector configuration is depicted in Figure 4.1 for the sake of discussion [41]. As you can see, there is no p-n junction in nBn detectors which ensures inherent elimination of SRH and tunneling currents.

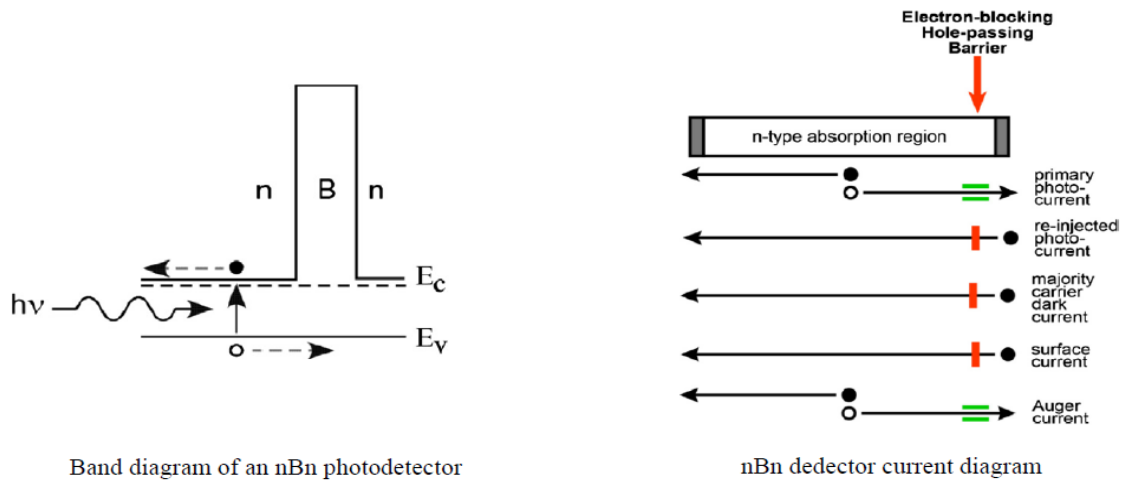


Figure 4.1: Band diagram of conventional nBn photodetectors with existing current mechanisms in configuration [41].

Also, by inserting a high bandgap material, with proper bandgap value and electron affinity, between two n doped regions, a conduction band barrier can be obtained. You can also observe direction flow of surface leakage current from Figure 4.1. According to this configuration, conduction band barrier basically blocks surface current. Surface current elimination means no need for complicated surface passivation techniques during fabrication. Filtering out surface leakage together with SRH and tunneling currents assures significant reduction in dark current of photodetectors. Only remaining dark current component becomes diffusion current associated with Auger and radiative recombination mechanism. Hence, this method is very useful to be applied in mesa type detectors where we can benefit from low crosstalk. In addition, as an important note, nBn detectors should be externally biased as there is no internally generated electric field which makes them photoconductor type detectors, but they can possess unity gain at maximum since reinjected electron is also blocked by conduction barrier.

Figure 4.1 reflects conventional nBn configuration where there is only barrier placed at conduction band, and no valence band offset exists in band diagram. Achieving zero valence band offset issue is critical because an inserted barrier at valence band does not allow to flow of photo-generated hole. If the optically generated hole cannot be collected

from the contact, basically we degrade photocurrent, responsivity and accordingly QE of the detector. Therefore, an appropriate material needs to be found for n doped regions, and it limits material selection.

Addressing barrier material limitation, we proposed a method for SWIR InGaAs photodetectors. We first created our barrier layer by increasing In mole fraction of InGaAs and by increasing the bandgap. This case breaks lattice matched condition with InP substrate, so in order to reduce lattice mismatch effect, we inserted graded layers, in which In mole fraction is gradually increased, between n doped and barrier layers at both sides. The epitaxial structure and corresponding band diagram of initial design are presented in Figure 4.2 (a) and (b) respectively.

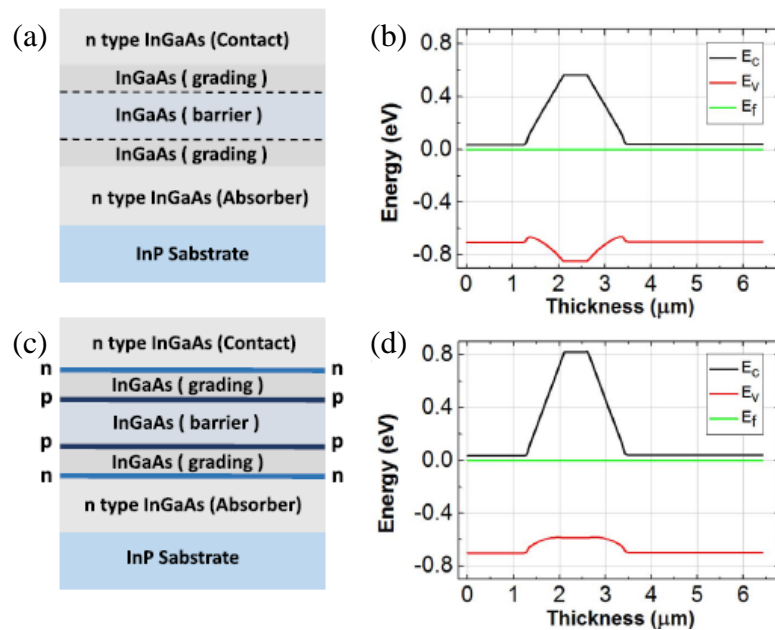


Figure 4.2: (a) First epilayer design of InGaAs nBn photodetector. (b) Corresponding band diagram of first design. (c) Final epilayer design of InGaAs nBn photodetector. (d) Corresponding band diagram of final design [39].

As you can observe, there is a valence band offset in the initial design which needs to be eliminated in order not to degrade responsivity. For this purpose, delta doping technique was utilized where two opposite polarity doped 5 nm thick sheets were inserted to the beginning and end of graded layers [42]. We know that electric potential variation in valence band offset introduces a quasi-electric field in the device, so doping polarities of delta doped sheets were adjusted so that a static electric field was created in opposite direction to the quasi-electric field. Static electric field magnitude can be calculated with Poisson equation, but by playing with doping concentrations of delta doped sheets, we continuously checked band diagram and optimized our design. Final shape of epitaxial structure and corresponding band diagram are given in Figure 4.2 (c) and (d) respectively. Eventually, we were able to push valence band offset inside band diagram and also increase barrier height in eV. In this study, it was demonstrated that all InGaAs nBn photodetector can be designed by utilizing delta doping technique and material limitations can be overcome.

4.2. Device Characterization Results

In order to put meaning to our design, we characterized our device in terms of dark current and photo-response by comparing the results with conventional InP/InGaAs p-n heterojunction detectors. A detailed modeling for surface leakage current was carried out to show that barrier is working properly and filters surface current. In the simulation program, surface current modeling is based on surface recombination rate which is provided as:

$$R_{SurfaceSRH} = \frac{np - n_i^2}{(n + n_1)/s_0 + (p + p_1)/s_0}. \quad (4.1)$$

In Equation 4.1, s_0 represent surface velocity (cm/s) parameter and, in this work, by manipulating surface velocity and also surface trap energy level which is hidden in n_1 and p_1 carrier concentration terms, we examined different surface conditions. For InGaAs material, surface velocity can be varied up to 10^6 cm/s [43]. Auger and radiative

recombination rates, and SRH lifetime were determined from a well-known, experimental based InGaAs article [44]. After constituting modeling, nBn and p-n photodetectors were analyzed for various surface velocities and SRH lifetimes. Dark current results are presented in Figure 4.3 (a) and (b), and they basically indicate the reduction of surface leakage and total dark current in the favor of nBn photodetector even if perfect InGaAs material is grown (meaning high lifetime values). 21 times improvement was achieved at -0.1 V, for $\tau_{\text{SRH}} = 47 \mu\text{s}$ and $s_0 = 4.5 \times 10^4 \text{ cm/s}$. Figure 4.3 (c) and (d) also show dark current of nBn photodetector for different barrier thicknesses and bias voltages. Barrier thickness was decided as 500 nm according to these simulation results.

In the dark current simulation of InP/InGaAs p-n diode, we were able to check characteristics of fabricated p-i-n InGaAs photodetector. After modeling SRH, Auger and radiative recombination, around 100 fA dark current was seen in the result for SRH lifetime of 10 μs , and it was observed that SRH current is the primary dark current mechanism. After inserting surface current to the model, as it can be seen from Figure 4.3 (a), surface current started to dominate the overall dark current even $s_0 < 10 \text{ cm/s}$ if passivation is not done properly. We are actually getting similar results from the produced InGaAs photodetectors. In short, this study allowed us to compare our experimental results with simulation results and strengthened our experimental findings.

Response of both type detectors under illumination was also examined. 0.01 W/cm^2 optical power was introduced to systems in parallel to epitaxial growth direction. nBn and p-n photodetectors yielded similar results in responsivity and around 80% QE can be reachable in both detectors. Responsivity and QE spectrum of both detectors are depicted in Figure 4.4 (a) and (b) respectively. A small disparity in photo-responses can be related to incapability of achieving exactly zero valence band offset in nBn detector.

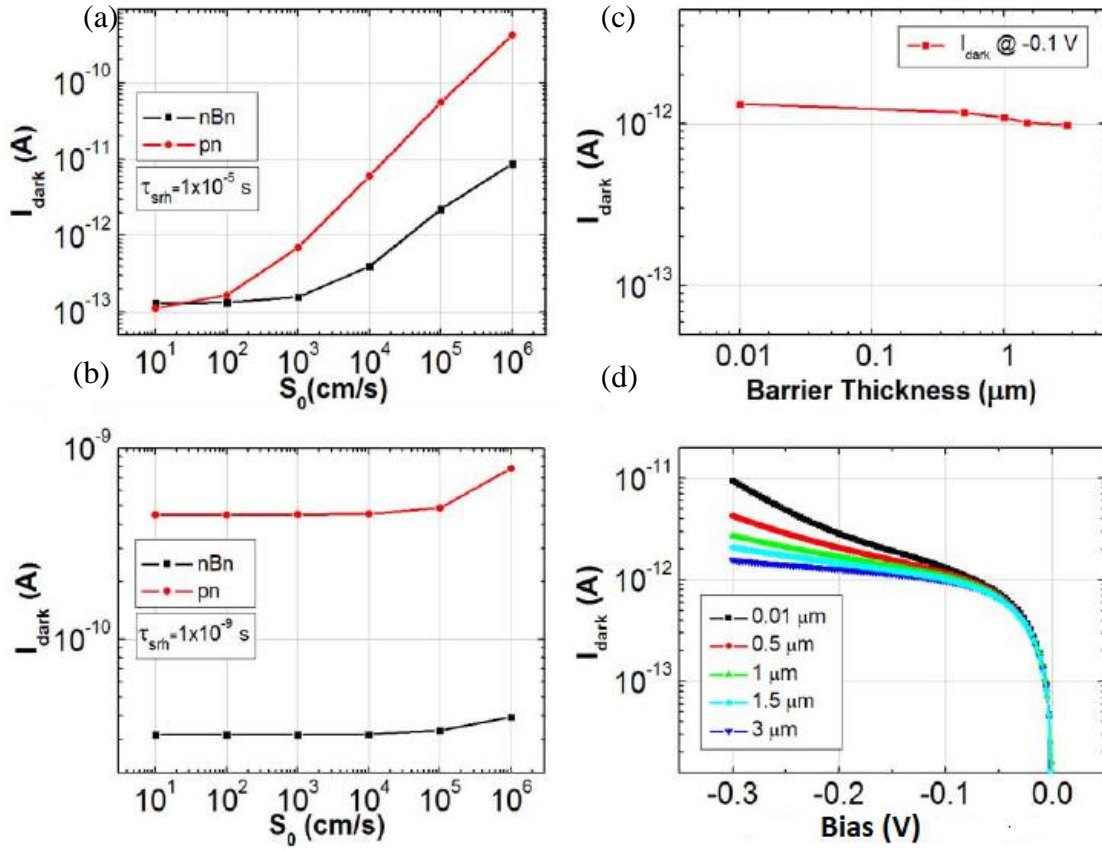


Figure 4.3: (a) nBn and p-n InGaAs photodetectors' dark current for different surface velocities at $\tau_{\text{SRH}}=10 \mu\text{s}$. (b) nBn and p-n InGaAs photodetectors' dark current for different surface velocities at $\tau_{\text{SRH}}=1 \text{ ns}$. (c) Barrier thickness versus dark current in nBn detector at -0.1 V . (d) $I_{\text{dark}}-V$ curve of nBn detector for various barrier thicknesses [39].

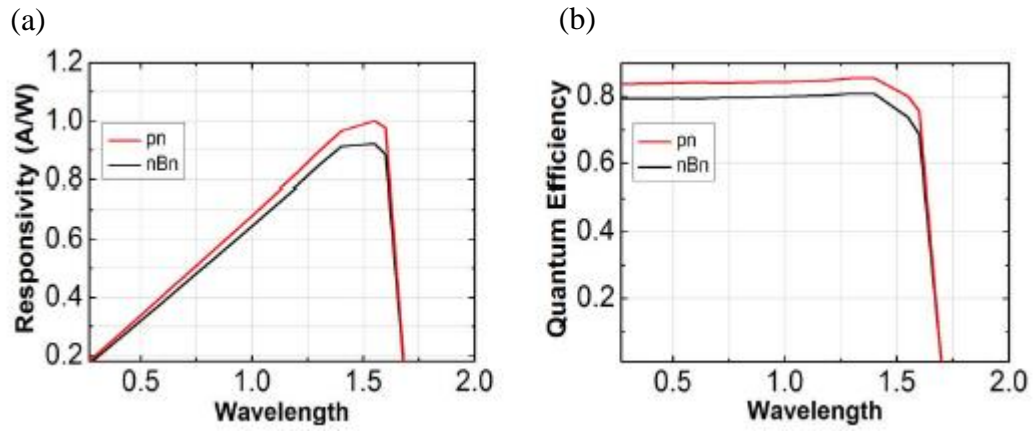


Figure 4.4: (a) Responsivity of nBn and p-n detectors. (b) QE of nBn and p-n detectors [39].

CHAPTER 5

CONCLUSION AND FUTURE WORK

In this thesis work, fabrication and characterization results of planar and mesa type 25 μm pitch 640x512 and 15 μm pitch 1280x1024 NIR/SWIR InGaAs photodetectors are presented. Particularly for planar type process, a fabrication procedure was developed. Progress of epitaxial structure and challenges encountered in fabrication steps are tried to be considered from all aspects. Measured dark current values from the photodetectors were appeared to be in 100-250 fA range at 20 °C which means that results are very close to state-of-the-art InGaAs photodetectors. Almost 100% internal quantum efficiency and photo-response in NIR and visible wavelengths was achieved successfully considering there is no antireflection coating. More than 99% operability in FPA pixels was obtained and good looking snapshots from a 640x512 format camera were captured. As a result of the work, high performance InGaAs photodetectors showing very close characteristics with the commercially available ones have been produced. To the best of our knowledge, unique epilayer structures and pixel isolation methods have been utilized in this work.

Apart from InGaAs FPA fabrication, a unique all InGaAs nBn photodetector was developed with Sentaurus TCAD numerical tool in order to improve mostly mesa type photodetectors performance by reducing surface leakage current. After forming barrier layer from InGaAs material, bandgap of the structure was engineered by delta doping technique. Characterization of the device was based on comparison with conventional InP/InGaAs p-n heterojunction photodetectors which is similar to fabricated InGaAs FPAs in this work. It was shown that more than 20 times improvement in dark current is possible with nBn photodetector if we have high quality crystal and surface current is

the dominant dark current component. Photo-response of nBn detectors also yielded similar results with conventional photodetectors. As a future work, growth and fabrication of designed nBn detector will be accomplished and it can be experimentally shown that proposed method is applicable to InGaAs photodetectors.

To sum up, this thesis work covers NIR/SWIR InGaAs photodetectors from development of megapixel and large format FPAs fabrication in cleanroom which demonstrates near characteristics with state-of-the-art ones to new design methods for the performance improvement of these detectors.

REFERENCES

- [1] B. Stuart, *Infrared spectroscopy*. John Wiley & Sons, Inc., 2005.
- [2] A. Rogalski, "Infrared detectors: Status and trends," *Prog. Quantum Electron.*, vol. 27, no. 2–3, pp. 59–210, 2003.
- [3] C.Beşikci, "Infrared Devices and Systems Lecture Notes," no. September, pp. 1–245, 2015.
- [4] B. Leblon, L. Bourgeau-Chavez, and J. San-Miguel-Ayanz, "Use of Remote Sensing in Wildfire Management," *Sustain. Dev. - Authoritative Lead. Edge Content Environ. Manag.*, 2012.
- [5] M. Razeghi, *Fundamentals of solid state engineering, 3rd edition*. 2009.
- [6] G. M. Koretsky, J. F. Nicoll, and M. S. Taylor, "A Tutorial on Electro-Optical/Infrared (EO/IR) Theory and Systems," *Inst. Def. Anal.*, p. D-4642, 2013.
- [7] A. Rogalski, "Infrared detectors : an overview," *Infrared Phys. Technol.*, vol. 43, pp. 187–210, 2002.
- [8] J. P. Perez, A. Evirgen, P. Christol, A. Cordat, A. Nedelcu, and J. Abautret, "Midwave infrared InSb nBn photodetector," *Electron. Lett.*, vol. 50, no. 20, pp. 1472–1473, 2014.
- [9] G. Gershon, E. Avnon, M. Brumer, W. Freiman, Y. Karni, T. Niderman, O. Ofer, T. Rosenstock, D. Seref, N. Shiloah, L. Shkedy, R. Tessler, and I. Shtrichman, "10 μ m pitch family of InSb and XBn detectors for MWIR imaging," *Infrared Technol. Appl. XLIII*, vol. 10177, p. 101771I, 2017.

- [10] A. Rogalski, "Progress in focal plane array technologies," *Prog. Quantum Electron.*, vol. 36, no. 2–3, pp. 342–473, 2012.
- [11] S. D. Gunapala, S. V. Bandara, J. K. Liu, C. J. Hill, S. B. Rafol, J. M. Mumolo, J. T. Trinh, M. Z. Tidrow, and P. D. Levan, "1024 × 1024 pixel mid-wavelength and long-wavelength infrared QWIP focal plane arrays for imaging applications," *Semicond. Sci. Technol.*, vol. 20, no. 5, pp. 473–480, 2005.
- [12] Y. Arslan, T. Colakoglu, and C. Besikci, "Diffraction-grating-coupled high quantum efficiency InP/InGaAs quantum well infrared photodetector focal plane array," *IEEE J. Quantum Electron.*, vol. 49, no. 2, pp. 186–195, 2013.
- [13] J. Battaglia, R. Brubaker, M. Ettenberg, and D. Malchow, "High speed Short Wave Infrared (SWIR) imaging and range gating cameras," in *Proc. of SPIE*, 2007, vol. 6541, pp. 1–12.
- [14] M. P. Hansen and D. S. Malchow, "Overview of SWIR detectors, cameras, and applications," in *Proc. of SPIE*, 2008, vol. 6939, p. 69390I.
- [15] M. MacDougal, A. Hood, J. Geske, C. Wang, D. Renner, D. Follman, and P. Heu, "Wide-area SWIR arrays and active illuminators," in *Proc. of SPIE*, 2012, vol. 8268, p. 82682Y–82682Y–8.
- [16] J. Allen, D. C. Dayton, J. D. Gonglewski, M. M. Myers, and R. Nolasco, "Seasonal hemispherical SWIR airglow imaging," in *Proc. of SPIE*, 2011, vol. 8165, p. 81650P.
- [17] M. Vatsia, U. Stich, and D. Dunlap, "Night-sky radiant sterance from 450 to 2000 nanometers," ARMY NIGHT VISION LAB FORT BELVOIR VA, 1972.
- [18] T. Y. Liow, K. W. Ang, Q. Fang, J. F. Song, Y. Z. Xiong, M. Bin Yu, G. Q. Lo, and D. L. Kwong, "Silicon modulators and germanium photodetectors on SOI: Monolithic integration, compatibility, and performance optimization," *IEEE J.*

- Sel. Top. Quantum Electron.*, vol. 16, no. 1, pp. 307–315, 2010.
- [19] T. Tsuchizawa, K. Yamada, T. Watanabe, S. Park, H. Nishi, R. Kou, H. Shinojima, and S. I. Itabashi, “Monolithic integration of silicon-, germanium-, and silica-based optical devices for telecommunications applications,” *IEEE J. Sel. Top. Quantum Electron.*, vol. 17, no. 3, pp. 516–525, 2011.
- [20] H. Figgemeier, M. Benecke, K. Hofmann, R. Oelmaier, A. Sieck, J. Wendler, and J. Ziegler, “SWIR detectors for night vision at AIM,” in *Proc. of SPIE*, 2014, vol. 9070, p. 907008.
- [21] R. Breiter, M. Benecke, D. Eich, H. Figgemeier, A. Weber, J. Wendler, and A. Sieck, “MCT SWIR modules for passive and active imaging applications,” in *Proc. of SPIE*, 2016, vol. 981908, p. 981908.
- [22] J. Piotrowski and A. Rogalski, “High-operating-temperature infrared photodetectors,” in *Proc. of SPIE*, 2007, vol. PM169, p. 256.
- [23] R. Breiter, M. Benecke, D. Eich, H. Figgemeier, A. Weber, and J. Wendler, “Progress on MCT SWIR modules for passive and active imaging applications,” in *Proc. of SPIE*, 2018, vol. 1017708, pp. 1017708–1.
- [24] P. Castelein, N. Baier, O. Gravrand, L. Mollard, D. Brellier, F. Rochette, A. Kerlain, L. Rubaldo, Y. Reibel, and G. Destefanis, “Latest developments in the p-on-n HgCdTe architecture at DEFIR,” in *Proc. of SPIE*, 2014, vol. 9070, p. 90702Y.
- [25] C. Cervera, O. Boulade, O. Gravrand, C. Lobre, F. Guellec, E. Sanson, P. Ballet, J. L. Santailier, V. Moreau, J. P. Zanatta, B. Fieque, and P. Castelein, “Ultra-Low Dark Current HgCdTe Detector in SWIR for Space Applications,” *Journal of Electronic Materials*, vol. 46, no. 10, pp. 6142–6149, 2017.
- [26] O. Gravrand and P. Chorier, “Status of very long infrared wave focal plane array

development at DEFIR Introduction: the small band gap issue Limiting mechanisms and figure of merit,” in *Proc. of SPIE*, 2009, vol. 7298, pp. 1–12.

- [27] O. Gravrand, J. Rothman, P. Castelein, C. Cervera, N. Baier, C. Lobre, E. De Borniol, J. P. Zanatta, O. Boulade, V. Moreau, B. Fieque, and P. Chorier, “Latest achievements on MCT IR detectors for space and science imaging,” in *Proc. of SPIE*, 2016, vol. 9819, p. 98191W.
- [28] S. Paul, J. B. Roy, and P. K. Basu, “Empirical expressions for the alloy composition and temperature dependence of the band gap and intrinsic carrier density in $\text{Ga}_x\text{In}_{1-x}\text{As}$ ” in *Appl. Phys. Lett.*, vol. 69, no. 2, pp. 827–829, 1991.
- [29] H. Yuan, G. Apgar, J. Kim, J. Laquindanum, V. Nalavade, P. Beer, J. Kimchi, and T. Wong, “FPA development: from InGaAs, InSb, to HgCdTe,” in *Proc. of SPIE*, 2008, vol. 6940, p. 69403C.
- [30] B. M. Onat, W. Huang, N. Masaun, M. Lange, M. H. Ettenberg, and C. Dries, “Ultra-low dark current InGaAs technology for focal plane arrays for low-light level visible-shortwave infrared imaging,” in *Proc. of SPIE*, 2007, vol. 6542, p. 65420L.
- [31] A. Rouvié, J. Coussement, O. Huet, J. P. Truffer, M. Pozzi, E. H. Oubensaid, S. Hamard, V. Chaffraix, and E. Costard, “InGaAs focal plane array developments and perspectives,” in *Proc. of SPIE*, 2015, vol. 9451, p. 945105.
- [32] A. Rouvié, O. Huet, S. Hamard, J. P. Truffer, M. Pozzi, J. Decobert, E. Costard, M. Zécri, P. Maillart, Y. Reibel, and A. Pécheur, “SWIR InGaAs focal plane arrays in France,” in *Proc. of SPIE*, 2013, vol. 8704, p. 870403.
- [33] P. Feautrier, J. Gach, T. Greffe, F. Clop, S. Lemarchand, P. Feautrier, J. Gach, T. Greffe, F. Clop, S. Lemarchand, T. Carmignani, E. Stadler, D. Boutolleau, C. One, and C. Swir, “C-RED One and C-RED 2: SWIR advanced cameras using Saphira e- APD and Snake InGaAs detectors,” in *Proc. of SPIE*, 2018, vol. 10209,

p. 102090G.

- [34] J. F. Klem, J. K. Kim, M. J. Cich, G. A. Keeler, S. D. Hawkins, and T. R. Fortune, "Mesa-isolated InGaAs photodetectors with low dark current," *Appl. Phys. Lett.*, vol. 95, no. 3, pp. 51–54, 2009.
- [35] Y. Arslan, F. Oguz, and C. Besikci, "640x512 Extended Short Wavelength Infrared In_{0.83}Ga_{0.17}As Focal Plane Array," *IEEE J. Quantum Electron.*, vol. 50, no. 12, pp. 957–964, 2014.
- [36] T. Oğuzhan, "Molecular Beam Epitaxy Growth of InP/InGaAs Structures for Short Wavelength Infrared Photodetectors," Middle East Technical University, 2014.
- [37] A. Rogalski, *Infrared detectors*, Second Edi. CRC Press, 2010.
- [38] N. I. R. Roic and S. May, "640 x 512 NIR ROIC Specification," 2004.
- [39] F. Uzgur, U. Karaca, E. Kizilkan, and S. Kocaman, "All InGaAs Unipolar Barrier Infrared Detectors," *IEEE Trans. Electron Devices*, vol. 65, no. 4, pp. 1397–1403, 2018.
- [40] S. Maimon and G. W. Wicks, "nBn detector, an infrared detector with reduced dark current and higher operating temperature," *Appl. Phys. Lett.*, vol. 89, no. 15, pp. 1–4, 2006.
- [41] G. R. Savich, J. R. Pedrazzani, D. E. Sidor, S. Maimon, and G. W. Wicks, "Use of unipolar barriers to block dark currents in infrared detectors," in *Proc SPIE*, 2011, vol. 8012, p. 80122T.
- [42] F. Capasso, "Compositionally graded semiconductors and their device applications," *Electron. Struct. Semicond. Heterojunctions*, Springer, Dordrecht, p. 70-98, 1988.

- [43] M. Boroditsky, I. Gontijo, M. Jackson, R. Vrijen, E. Yablonovitch, T. Krauss, C. Cheng, A. Scherer, M. Krames, M. Boroditsky, I. Gontijo, M. Jackson, R. Vrijen, and E. Yablonovitch, "Surface recombination measurements on III – V candidate materials for nanostructure light-emitting diodes Surface recombination measurements on III – V candidate materials for nanostructure light-emitting diodes," *J. Appl. Phys.*, vol. 87, no. 7, p. 3497, 2000.
- [44] R. K. Ahrenkiel, R. Ellingson, S. Johnston, and M. Wanlass, "Recombination lifetime of In_{0.53}Ga_{0.47}As as a function of doping density," *Appl. Phys. Lett.*, vol. 72, no. 26, pp. 3470–3472, 1998.